UNIVERSIDAD MICHOACANA DE SAN NICOLAS DE HIDALGO

Facultad de Ciencias Físico-Matemáticas

"Mat. Luis Manuel Rivera Gutierrez"

DIVISION DE ESTUDIOS DE POSGRADO

GENERACIÓN DE MODOS PLASMÓNICOS EN METASUPERFICIES

Tesis para obtener el grado de Doctor en Ciencias en Ingeniería en Física

Presenta:

Mas-ud Ayodeji Abdulkareem

Asesor:

Dra. Mary Carmen y Monserrat Peña Gomar

Co-Asesor:

Dr. Víctor Manuel Coello Cárdenas

Morelia, Michoacán, Septiembre 2023

UNIVERSIDAD MICHOACANA DE SAN NICOLAS DE HIDALGO

Facultad de Ciencias Físico-Matemáticas

"Mat. Luis Manuel Rivera Gutierrez"

DIVISION DE ESTUDIOS DE POSGRADO

GENERATION OF PLASMONIC MODES AT METASURFACES

Thesis submitted in fulfillment of the requirements
for the degree of Doctor of Sciences in Engineering Physics

By:

Mas-ud Ayodeji Abdulkareem

Supervisor:

Dra. Mary Carmen y Monserrat Peña Gomar

Co-Supervisor:

Dr. Víctor Manuel Coello Cárdenas

Morelia, Michoacán, September 2023

Declaration of Authorship

I, Mas-ud Ayodeji ABDULKAREEM, declare that this thesis titled, "GENERATION OF PLASMONIC MODES AT METASURFACES" and the work presented in it are my own. I confirm that:

- This work was done wholly or mainly while in candidature for a research degree at this University.
- No part of this thesis has previously been submitted for a degree or any other qualification at this University or any other institution.
- The individuals who contributed directly to the thesis and their roles are listed as follows

  Conceptualization: Mas-ud A. Abdulkareem, V. Coello and Marycarmen Peña-Gomar Methodology: Mas-ud A. Abdulkareem, V. Coello and Marycarmen Peña-Gomar Software: Ricardo Téllez Limón, Mas-ud A. Abdulkareem Formal analysis: Mas-ud A. Abdulkareem, V. Coello, Mary Carmen Peña-Gomar, Maximino L. Arroyo, Citlali T Sosa, Fernando Lopez, Ramses Bautista, and Ricardo Téllez Limón Writting: Mas-ud A. Abdulkareem Supervision: Mary Carmen Peña-Gomar and Victor Coello.

Signed: _____

Date: _____

"*There is no superiority of an Arab over a non-Arab, or of a non-Arab over an Arab, and no superiority of a white person over a black, or of a black person over a white, except on the basis of personal piety and righteousness.*"

Muhammad (S.A.W.)

Resumen

GENERACIÓN DE MODOS PLASMÓNICOS EN METASUPERFICIES

El objetivo de este proyecto es diseñar, fabricar y caracterizar estructuras plasmónicas que aporten características mejoradas (respecto a las existentes) en términos de un compromiso óptimo entre el grado de confinamiento, absorción, y eficiencia de acoplamiento. Se emplean métodos de caracterización tanto lineales como no lineales. Comenzamos con el estudio de respuestas tanto lineales como no lineales de protuberancias de oro colocadas aleatoriamente sobre una película delgada de oro. Se observó que una fuerte localización debida a la retrodispersión puede provocar una enforsamiento intensa de hasta ~ 40. La dependencia de la longitud de onda de las resonancias SPP hace posible aplicar esta estructura en la nanodetección óptica. Luego diseñamos y caracterizamos conjuntos de nanopartículas de oro con periodicidad y dimensiones de partículas conocidas. Las muestras se caracterizaron con luminiscencia de dos fotones y evaluamos el factor de mejora frente a la respuesta no lineal de una película fina de oro. Obtuvimos imágenes mediadas por TPL de superficies con estructuras de sublongitud de onda y presentamos las dependencias de longitud de onda y polarización. Estudiamos numéricamente estructuras de mayor complejidad, utilizando métodos numéricos FDTD y FEM. Al insertar una capa dieléctrica entre conjuntos de protuberancias de oro y una película delgada de oro, formamos una estructura de metal-aislante-metal en la que estudiamos los espectros de reflexión, la dependencia de la periodicidad y la dependencia del espesor de la brecha de diferentes resonancias plasmónicas. Se elabora la coexistencia de resonancias plasmónicas de diferentes canales. Se estudia y aplica como filtro óptico de paso de banda una estructura aún más compleja, donde las capas MIM se colocan en cascada para formar un metamaterial hiperbólico. Los resultados muestran que se puede obtener una guía de ondas óptica con funcionalidad de filtro.

Palabras claves: Metamaterial hipabolico, resonancia plasmonica de rejillas, luminisencia de dos fotones, dominio del tiempo de diferencias finitas, resonancia de Fano

Abstract

GENERATION OF PLASMONIC MODES AT METASURFACES

The objective of the project is to design, manufacture and characterize plasmonic structures that provide improved characteristics (with respect to the existing ones) in terms of an optimal compromise between the degree of confinement, enhancement, absorption, and coupling efficiency. Both linear and non-linear methods of characterization are employed. We started with the study of both linear and nonlinear responses from randomly-positioned gold bumps on a gold thin film. It was observed that strong localization due to backscattering can provoke an intense enhancement as high as ~ 40. The wavelength dependence of SPP resonances makes it possible to apply this structure in optical nano-sensing. We then designed and characterized arrays of gold nanoparticles with known periodicity and particle dimensions. The samples were characterized with two-photon luminescence and we evaluated the enhancement factor against the nonlinear response from a gold thin film. We obtained TPL-mediated images of surfaces with subwavelength structures, and present the wavelength and polarization dependencies. We numerically studied structures with more complexity, using FDTD and FEM numerical methods. By inserting a dielectric layer between arrays of gold bumps and a gold thin film, we formed a metal-insulator-metal structure in which we studied the reflection spectra, periodicity dependence, and gap thickness dependence of different plasmonic resonances. The co-existence of plasmonic resonances from different channels is elaborated. An even more complex structure, where MIM layers are cascaded to form an hyperbolic metamaterial is studied and applied as an optical band-pass filter. The results show that an optical waveguide with filtering functionality is obtainable.

Acknowledgements

The first of all appreciations belongs to almighty Allah the lord of the universe. I express my deep gratitude to my supervisor, Mary Carmen Pena-Goma (PhD), and my co-advisor, Victor Coello Manuel Cardenas (PhD), for their unwavering support, guidance, and mentorship throughout the entire research process. Their expertise, insightful feedback, and constructive criticism have significantly shaped the direction and quality of this dissertation. A special appreciation to Dr. Mary Carmen, for her kind and motherly role during the course of the program. During my stay in CICESE-MTY, I was privileged to work with Dr. Rodolfo Cortes, Dr. Cesar Garcia, and Dr. Ricardo Tellez-Limon. They laid my foot and put me in the correct and technical ethics of using the laboratory. A special thanks to Ricardo Tellez-Limon for his viable discussions that have form an integral part of this thesis. I would like to acknowledge the contributions of Fernando Lopez, Citlali T Sosa, Ramses Bautista, Maximino L. Arroyo, for their collaboration, their expertise and dedication have been instrumental in achieving the research objectives. I can't thank my parents Muili Ayodele Abdulkareem, and Adeyinka Beatrice Adeeso enough for their unending love, support, and patience. I would definitely not have gotten this far without them. A special thanks to my wife Aminat Opeyemi Oladejo for keeping strong while I was away for the doctoral program and she had to care for the children alone, I never took that for granted. To my beautiful children, Shamsudeen Ayowande and Faoziyah Ayomide, I just can not love you enough.

I am indebted to all those mentioned above for their contributions, without which this dissertation would not have been possible. However, I must acknowledge that any errors or omissions are solely my responsibility.

Contents

List of Figures

List of Tables

List of Abbreviations

MIM	Metal-Insulator-Metal
GSP	Gap Surface Plasmon
SPP	Surface Plasmon Polariton
SLR	Surface Lattice Resonance
FDTD	Finite-Difference Time-Domain
NFC	Near Field Coupling
HMM	hyperbolic metamaterials
FWHM	Full width at Half máximum
TPL	Two-Photon Luminescence
SNOM	Scanning Near-field Optical Microscopy
LSP	Localized Surface Plasmon
LSPR	Localized Surface Plasmon Resonance
CDA	Coupled Dipole Approximation
SHG	Second Harmonic Generation
ABC	Absorbing Boundary Condition
PML	Perfectly Matched Layer
PBC	Periodic Boundary Condition
AFM	Atomic Force Microscopy
HWP	Half Wave Plate
HMM	Hyperbolic Metamaterial
LED	Light Emitting Diode
FWHM	Full Width at Half Maximum

To the Almighty Allah in whose lies my life and my beloved family that have supported me through every thick and thin of my life.

Chapter 1

INTRODUCTION

1.1 State-of-the-art

Though, the historical discovery of Surface plasmon can be dated back to the early twentieth century with the famous Wood anomaly (Woods, 1902), when Robert Wood (1868-1955) observed a diminution of illumination at certain wavelengths and at particular incident angles in a diffraction grating, only till 1957 that Ritchie suggested that the loss is associated to the interaction of the incident stream of electrons with plasma oscillations in a metal foil (Ritchie, 1957), giving birth to the field of surface plasmon polaritons (SPP). Surface plasmons are very sensitive and tight-bound to the interface on which they occur, and this confinement can be in the order of $\approx$ 180 nm (for silver at λ_0 = 450 nm). This imposes a limitation on direct observation of SPP, based on the theory of diffraction by Abbe-Rayleigh and often called Abbe diffraction limit. According to this theory, the minimum spatial distance between two objects that can be resolved distinctly in a microscope image, is given by $d = \frac{\alpha\lambda}{n \sin\theta}$. Due to this limitation, the study of SPP was hindered and could be experimentally observed at far field reflection at the time, though this methodology was inefficient. However, recent developments in sophisticated experimental techniques have made the study of SPP a continuous interest, with the invention of scanning near-field optical microscopy (SNOM), which has microscopes capable of resolving distances below λ/20 (Moreno, Gonzalez, and Saiz, 2006), and direct observation of SPP has been made easy and ubiquitous. Surface plasmon microscopy was invented in 1988 (B and W, 1988) when a scanning detector was used to measure the intensity distribution of different diffraction peaks obtained from gratings on a multilayers of cadmium arachidate. Following the development of modern nano-fabrication techniques such as electron beam microscopy (EBL) and focused ion beam in the last two decades, research in SPP has been sporadically favoured. Starting from as simple as the plasmonic properties of single metallic particles and structures (Ditlbacher et al., 2005) to particles immersed in environments with different refractive indices (Papanikolaou, 2007). In a similar trend, many numerical calculations which were not possible due to high computational resources are now realizable by the present generation high efficient computational facilities. The enhancement of SPP localization in randomly distributed metallic nanoparticle (NP) on metallic thinfilms has been numerically and experimentally evaluated (J. Beermann, 2006a; Coello, 2008a; P. Segovia, 2012), characterizing the shapes, thinfilm thicknesses, particle densities, and

dimensions. Aside the irregular arrangement of NP, the linear and nonlinear optical properties of regular structures were also studied for different metallic nanoparticle shapes. Alluminium and Silver nanocrescent particles have shown to exhibit multimodal polarization-dependent plasmon resonances in the ultraviolet (UV), visible, and near infra-red regions of electromagnetic spectrum (Swartz et al., 2016R. Bukasov, 2009). The associated surface plasmons resonances in single metallic NP are localized in nature and tightly dependent on size, shape, and the effective refractive index of the system, whereas, arrays of gold, silver, and aluminum fabricated on gold thin-film have shown to exhibit lattice modes, gap modes, and the hybridization between the two modes (Rivera, Ferri, and Jr., 2012). During the last decades, there has also been a significant advance in the application of plasmonic structures in different realm. Plasmonic nanomirrors, beam splitters (V. Coello, 2009), waveguides (Han et al., 2009; Garcia et al., 2012), and directional couplers (C.E. Garcia-Ortiz, 2019), show the possibility of exciting and manipulating SPP. The trade-off between the degree of energy confinement which is a desirable property in sensor applications, and propagation length in applied nano-circuitory, is to date an open research interest. One way that this trade-off can be achieved is fabricating array of metallic structures on top of an ion-exchange waveguide (IExWG) (R. Tellez-Limon and Salas-Montiel, 2021). Regular arrays of NP placed on metallic substrates in different shapes have also been studied and found to show localized surface plasmon (LSP), which greatly depend on the dielectic function of the medium and its environment (M.G. Nielsen, 2010), and propagating surface plasmon resonances, which depend on the grating period, and geometrical characteristics (H. Saito, 2019; N. Felidj, 2005). Local surface plasmon resonance (LSPR) and photonic lattice mode hybridization application as a sensor is significantly dependent on the substrate on which the metal array is fabricated (S.M. Novikov, 2009). The birth of ultra short pulse lasers has also sprung up the field of nonlinear optics and many work have been done on the nonlinear properties of different plasmonic structure (M.G. Nielsen, 2010). The two-photon luminescence from gold particles of different shapes, sizes, and arrangements, were analyzed experimentally using femtosecond pulse lasers, and the optical image by SPP were clearly observed and the enhancement factors were reported (Y. Zhang, 2010; X. Wang, 2014; C. Molinaro, 2016). Another interesting property is the lattice surface resonance (SLR), which arises from optical coupling of LSPR modes in arrays of metallic NP. Compared to the optical absorption of LSPR from single NP, SLR from nanoparticle arrays has much narrower optical spectrum (V.G. Kravets, 2018; Gutha, Sadeghi, and Wing, 2017; B. B. Rajeeva and Zheng, 2018; C. Cherqui, 2019).

To gain greater control over light manipulation at the nanoscale, researchers have developed a novel class of materials known as gap surface plasmon (GSP) metasurfaces. These metasurfaces are composed of a thin dielectric spacer, with sub-wavelength dimensions, situated between an optically thick metal film and arrays of sub-wavelength-sized metal elements. These metal elements are arranged in either a regular or random pattern (H. Saito, 2019). This different group of structures has been shown to have interesting optical properties and the study has increased rapidly since the last decade. There are different configurations of MIM structures. The first group of consists of truncated infinitely long two metal strips separated by a dielectric spacer. This configuration has been studied to have Fabry-Perot like resonant positions showing lateral standing waves GSP modes (Hohenau et al., 2007,T.

Søndergaard, 2007,A. Pors, 2008). The second group of GSP resonator has terminated layers of the metallic strip and a dielectric, both fabricated on an infinitely extended gold thin film (T. Søndergaard, 2005). As a third kind of GSP resonator, the truncation only occurs at the top metallic layer, showing a strong red-shift due to the removal of horizontal refractive index contrast between air and SiO_2 spacer (J. Jung, 2009). The application of MIM structures has been widely studied in different areas. Similarly, there have been widely reported in many literature for the promising Mid-Infrared applications, including chemical detection, environmental monitoring, perfect absorption, gas sensing, and thermal imaging (T.H. Xiao, 2018; R. Xu, 2018; Liang et al., 2018; J. Luo, 2019). An enhanced near-infrared photosensor was designed with two layers of lead-sulfide (PbS) Sandwiched by an aluminum Spacer (Zhao et al., 2020). Other applications as sensors are found in recent developments (Zhao et al., 2020; D.Wang et al., 2020; Leveque and Martin, 2006; Fantoni et al., 2017), while MIM structures as perfect absorbers based on different configurations have demonstrated efficient absorber (Feng et al., 2014), efficient quarter-wave plate (Pors and Bozhevolnyi, 2013b), and waveguide passive structures (Singh and Raghuwanshi, 2018). Fano resonance, defined as the interaction between a narrow discrete state and a broad continuum producing asymmetric spectral shape. Resonant suppression and enhancement have been found and attributed to this behaviour in different structures with NP on metallic substrates composition (Bushati, Guddala, and Menon, 2019; Arianfard, Wu, and Moss, 2020). The application of this feature is found in optical reflectors, sensors, and optical switching (Su et al., 2021; Bekele et al., 2019; Saudan et al., 2019).This resonance is significantly affected by many factors ranging from geometry (Su et al., 2021; Bekele et al., 2019; Saudan et al., 2019), to incident conditions. Recently, the fully atomistic model, ωFQ has been applied to explain plasmonic resonances excitation in metal NP. (Bonatti et al., 2020; Giovannini et al., 2019).

This PhD thesis is dedicated to contributing to the design and optimization of plasmonic devices based on metal-insulator-metal structure. Both experimental and numerical studies were conducted, and the results are presented in this report.

Chapter 2

THEORETICAL FRAMEWORK

2.1 Plasmons

In the free electron representation of the atomic model, a gas of free electrons with mass m and density N is considered to be moving freely and randomly against a fixed background of positively charged nuclei. This cloud of electrons exhibits a strong dependence on wave vector, which in turn determines many of the material's kinetic properties. One of these kinetic properties is the dielectric function $\epsilon(\omega,\kappa)$, which is used to describe the interaction of light with matter. The dielectric function is defined in terms of the electric field E and the polarization P. The SI unit of the measure is coulombs which are per square meter ($C.m^2$).

$$\mathbf{D} = \epsilon\mathbf{E} + \mathbf{P} = \epsilon_0\epsilon\mathbf{E}. \tag{2.1}$$

The electric field in equation 2.1 is related to the total charge density $(\rho_{ind} + \rho_{ext})$, where ρ_{ind} is the induced charge density by ρ_{ext} (external charge density). In long wavelength approximation $(\kappa \approx 0)$, the dielectric response of the electron cloud can be approximated using the equation of free electron motion driven by an electric field $\mathbf{E}$;

$$m\ddot{\mathbf{x}} = -e\mathbf{E}. \tag{2.2}$$

When an electric field $\mathbf{E}$ is applied, the electron cloud is displaced from the core positive nucleus with a restoring force due to an electric field $\mathbf{E} = 4\pi e\mathbf{x}$. Substituting this into equation 2.2 for a system with electron concentration n.

$$m\ddot{x} = -4\pi e^2 n^2\mathbf{x}, \tag{2.3}$$

leading to the second-order differential equation

$$m\ddot{x} + \omega_p^2\mathbf{x} = 0, \tag{2.4}$$

where ω_p is the natural frequency of the electron cloud, defined by the relation

$$\omega_p = \sqrt{\frac{Ne^2}{\epsilon_0 m}}, \tag{2.5}$$

TABLE 2.1 Electron density and plasma frequency values for common metals obtained by using the expression above 2.5.

Metal	Electron density $(10^{22}/m^3)$	Plasma frequency $(10^{13}Hz)$
Nickel (Ni)	18.26	2.4
Copper (Cu)	8.1	1.61
Palladium (Pd)	122.48	6.24
Silver (Ag)	5.86	1.37
Platinum (Pt)	6.62	1.45
Gold (Au)	5.9	1.37

where N is the electron density, e is the electronic charge, ϵ_0 is the permittivity of free space, and m is the effective mass of an electron. Equation 2.5 implies that the bulk plasma frequency depends only on the density of free electrons of the material. This plasma frequency for noble metals mainly lies in the UV-visible region with energies from 3 to 20 eV. The electron density of common metals and their corresponding plasma frequencies are given in table 2.1.

2.2 Localized Surface Plasmon

The application of electromagnetic field to bulk plasmon of rare metals generates dipolar oscillations whose spatial field distribution is confined to nanometer volume around the metallic nanoparticle. The interaction can be represented with a quasi-static approximation. In this way, the electric field around the metal can be studied through its absorption and scattering patterns. Assuming the problem of a particle in an electromagnetic field, the expression for the electric field both inside and outside the nanoparticle is detailed in Jackson (Jackson, 1998) as

$$E_{in} = \frac{3\epsilon_m}{\epsilon_N P + 2\epsilon_m} E_0, \tag{2.6}$$

$$E_{out} = E_0 + \frac{3n(\mathbf{n}.\mathbf{p}) - p}{4\pi\epsilon_0\epsilon_m}\left[\frac{1}{r^3}\right]. \tag{2.7}$$

Here, $p = \epsilon_0\epsilon_0\alpha E_0$ is the dipole moment, E_0 is the amplitude of the applied electric field, ϵ_{NP} and ϵ_m are the dielectric permittivity of the nanoparticle and its surrounding medium respectively, r is the distance from the core of NP to the point of observation. Equation 2.7 implies that the electric field in close proximity to the particle is highly dependent on the shape, size, and dielectric constant of the scatterer and the surrounding medium. The solution to this phenomenon explains the absorption and scattering cross section by a spherical particle with a diameter very less than the wavelength of the incident light. The sum of

these two cross-sections gives the extinction cross-section.

Scattering and absorption cross sections are calculated for a gold nanoparticle, with a refractive index of 1 for the surrounding medium (air). It is illuminated with a single wavelength source (laser) which can be tuned from 450-1100 nm. When the size of the particle is very small compared to the wavelength of the EM field (30 nm), the extinction is dominated by absorption while scattering increases with larger particles and dominates for sizes larger than 60 nm as shown in figure 2.1. The dependence of localized surface plasmon resonance on both nanoparticle size and the refractive index of the medium in which it is embedded is shown in figure 2.2.

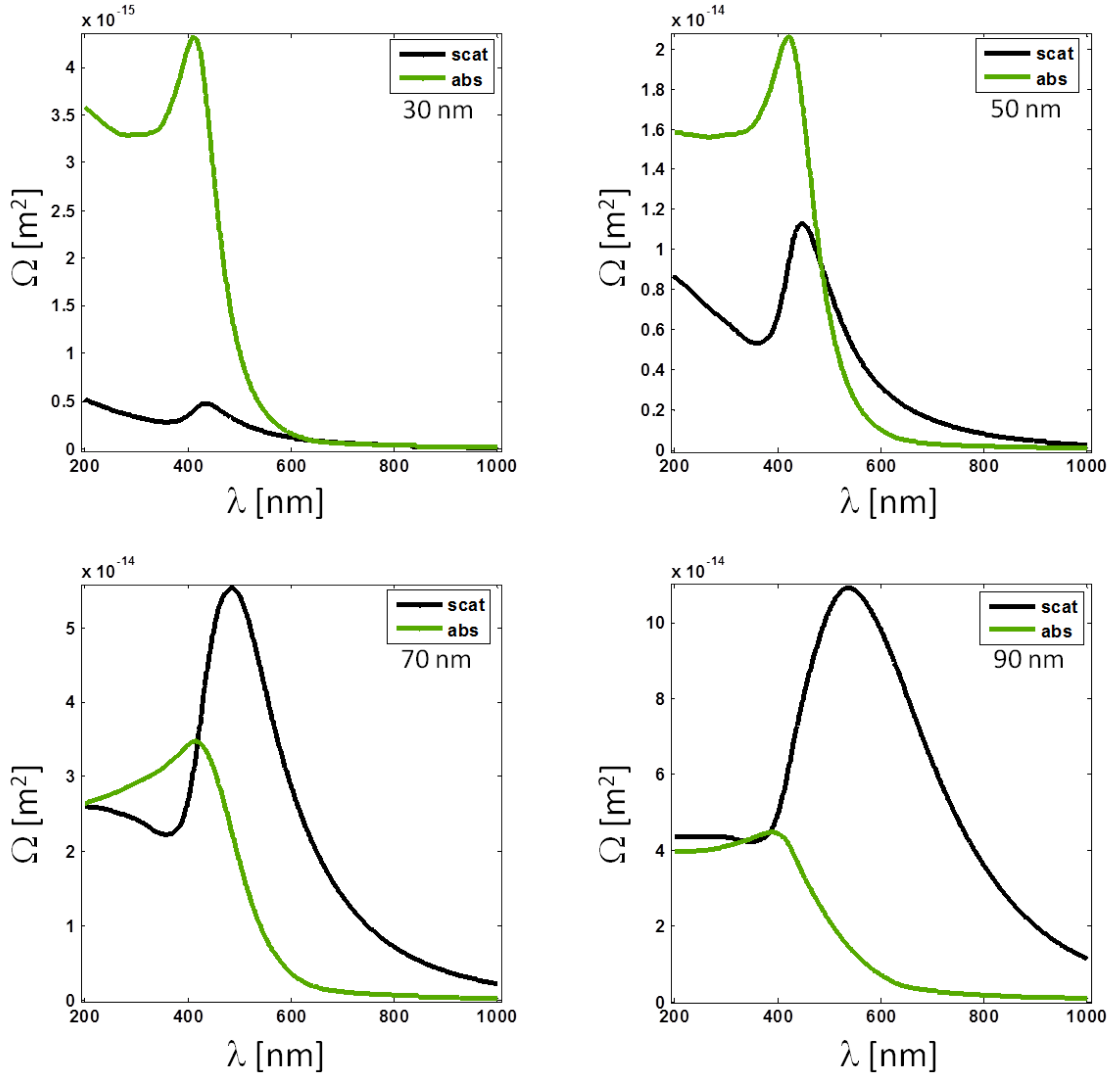

FIGURE 2.1 Absorption and scattering cross-sections vs. wavelength, for different radius of spherical NP, with air as the surrounding medium. The green and black curves correspond to the absorption and scattering cross sections respectively.

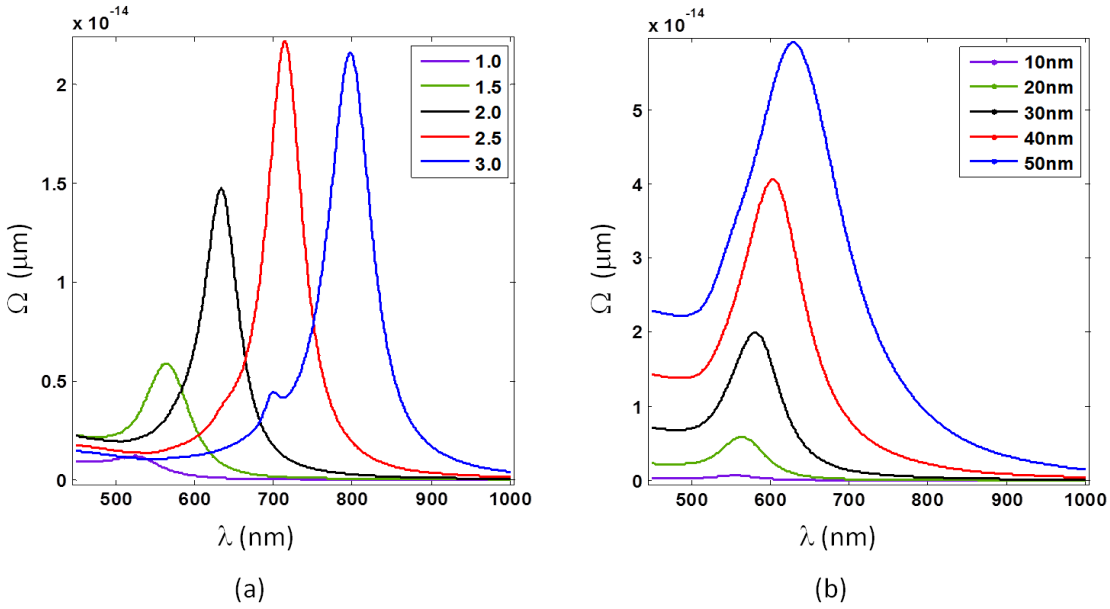

FIGURE 2.2 Extinction cross sections for gold particle calculated from Mie theory demonstrating (a) variations with different surrounding medium (refractive indices) and (b) nanoparticle sizes.

However, Mie theory is only accurate in this approximation for spherical NP for simplicity, since for other shapes, the solution to the Laplace equation can only be solved numerically.

2.3 Surface Plasmon Polariton

SPPs are collective electromagnetic flunctuations propagating at interfaces between a dielectric and a conductor, confined in the perpendicular direction, and in an evanescent manner. These collective oscillations are made by charge densities due to valence electron in a metal. When a metal is exposed to electromagnetic radiation, the charge densities couple with the incident beam to form localized surface plasmon. However, SPP can not be excited directly by illuminating a flat metal surface with light, due to the high momentum requirement. One of the ways to excite SPP is through Kretschmann configuration, where the large refractive index prism enables an evanescent field through attenuated total reflection to excites plasmons. Among other methods, one of the ways of exciting SPP is through diffraction grating coupling; where diffracted orders of incident light couple with surface plasmons on the metal-dielectric interface. In order to understand the physical properties of SPP, we apply Maxwell's equation to the medium through which they propagate.

$$\nabla \cdot \mathbf{E} = \frac{\rho_{\text{ext}}}{\epsilon_0}, \tag{2.8a}$$

$$\nabla \cdot \mathbf{B} = 0, \tag{2.8b}$$

$$\nabla \times \mathbf{E} = -\frac{\partial \mathbf{B}}{\partial t}, \tag{2.8c}$$

$$\nabla \times \mathbf{H} = \mathbf{J}_{\text{ext}} + \frac{\partial \mathbf{D}}{\partial t}. \tag{2.8d}$$

In the absence of an external charge source, and the current density, the curl functions can be simplified to

$$\nabla \times (\nabla \times \mathbf{E}) = -\mu_0 \frac{\partial^2 \mathbf{D}}{\partial t^2}, \tag{2.9}$$

and using the vector identity $\nabla \times (\nabla \times \mathbf{E}) = \nabla(\nabla \cdot \mathbf{E}) - \nabla^2 \mathbf{E}$, where $\nabla \cdot \mathbf{E} = 0$ in the absence of external stimuli. Equation 2.9 can therefore be written as

$$\nabla^2 \mathbf{E} - \frac{\epsilon}{c^2} \frac{\partial^2 \mathbf{E}}{\partial t^2} = 0. \tag{2.10}$$

Due to the oscillations of electrons about the fixed positive charge background, a harmonic time dependence $\mathbf{E}(\mathbf{r}, t)e^{-i\omega t}$ of the electric field can be assumed. Applying this to equation 2.10, we obtain the Helmholtz equation

$$\nabla^2 \mathbf{E} + k_0^2 \epsilon \mathbf{E}, \tag{2.11}$$

where $k_0 = \frac{\omega}{c}$ is the wave vector in the propagating wave in vacuum. When equation 2.11 is applied to electromagnetic surface wave problem in one dimension, where $z = 0$ coincides with the interface, and the surface wave is propagating with a propagating constant β, equation 2.11 can be written as

$$\frac{\partial^2 \mathbf{E}(z)}{\partial z^2} + (k_0^2 \epsilon - \beta^2)\mathbf{E} = 0. \tag{2.12}$$

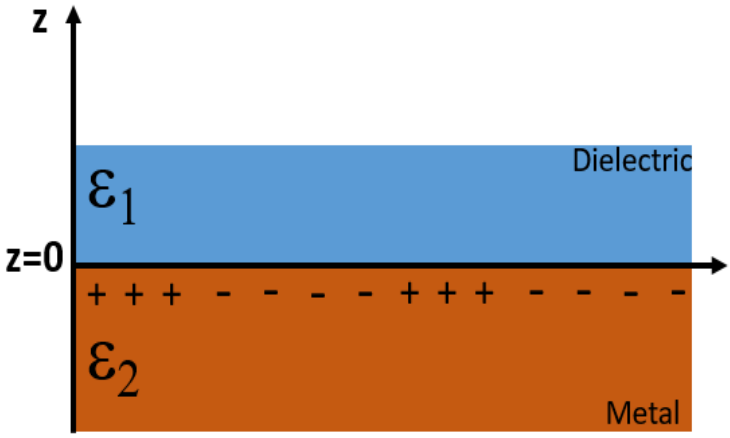

FIGURE 2.3 Charge distribution at the interface between a metal and dielectric with dielectric constant ϵ_1 and ϵ_2 respectively.

The TM solutions for equation 2.12 gives the following components of both the magnetic and electric fields

$$H_y(z) = Be^{i\beta x}e^{-k_2 z}, \tag{2.13a}$$

$$E_x(z) = iB\frac{k_2}{\omega\epsilon_0\epsilon_2}e^{i\beta x}e^{-k_z z} = 0, \tag{2.13b}$$

$$E_z(z) = -A\frac{\beta}{\omega\epsilon_0\epsilon_2}e^{i\beta x}e^{-k_z z} = 0, \tag{2.13c}$$

and for the region $z > 0$,

$$H_y(z) = A\exp i\beta x\exp -k_1 z, \tag{2.14a}$$

$$E_x(z) = iA\frac{k_1}{\omega\epsilon_0\epsilon_1}e^{i\beta x}e^{-k_1 z} = 0, \tag{2.14b}$$

$$E_z(z) = -A\frac{\beta}{\omega\epsilon_0\epsilon_2}e^{i\beta x}e^{-k_1 z} = 0, \tag{2.14c}$$

where k_1 and k_2 are imaginary and determine the decay of the electromagnetic field from the interface into medium 1 and 2 respectively as demonstrated in 2.3. Continuity conditions of H_y and E_z at the interface requires that $A = B$, and solving for k_1 and k_2 gives

$$k_1^2 = \beta^2 - k_0^2\epsilon_1, \tag{2.15a}$$

$$k_2^2 = \beta^2 - k_0^2\epsilon_2, \tag{2.15b}$$

where

$$\frac{k_2}{k_1} = -\frac{\epsilon_2}{\epsilon_1}. \tag{2.16}$$

Applying equation 2.16 in equation 2.15, we obtain the dispersion relation,

$$\beta = k_0 \sqrt{\frac{\epsilon_1 \epsilon_2}{\epsilon_1 + \epsilon_2}}. \tag{2.17}$$

Equation 2.17 is true for both the imaginary and real parts of the dielectric constant.

2.4 Surface Lattice Resonance

The advance in nanostructure fabrication has contributed to the progress in research on photonic properties of metallic NP. Localized surface plasmon resonance is supported by individual or small clusters of metal NP (NPs), leading to amplification of the incident electromagnetic field. However, arrays of NPs patched on a metal substrate have even larger local electromagnetic field enhancements in deep subwavelength volumes. The enhancement can be understood as a result of the interactions between the LSP at different particle site. This electromagnetic coupling can take several forms: via near-fields and via far-fields. Particles interact via near-field coupling when they are relatively densely packed, leading to significant spectral shifts of the plasmonic resonances and a modification and splitting of their line-shapes due to the hybridization of the plasmonic modes ("Plasmons in Strongly Coupled Metallic Nanostructures" 2011). The far-field interactions involve the scattered incident radiation from every nanoparticle site. Due to the orderly arrangement of the NP, the scattered field, under appropriate conditions can arrive in phase with the incident light. By tailoring the geometrical parameters of the nanoparticle, the period of the array, and the incident wavelength and angle of the elctromagnetic field, it is possible to make the diffracted field scattered in phase with the LSPR of different NP, thereby reinforcing the resonance in the neighboring particle. When extended over a large array of NP, the contribution from different particle sites can be so significant, and can produce a remarkably narrowed width as well as dramatic enhancement of the local electric fields near the nanostructures. The theoretical framework for surface lattice resonance has been based on coupled dipole approximation (CDA). In this approximation, the particles are replaced by sets of dipole units with scalar dipole susceptibility χ, interacting via dipole fields. The coupled-dipole equation is of the form:

$$d_i = \chi E_{in}(r_i) + \chi \sum_{j \neq i}^{\infty} \hat{D}(r_i, r_j) d_j, \tag{2.18}$$

where d_i is the dipole moment of the ith dipole unit, E_{in}, is the incident field at the point r_i where the ith unit is located, and $\hat{D}$ is the matrix of dipole interaction. Despite the well developed mathematical theory of the surface lattice resonance, the experimental realization is still in development.

2.5 Fano Resonance

In an ordered array of particles on metal thinfilms, different and more complicated resonances occur. Propagating surface plasmons, which occur on the continuous metal-dielectric interface, localized surface plasmon confined to the nanoparticle, and surface lattice resonance, resonating between NP, are the most common resonances in this type of structures. Fano resonance is an advance phenomenon that occurs in arrays of nanoparticle. It involves the coupling between a narrow discrete state, and a broad continuum that produces an asymmetric shape in the reflection spectrum. For a single spherical particle, Fano resonance can be derived from the Mie theory for a single spherical plasmonic particle. The resonance can be of both magnetic and electric resonances, or only one of the two. These resonances depend strongly on the size of the particle. The size parameter is related to the scattering cross-section as described by Rayleigh (Luk'yanchuk1 et al., 2010):

$$Q_{Scat} = \frac{8}{3}\frac{|\,\epsilon - 1\,|^2}{|\,\epsilon + 2\,|}q^4. \tag{2.19}$$

The above equation is obtained for a small-sized ($q << 1$) and non-magnetic particle ($\mu = 1$), where q represents the size parameter. With the increase in particle size, Maxwell's equations yield more eigenmodes that result in more resonances that lead to oscillations and contribute to the scattering efficiency. For dielectric optical materials ($\epsilon > 1$), all-optical resonances are broad (Luk'yanchuk et al., 2007), and consequently, can not lead to Fano resonance requirements for a Fano resonance, that is, the spectral overlap of broad and narrow resonances, cannot be fulfilled. However, with plasmonic materials, this is possible.The Fano resonance phenomenon exists in plasmonic nanostructures, where the continuum plasmon resonance couples with a discrete state to form a Fano resonant mode. The discrete state can be the excitation of a nanoparticular or the excitation of a diffraction channel.

2.6 Two-Photon-Luminescence

An electron de-excitation from an energy level above its ground energy after receiving an external energy from an incoming electric field produces an emission of photon whose energy is the difference between the two energy levels. This process is called photoluminescence. The two-photon luminescence microscopy is a nonlinear microscopy which uses the two-photon excitation and absorption. In this process an electron is excited from ground state by simultaneously absorbing two photon within a very short time to produce an emission of shorter wavelength and consequently more energetic. Both the one-photon and two-photon processes are shown in the figure 2.4.

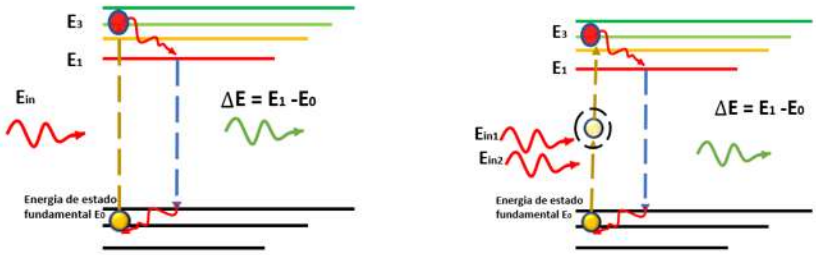

(A) (B)

FIGURE 2.4 (A) A one-photon absorption and (B) a two-photon absorption of photon by an electron at ground energy level thereby causing it to excite. After the electron is excited the relaxation and emission process remain same.

To observe all nonlinear optical effects, a high-intensity focused electromagnetic radiation source is needed. For this reason, nonlinear optics did not become popular until the invention of lasers. Nonlinear optical materials are those which optical properties can not be determined by the intensity of the applied field. When they are exposed to an EM field, their atomic and molecular configurations are altered, which basically is the displacement of valence electrons from their actual energy level. The manifestation in macroscopic scale is the polarization. The relationship between the applied electric field and the polarization effect shown by this class of materials is given by

$$P(r,t) = \epsilon_0 \overleftrightarrow{\chi}^1 E(r,t) + \epsilon_0 \overleftrightarrow{\chi}^2 E^2(r,t) + \epsilon_0 \overleftrightarrow{\chi}^3 E^3(r,t) + ..., \tag{2.20}$$

Where $\overleftrightarrow{\chi}^1, \overleftrightarrow{\chi}^2, \overleftrightarrow{\chi}^3$... are first, second, and third order susceptibilities respectively and ϵ_0 is the vacuum permittivity.

At a relatively low incident electric field, the response of a material is predominated by the first-order (linear) while the nonlinear response increases with the incident electric field. Second-Harmonic Generation (SHG) assumes the domination of the second-order nonlinear response to the electric field where both the susceptibility and the electric field are functions of two frequencies as shown in equation 2.21

$$P(r,t) = \epsilon_0 \overleftrightarrow{\chi}^2(\omega_1, \omega_2) E(\omega_1,) E(\omega_2). \tag{2.21}$$

While the first harmonics (FH) directly relates to the refractive index, the nonlinear interactions is highly sensitive to material shape and symmetry and this has been the reason in the recent interests and investigations in its optical effects at surfaces. The experimental work in this thesis treats all the nonlinear components as a single entity, since, an experimental setup that is capable of resolving different components is a highly expensive one, and consequently not available at this time in the laboratory. However, it is intuitive to infer that the major components in the nonlinear responses obtained in this way, is the second-order susceptibility nonlinear component.

Chapter 3

FDTD

3.1 Introduction to Finite Difference Time-Domain

Finite difference Time–domain (FDTD) is unarguably one of the most common, and simplest tools for mathematical solutions to electromagnetic problems. FDTD solves Maxwell's equations in time domain, using finite-difference approximations of the spatial and temporal derivatives of the Maxwell's curl equations. This method was first introduced by Kane S. Yee in 1966 (Yee, 1966) and applied in 1975 by Taflove and Brodwin to simulate scattering by dielectric cylinders (A.Taflove and Brodwin, 1975a), and microwave-irradiation of the human eye (A.Taflove and Brodwin, 1975b). The availability of sophisticated computation machines in recent years has geared interests in the method, and its application has been consequently and continuously increasing as newer computer technologies evolve. Being a solution in time–domain, FDTD provides a visual interpretation of the response of an object to electromagnetic radiation as a function of time. This creates a "moving" field flowing through the propagating medium. Ever since the introduction of FDTD, the method has been significantly improved through different modifications and applications (G.Mur, 1981; Higdon, 1986; R.L.Higdon, 1987; Betz and Mittra, 1992; Berenger, 1994; Berenger, 2007), most of which tend to solve boundary condition problems, and stability complications. This section is not intended to serve as a complete guide to FDTD, but to mention some fundamentals based on which the calculations in this thesis were made. More detailed information on the method can be found in literature (Stephen, 2011; Taflove, 1984) for general understanding.

3.2 Theory

The mathematical foundation of FDTD roots in the application of finite difference method to solving differential equations. In light-matter interactions, the formulation is used in solving the differential form of Maxwell's equation in time domain.This method requires discrete samples of f(x) at two points that have their center at x. Given that Δx is small enough. The two curl Maxwell's equations in a homogeneous, non-magnetic medium is

given below

$$\frac{\partial \mathbf{E}}{\partial t} = \frac{1}{\epsilon_0}\nabla \times \mathbf{H}, \tag{3.1a}$$

$$\frac{\partial \mathbf{H}}{\partial t} = \frac{1}{\mu_0}\nabla \times \mathbf{E}. \tag{3.1b}$$

For simplicity, one-dimensional solutions of equations 3.1a and 3.1b are

$$\frac{\partial \mathbf{E}_x}{\partial t} = -\frac{1}{\epsilon_0}\frac{\partial \mathbf{H}_y}{\partial z}, \tag{3.2a}$$

$$\frac{\partial \mathbf{H}_y}{\partial t} = -\frac{1}{\mu_0}\frac{\partial \mathbf{E}_x}{\partial z}, \tag{3.2b}$$

which represents an electromagnetic wave propagating in the Z-direction. Applying the central difference approximation to equations 3.2a gives

$$\frac{\mathbf{E}_x(\Delta t + \frac{\Delta t}{2}) - \mathbf{E}_x(\Delta t - \frac{\Delta t}{2})}{\Delta t} = -\frac{1}{\epsilon_0}\frac{H_y(\Delta z + \frac{\Delta z}{2}) - \mathbf{H}_y(\Delta z - \frac{\Delta z}{2})}{\Delta z}, \tag{3.3a}$$

$$\mathbf{E}_x(\Delta t + \frac{\Delta t}{2}) = \mathbf{E}_x(\Delta t - \frac{\Delta t}{2}) - \frac{\Delta t}{\epsilon_0 \Delta z}\left[\mathbf{H}_y(\Delta z + \frac{\Delta z}{2}) - \mathbf{H}_y(\Delta z - \frac{\Delta z}{2})\right]. \tag{3.3b}$$

The electric field obtained at time $(t + \frac{\Delta t}{2})$ from equation 3.3b will then be used to calculate the magnetic field using equation 3.4a.

$$\mathbf{H}_y(k + \frac{1}{2}) = \mathbf{H}_y(k + \frac{1}{2}) - \frac{\Delta t}{\mu_0 \Delta z}\left[\mathbf{E}_x^{n+\frac{1}{2}}(k+1) - \mathbf{E}_x^{n+\frac{1}{2}}(k)\right], \tag{3.4a}$$

where the terms $\frac{\Delta t}{\mu_0}$ and $\frac{\Delta t}{\epsilon_0}$ in equations 3.3b and 3.4a respectively are called update coefficients. These terms can be calculated ahead as a constant and do not necessarily need to be computed in the loop, since they are constants of calculation.
Equation 3.4a implies that to find the electric field at a future time (n+1) Δt, we use the electric field of the present time and magnetic field at positions (k+1/2) Δx and (k-1/2) Δx. These approximations require us to always calculate values of E field at points (k-1) Δx, k Δx, (k+1) Δx,... and times (n-3/2) Δt, (n-1/2) Δt (n+1/2) Δt, ... and to calculate H field always at points (k-3/2) Δx, (k-1/2) Δx, (k+1/2) Δx, ... and at times (n-1) Δt, n Δt, This is known as leap-frog algorithm. This implies that to approximate Maxwell's equations in space and time, the H field is first calculated, followed by the E values. The choice of Δz and Δt determines the resolution of our calculation. It has been verified that at least 10 cells per wavelength are necessary in a simulation, considering the smallest wavelength for a broadband simulation (A.Taflove and Brodwin, 1975a). After selecting the cell size, the time step is chosen according to stability considerations. For stability to occur, a field component cannot propagate more than one cell size in time step Δt. This condition for

one-dimensional problems is

$$\Delta t \leqslant= \frac{\Delta z}{c_0}, \tag{3.5}$$

and for more than one-dimensional cases,

$$\Delta t \leqslant= \frac{\Delta}{c_0\sqrt{d}}, \tag{3.6}$$

where Δ is the smallest cell size and d = 1, 2, or 3 for one, two, or three-dimensional problems, respectively.

3.3 Boundary Conditions

3.3.1 Absorbing Boundary Conditions

One of the ways to introduce stability in FDTD method is the introduction of absorbing boundary conditions (ABCs). ABCs employ the use of artificial numerical boundaries of a computational domain to minimize or eliminate the non-physical reflections at these boundaries, which occur in the simulations of wave propagation phenomena. The quest for an ABC that produces minimum reflections has been an active research topic in FDTD. There are basically two types of ABCs: ABCs derived from differential equations or ABCs that employ a material absorber. An example of the formulations that use a material absorber is the perfectly matched layer (PML). The PML technique was proposed by Berenger in 1994 (Berenger, 1994; Berenger, 2007), and this method has been shown to efficiently stabilize the numerical calculations and improve accuracy. Berenger's original method is called the split-field PML because it splits the wave solution into the sum of new artificial field components. Another common formulation involves expressing the PML region as an ordinary wave equation with a combination of artificial anisotropic absorbing one-dimensional stacks. Both the split-field and the PML formulations were originally derived by laboriously computing the solution for a wave incident on the absorber interface at an arbitrary angle and then solving for three-dimensional cases in which the reflection is always zero.

3.3.2 Periodic boundary conditions

Many structures of interest in electromagnetic interactions have periodicity in one or more dimensions. The periodic boundary conditions (PBCs) are a set of equations applied to a small domain in a way that the domain can be replicated through the different dimensions of the model. FDTD, can be applied to the study of infinite array of structures, which inevitably comes with computational problems due to replicas of basic elements. One way to reduce these complications is to model only one element and use periodic boundary conditions to simulate the effect of periodic arrangement. In this way, PBCs permit us to calculate the response to the complete array by only simulating one unit cell. For plane waves incident at normal to the surface, the difficulty that arises in the time domain does not exist. This is because at normal incidence, the wavefront has no spatial tilt, nor time delay or

advance. Therefore, when the simulation runs, the PBCs simply copy the electromagnetic fields that occur at one side of the simulation window and inject them at the other side. For an incidence angle different from normal, the field will possess a phase difference at the two sides of the simulation window, the Bloch boundary conditions can be used instead in this case.

3.4 Limitations of FDTD Method

As simple and intuitive FDTD method is, it is not without limitations. It is therefore important, to identify these limits, as they affect the accuracy, and in some cases, acceptability of the results. One of the limitations arises from the discretization of the magnetic and electric field over the entire volume of the computation window. This consequently leads to increased computation resources and more simulation time. Another limitation that FDTD provides, is a broad-band simulation, and this results in a broad frequency response. However, there are times when only a narrow band response is desired. This type of simulation will be better performed using a frequency-domain simulation.

3.5 Lumerical FDTD Solution

Lumerical FDTD solution software was used for the simulations of plasmonic structures in this thesis. The structures were designed using the geometry menu of the software and their optical constants are interpolated from experimental data. John and Christy experimental data was used in the results presented in this study. The material database in the software contains dielectric constants for many dispersive materials. However, some materials whose refractive indices are not included in the software can be defined manually or imported. The FDTD region in the software determines the background properties, the simulation area and boundaries.

After definition of the simulation area and sample structure, the next step will be adding source and monitors. The program permits the use of Gaussian source, mode source, and plane wave source. In this work, a broadband plane wave source is positioned in the FDTD region (air), and above the sample to be studied. For best performance, physical structures should extend completely through the PML boundary condition region. The incident plane waves can be controlled by changing the wavelength range of the spectrum, polarization state, and the incident angle. The monitors can be placed in different planes to measure the S-parameters in different directions. The vertical distance of the monitor can be at about 20-60 nm to observe the near-field effect. However, convergence test must be performed before fixing a sample/monitor distance to avoid any divergence due to back-reflections.
The third step is meshing. The mesh set in FDTD simulations is a function of both the material property and the input spectrum. For stability and convergence to occur, the condition

in 3.6 must be satisfied. The finer the mesh is, the more computational resources required. However, after convergence is achieved, further reduction of the mesh size will only contribute more numerical errors. The unit cell of a periodic array of nanoparticle is shown in fig. 3.1, showing the source, monitor, FDTD region, mesh, and the sample as described above.
The recorded data can further be exported to a third-party application software for advance data processing and visualization. The script interface allows for data export into csv, mat, pjeg formats.

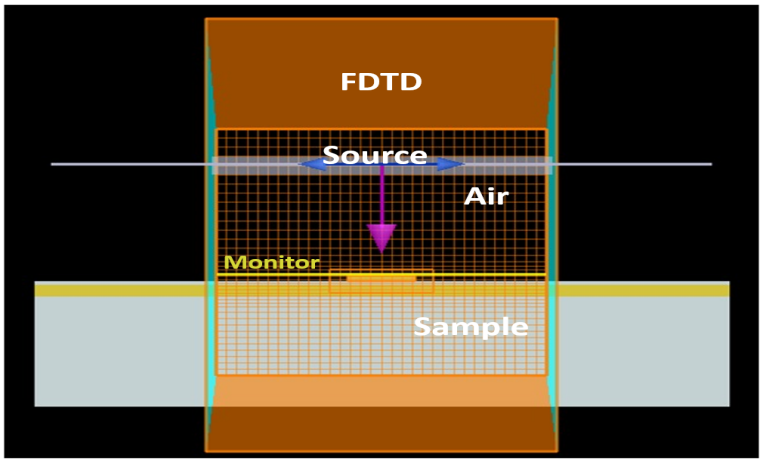

FIGURE 3.1 Charge distribution at the interface between a metal and dielectric with dielectric constant ϵ_1 and ϵ_2 respectively.

3.6 Application of Finite Element Method in Solving Optical Problems

The Finite Element Method (FEM) finds wide application in solving optical problems, particularly in the analysis of light propagation, waveguides, optical devices, and electromagnetic interactions. The FEM allows for the accurate modeling and simulation of complex optical systems by discretizing the problem domain into smaller finite elements. This approach enables the numerical approximation of optical phenomena and the computation of important parameters such as field distributions, scattering, and transmission characteristics.

Mathematical Descriptions:

1. **Maxwell's Equations:** The governing equations for electromagnetic fields in optical problems are described by Maxwell's equations. These equations establish the relationships between the electric field ($\mathbf{E}$) and the magnetic field ($\mathbf{H}$) in the presence of sources and materials. In optical problems, typically the time-harmonic form of Maxwell's equations is used, where the fields vary sinusoidally with time.

2. **Electromagnetic Wave Equation:** By combining Maxwell's equations, one can derive the wave equation governing the behavior of electromagnetic waves in optical systems.

The wave equation relates the spatial variation of the electric field or magnetic field to its temporal variation. It is typically represented as:

$$\nabla^2 \mathbf{E} - \frac{1}{\varepsilon\mu}\frac{\partial^2 \mathbf{E}}{\partial t^2} = 0 \tag{3.7}$$

where ∇^2 denotes the Laplacian operator, ε is the permittivity, μ is the permeability, and $\frac{\partial^2 \mathbf{E}}{\partial t^2}$ represents the second time derivative of the electric field.

3. **Discretization:** In the FEM, the problem domain is divided into finite elements, which can be triangles, quadrilaterals, or tetrahedra depending on the dimensionality of the problem. Each finite element is characterized by a set of nodes and associated shape functions that approximate the behavior of the electric field within the element. The electric field is then expressed as a linear combination of the shape functions and nodal values.

4. **Element Equations:** By applying the variational principle, the weak form of the wave equation is established. This involves multiplying the wave equation by a weight function and integrating over each finite element. By substituting the approximation of the electric field and weight functions into the weak form, the element equations are obtained. The element equations express the relationship between the nodal values of the electric field within an element.

5. **Assembly:** The element equations are assembled to form a global system of equations that represents the entire problem domain. This assembly process involves accounting for the connectivity between elements and enforcing continuity at element interfaces. The global system of equations is usually large and sparse, reflecting the size and interconnectedness of the finite elements.

6. **Solution and Analysis:** The global system of equations can be solved using numerical methods such as direct solvers or iterative techniques. The solution yields the nodal values of the electric field, which can be used to determine various optical properties such as intensity, phase, polarization, and transmission characteristics. Post-processing techniques can be applied to extract useful information, including field distributions, dispersion curves, or the behavior of light in waveguides and photonic devices.

In conclusion, the Finite Element Method provides a powerful tool for solving optical problems by numerically approximating the behavior of electromagnetic fields. By discretizing the problem domain into finite elements and utilizing the principles of variational calculus, the FEM enables the accurate modeling and simulation of complex optical systems. This approach allows for the analysis of light propagation, waveguides, optical devices, and electromagnetic interactions, providing valuable insights into the behavior of light in various applications.

Chapter 4

EXPERIMENTAL DEVELOPMENT

4.1 Atomic Force Microscopy

Atomic force microscope (AFM) uses a very powerful microscopy technique that enables the imaging of any type of surface at nanoscale. The scanning tunneling microscopy, which had been used earlier has a lower resolution when compared to AFM, and also limited to only conducting surfaces including ceramics, polymers, etc. AFM consists of a cantilever and a nano-meter sized sharp probe integrated near the free end of the cantilever. The sharp probe is usually made with silicon or silicon nitride, and it's made to scan over the sample in a raster pattern along an x-y grid. An electronic feedback loop is commonly set to keep the probe-sample force constant. The input of the feedback loop is the cantilever deflection, and it's output is the distance along the z-direction between the probe and the sample. As long as the tip remains in contact with the sample, and the sample is scanned in the x-y plane, height variations in the sample will change the deflection of the cantilever. The feedback then adjusts the height of the probe support so that the deflection is restored to a user-defined value. An AFM operates basically in two modes; contact mode, and tapping mode. In contact mode, the probe is in continuous contact with the surface, and the roughness of the surface is measured using the deflection of the cantilever. On the contrary, in the tapping mode, the cantilever is oscillated above the sample surface in a way that the probe tip slightly touches the sample surface, and the interaction force is recorded and set back to an initial value by the feedback loop. For application purposes, the tapping mode is the recommended mode for imaging surfaces, while the contact mode is used in specific applications such as force curve measurements.
In this thesis, we used AFM to image and characterize the surfaces of arrays of nano patches, operating in the tapping mode, and controlled with nanosurf computer application software. In this way, the periods, and the heights of the samples were measured with the help of a third-party image processor such as MATLAB. The images in fig. 4.1 shows the AFM image obtained for triangular shaped copper NP with the equipment at CICESE-Monterrey laboratory as at the time this doctoral work is done.

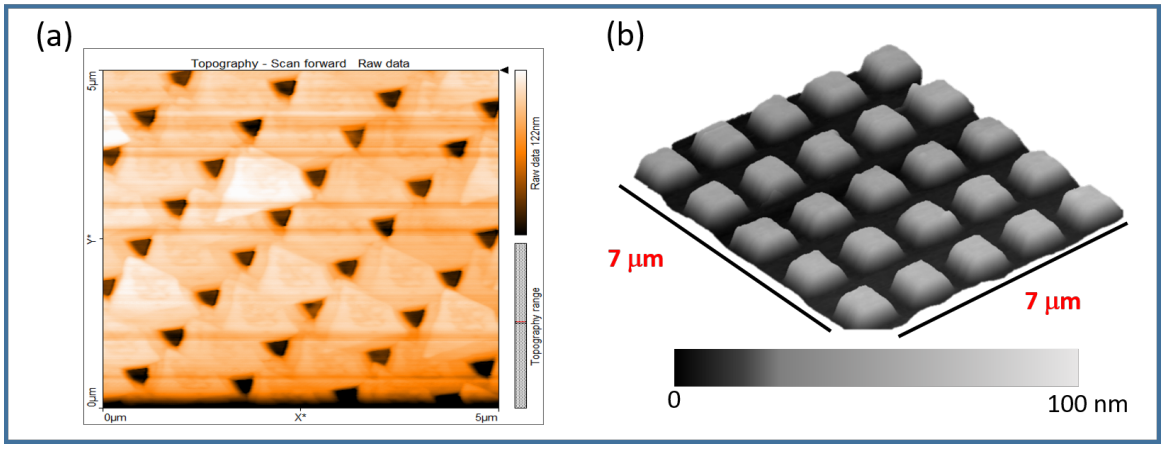

FIGURE 4.1 Atomic force microscopy showing a (a) 5x5 mm^2 2-D arrays of triangular shaped copper NP, (b) 3-D image of square gold NP, used in the characterization of topography and dimensions.

4.2 Two-Photon Luminescence

4.2.1 The Laser

A relatively strong electric field is required to observe nonlinear effect of materials. However, it also poses considerable risk of damaging samples if used at continuous illumination. This damage is avoided in laboratory by using ultra-short fs-pulses with intensity which can be enhanced by a factor up to 10^5 or more without increasing the average intensity that could damage the material. The experimental setup used to measure the nonlinear responses is shown in fig. 4.3. The setup consists of a Ti:Saphire pulse laser with an average power of 300 mW, repitition rate of 80 MHz, and a pulse duration of about 200 fs. With this specification, the energy of a single pulse is about $3.8x10^{-9}J$. The laser is tunable and it emits between red and near-infrared light in the range of 500 to 1100 nm. The operational wavelength range at mode-locking mode is shown in fig. 4.3. For pulse laser, the peak power, average power, pulse width, and repetition rate, are not mutually exclusive, hence, the peak power was adjusted to obtain different spectral shown in fig. 4.2.

4.2.2 Spot size characterization

To overcome the limitations imposed by Abbe diffraction in optical devices, it is crucial to have a well-defined and characterized laser spot before conducting experiments that involve varying wavelengths. The changes in wavelength necessitate an understanding of how the size and shape of the spot are affected by the optics in the experimental setup. In this study, the beam was expanded and collimated using a combination of positive and negative lenses to reduce the average power per unit area at the sample. Additionally, a converging lens was placed to focus the collected nonlinear signal just before the avalanche photodiode (APD).

The spot size measurement in this experiment followed the criterion of full-width at half-maximum (FWHM), which is measured from the intensity distribution curve along a predefined axis passing through 0.135 of the maximum intensity. Two methods were employed to characterize the spot size: the razor edge method and the charge-coupled device (CCD) image method. Due to experimental fluctuations, the CCD method was found to be more precise and preferable. By calibrating the reflected image's pixels using a known scale, both vertical and horizontal profiles of the points were obtained. These profiles were then fitted with a Gaussian function to determine the beam diameter. This process was repeated for different wavelengths to observe the distortion resulting from the Abbe diffraction limit.

Using the aforementioned techniques, the spectral beam waist was measured to be approximately 950 nm at a wavelength of 800 nm, and used in all the experiments unless otherwise stated.

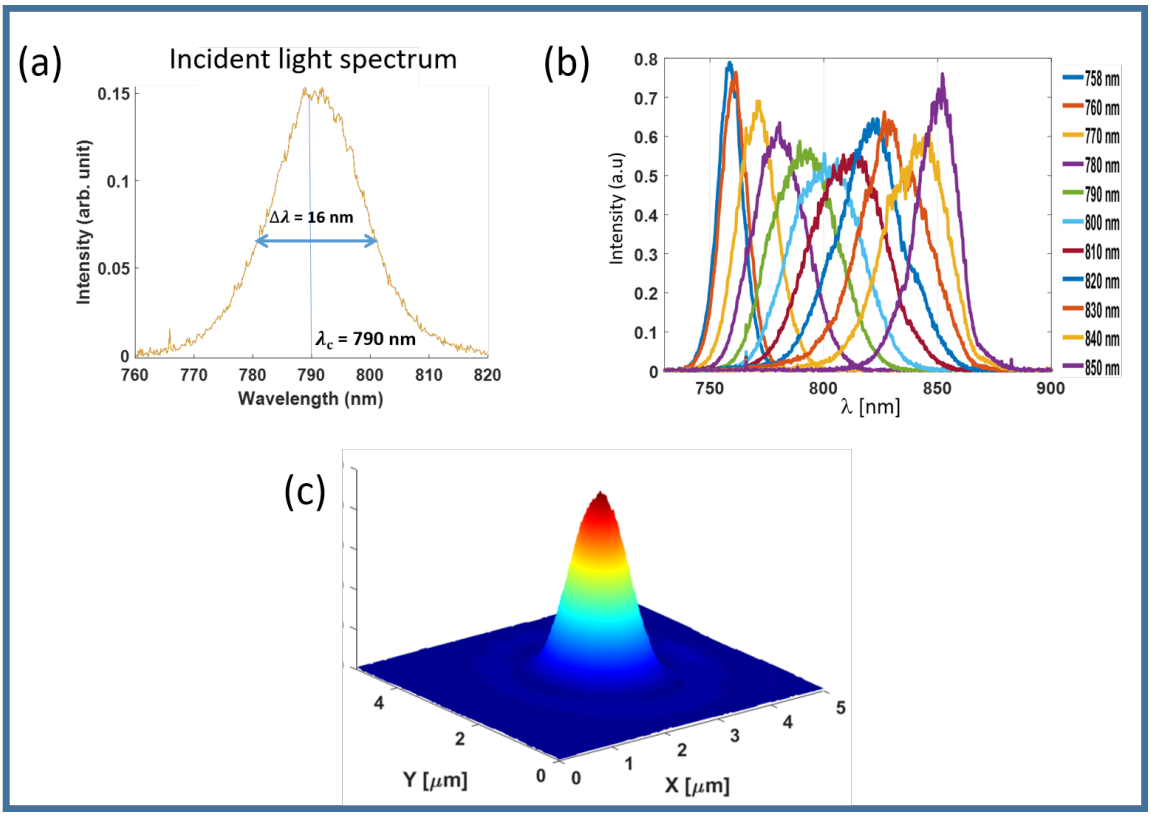

FIGURE 4.2 (a) A laser pulse profile measured with a CCD array spectrometer. A laser pulse width of about 1.3 ns was produced at an average power of 30 mW, peak power of 3 W, and repetition rate pf 80 MHz. (b) Tunability of the mode-locked Ti:Saphire laser within a wavelength range of about 100 nm. (c) The Gaussian representation of the beam spot of the laser source with 3 W.

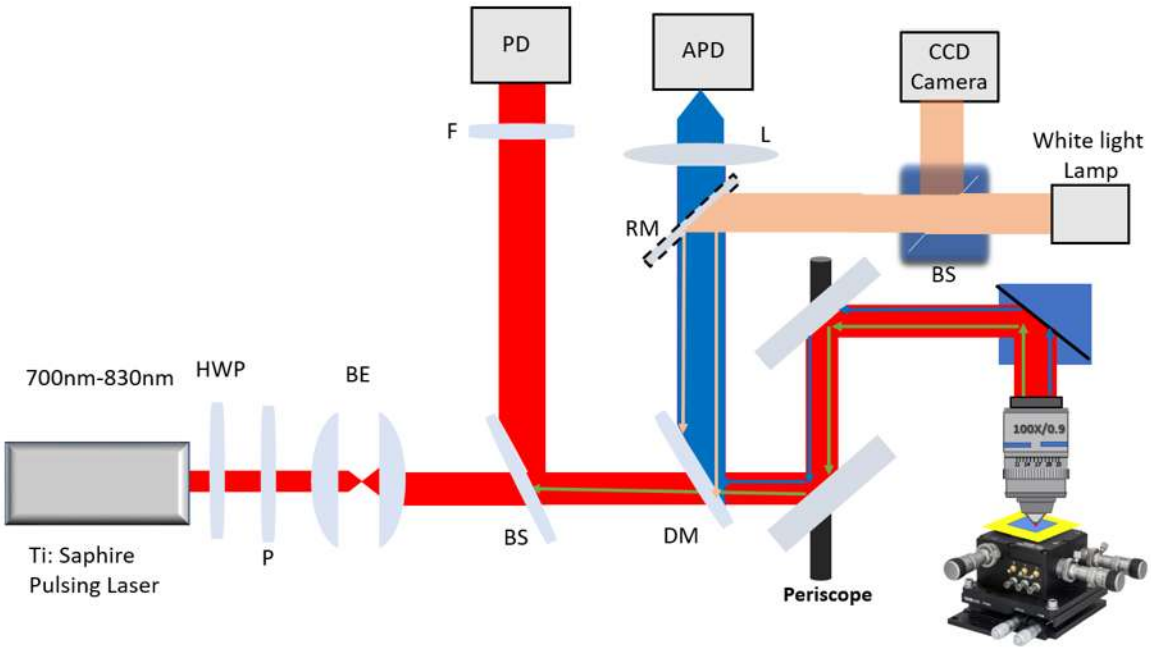

FIGURE 4.3 The experimental setup for recording two-photon luminescence with Ti:Sapphire laser, optical isolator (IO), Half-wave plate (HWP), Polarizer (P), Beam splitter (BS), Filters (F1 and F2), Wavelength selective beam splitter (WSBS), Analyzers (A1 and A2), Photomultiplier Tube (PMT), Photodiode (PD).

4.2.3 Experimental Setup of Two-Photon Luminescence

The sample is mounted on a computer-controlled two-dimensional piezoelectric stage capable of moving in steps down to 50 nm (with accuracy of 4 nm) within a scanning area 25x25 mm^2 allowing for a sample scanning in the x-y plane. The part of the experimental setup used to change the polarization state of the incident laser beam comprises a combination of a polarizer and a half-wave plate (HWP). To avoid saturating the half-wave plate and the polarizer with too much laser light, we include a neutral density filter just before the half-wave plate. Both the neutral density filter and the HWP with the polarizer are oriented so that the laser beam is perpendicular to all optical surfaces and passes through the centers of all optical devices. The laser beam is brought to focus on the sample, with the use of an X100 objective with numerical aperture of 0.9. The responses which include both linear and nonlinear are collected in the far-field back-reflection geometry following same optical path as in the incident beam but in the reverse direction. The nonlinear radiation is reflected by the dichroic mirror (DM) with transmission above the FH wavelength and collected at a photo multiplier tube (PMT) while the FH is transmitted through and detected with a photodiode. The analyzer placed before the photodiode is to attenuate the FH luminescence to avoid saturation of the FH response image. The removable mirror (RM) is used to obtain the images of the sample using the camera and illumination lamp during the sample search and focusing processes. Both FH and SH signals are simultaneously recorded as a function of the sample coordinates resulting in FH and SH images of the sample surface by using a computer specific program for automation and result processing. The data collection and processing involves using the LabView computer program to control piezoelectric stage, store the captured optical response in matrix form, and then processed by a third-party computer program such as MATLAB. With the possibility of moving the focus in steps of as little as 50 nm, the image resolution can be controlled, though the beam spot size, and environmental vibrations will also need be put in consideration.

4.3 Conclusion

This chapter presents some of the techniques applied in the characterization of samples and the experimental setup that will be used for all TPL experiments presented in the remaining chapters of this thesis. Characterization of samples is done by using AFM operating in tapping mode and scanning optical microscopy. TPL requires a relatively strong electric field to observe the nonlinear effect of materials but it also poses a considerable risk of damaging samples. This damage is avoided in the laboratory by using ultra-short fs-pulses. A Ti:Saphire pulse laser is used to generate the required pulse. The spot size of the laser is varied by Abbe diffraction, making it necessary to know the variations in the size and shape of the spot introduced due to the optics in the experimental configuration. The beam is expanded and collimated using lenses, and a converging lens is located to focus the parallel collected nonlinear signal just before the Avalanche photodiode (APD). The spot size measured by using couple-charge device image is the full-width at half-maximum, measured from the beam intensity distribution curve along a predefined axis passing through 0.135 of

the maximum intensity. The spectral beam-waist measures about 950 nm at 800 nm wavelength. The University of Southern Denmark collaborated in the fabrication of the samples, which were created using Electron Beam Lithography (EBL), unless stated otherwise.

Chapter 5

Surface lattices resonace

5.1 Introduction

Arrays of nanostructure have gained increasing attention in the research of the diverse fields of nanotechnology. This is due to different plasmonic resonances that occur when light is made to interact with this type of structure at a subwavelength scale. These plasmonic resonances are generally divided into two classes; localized surface plasmons (LSP) and SPP. While SPPs are the collective propagation of electromagnetic waves due to mobile electronic charges on metallic interfaces in metal-dielectric configurations, LSPs are associated with the collective non-propagating oscillation of free electrons, tightly bound to a metallic surface. The study of these plasmonic modes has received so much attention, owing to their potential applications in biosensing/biorecognition, nano-circuitry, waveguiding, environmental monitoring, and LED lighting applications (Colburn, 2018; G. E. Lio and Caputo, 2015; Lio, 2020; Lio, 2021; Ghindani, 2021; R., 2021). The applicability of this plasmonic mode is due to resonance frequency dependence on particle size, shape, and dielectric environment. SPPs on the other hand can be excited on a 2-D metal-dielectric interface and have been widely studied to apply in areas such as waveguiding, optoelectronics, and nano lens (C. Garcia-Ortiz and Garcia-Ortiz, 2019; Horton, 2020; Y. Xu and Li, 2013; C. Garcia-Ortiz and Bozhevolnyi, 2019; G. E. Lio and Caputo, 2020). However, due to the high momentum mismatch between the optical frequency in the visible light spectrum and the natural oscillating frequency of rare-earth metals, the applications of LSP and of SPP have been limited. Compared with individual and small clusters of NPs, metal particles organized into ordered arrays with spacings comparable to the wavelength of light, and fabricated on a metal thin-film can diffract incident light to couple with SPP and produce greater field enhancements and higher quality resonances which resonates in-between the NP. This diffractively coupled resonance will be referred to as the surface lattice resonance (SLR) in this article. When metal NP (nanoantennas) are arranged in a periodic manner, where the pitch is comparable to the wavelength of incident light under suitable conditions, the collective diffracted fields from the particles arrive in phase with the incident light. Though SLRs occur at wavelength very close to the array pitch (for (0,1), (1,0), (0,-1), (-1,0) modes), they have been characterized with significantly narrow FWHM down of a few nanometers compared to the incident wavelength (B. Lamprecht and Aussenegg, 2000; Humphrey and Barnes, 2018; J. Gömez-Correa and Chávez-Cerda, 2017; X. Yang

and Li, 2020; R. Tellez-Limon and Blaize, 2017; X. Yang and Li, 2019; N. Mahi and Gontier, 2017; A. Ferraro and Caputo, 2022). This translates to high quality factor of $\sim$ 105, which corresponds to about 25X of the LSP resonance for a gold free particle. However, in this type of nanomaterials, the 2-D plasmonic properties (localization and propagation length) are difficult to observe simultaneously in the same experimental setup. To have a 3-D view where both properties can be studied concurrently, the gap surface Plasmon (GSP) nanostructures which are composite of structure composed of a dielectric layer sandwiched between two layers of a metal film is introduced. In this more complex system, a new plasmonic mode has been reported to exist in the dielectric medium between the arrays and the thin film. This resonance exists as a result of nearfield coupling (NFC) between the SPP at each metal-dielectric interface in a MIM configuration (F. Ding and Bozhevolnyi, 2018; G. Lio and Luca, 2020; Bozhevolnyi, 2006). Here, we use the metal-insulator-metal (MIM) to demonstrate the dependence of GSP on the thickness of the dielectric spacer, and how this can be used to tune the plasmonic resonance within the near-infrared domain, therefore making it applicable in optical waveguiding, and sensor applications. We begin the investigation by observing how SPP and the SLR modes are excited in arrays of different periods. Furthermore, we investigate in detail how the dielectric gap thickness influences the hybridization between SLR and GSP.

5.2 Sample Description and Methods

The sample investigated in this paper consists of a dielectric spacer, sandwiched between a gold substrate and an array of gold nanoblocks. The parameter set for functional device optimization includes period (Λ), infinitely thick metal substrate thickness, dielectric thickness (t), nanoblock length (L), and nanoblock height (h) (fig. 5.1). To optimize the structures, we performed a 3D numerical modeling based on FDTD method. A periodic boundary condition is applied at the walls perpendicular to the unit cell to simulate an infinite array and uniaxial anisotropic PML in the walls parallel to the sample. The background refractive index of air at room temperature (T=300 K) is used, and the dielectric constants of gold were extrapolated from Johnson and Christy experimental results, while the optical constants of SiO_2 spacer were extracted from Palik experimental data. In order to sufficiently absorb energy flowing at grazing incidence, the number of PML layers is set to 12. A mesh size of 5x5x5 nm^3 in space and 2x2x2 nm^3 around the NP are applied. With a time step of 0.0095 fs corresponding to a stability factor of 0.5 and a simulation time of 1500 fs, convergence was achieved. A Gaussian wave packets composed of plane waves with the wave-vector parallel to the surface impinges onto the structure from normal incidence.

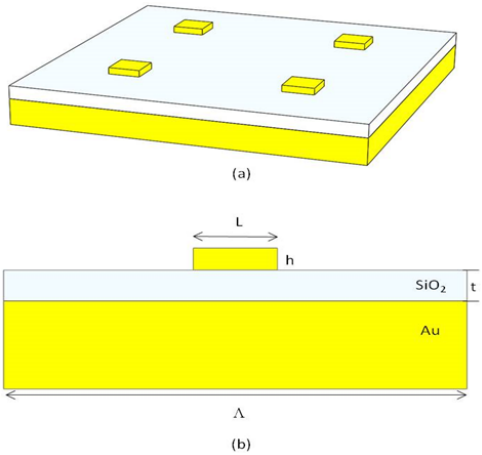

FIGURE 5.1 (a) 3-D Schematic of the structure composed of periodic square Au NP. (b) 2-D representation of a unit cell showing Au NPs with sides L, height h, and period L, fabricated on gold film with infinite thickness, and separated by a dielectric spacer layer of thickness t.

5.3 Results and Discussion

As a first approach, we calculate the reflection spectra of the MIM structure under normal incidence with x-polarized plane waves for different periods. Fig. 5.2 shows the reflection spectra for arrays with periods $\Lambda_x = \Lambda_y = 650$, 750, 850, and 950 nm. Though a metal thin-film of 100 nm thick will produce the same result, the metal thin-film is infinitely thick, enough to suppress the transmission practically to zero. The particle height and length are fixed at 50 nm and 200 nm respectively, and the dielectric gap thickness is fixed at 25 nm, similar to fabrication parameters in (Hohenau et al., 2007). The reflection spectra show distinct resonances in three wavelength regions. The broad resonance centered at about 1150 nm is common across all the periods and apparently independent of the array periodicity. This is associated with the excitation of a plasmonic mode which is localized inside the dielectric gap, and due to the near-field coupling (NFC) between the SPPs of the individual metal interface. The narrow deep resonance found at almost the grating period is the (SLR), which occurs due to the excitation of SPPs by diffraction orders of the incident beam and is governed by the famous Bragg formula, simplified as

$$\lambda_{SLR} = \frac{\Lambda}{\sqrt{m^2 + n^2}.} \tag{5.1}$$

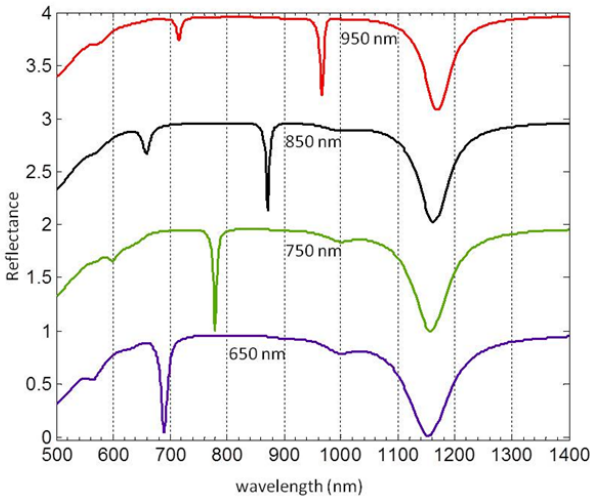

FIGURE 5.2 The reflection spectra at normal incidence for different array periods of Au square NP in a metal-insulator-metal structure, with the gap thichness of 25 nm, particle size of 200x200x50 nm^3.

Where λ_{SLR} is the wavelength at which the SLR occurs, and m and n are integers relating to the lattice constants (Pors and Bozhevolnyi, 2013a). By resolving SLR(1,1) and SLR(-1,1) into components, the components for two immediate particle sites destructively interfere due to symmetry and incident beam polarization. The only non-cancelling excitations are the (1,0) and (-1,0), which both occur in opposing directions but at the same wavelength. The dip at the left end of the SLR is the SPP associated with the diffracted incident beam. We observed that for closely packed nanobricks, an evanescent interaction between SLR and the gap mode exists as a dip shoulder to the immediate left of the gap mode. This shoulder reduces with larger inter-particle distance and has vanished for a period of 950 nm.

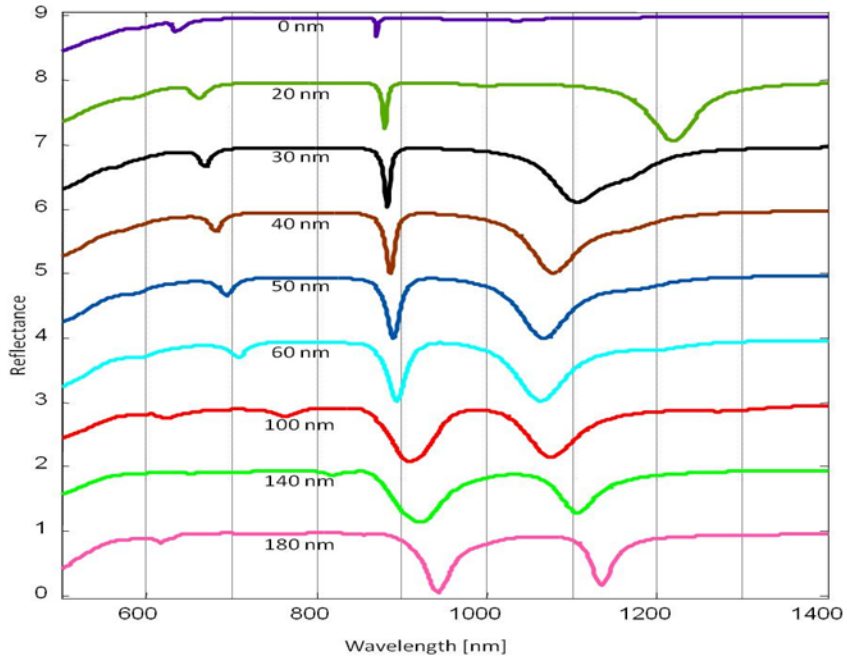

FIGURE 5.3 Reflection spectra for different gap thicknesses showing the gap mode tending to the blue light for thicknesses below 50 nm (a), and to the red light for thicker gaps (b).

To further gain insight into the origin of the gap mode, we calculate the reflection spectra for different gap thicknesses. To achieve this, we fix the period of the gold NP at 950 nm, while other parameters are kept as described above. We vary the dielectric thickness from 0-200 nm. fig. 5.3 demonstrates the evolution of SLR from ultrathin FWHM to broadband, pseudo-localized, and hybridized modes. For gap thicknesses greater than 50 nm, the spectral shape of both SLR and gap mode has become indistinguishable, indicating a strong interaction. The tuning of these resonances with respect to applications relies on the use case they are meant for. From sensor applications, where two distinct energies (far apart) are studied to systems of energy with close spectral proximity. For each reflection spectra shown in fig. 5.3, the resonance wavelength for the three dips is plotted against the gap thickness, and presented in fig. 5.4.

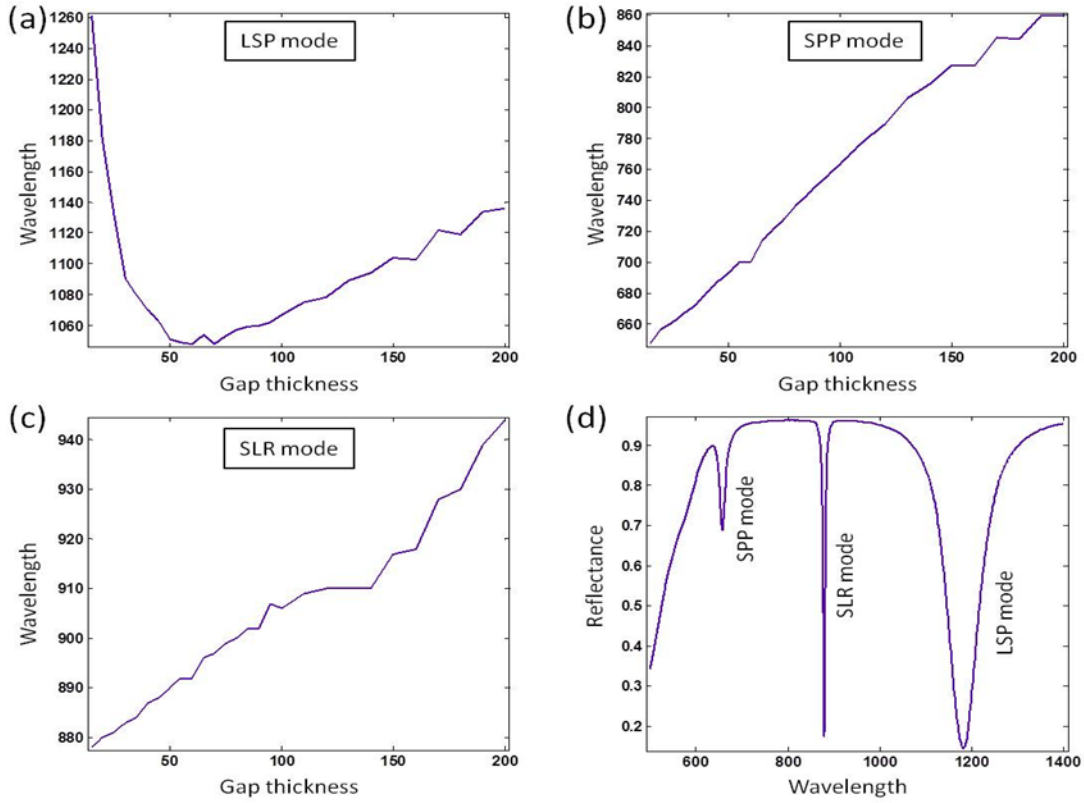

FIGURE 5.4 Resonance positions of different peaks in the reflection spectra of square gold nanoparticle arrays with grating period of 950 nm as a function of gap thickness for (a) LSP, (b) SPP, and (c) SLR plasmonic modes. (d) Reflection spectra obtained from gold square NP array with a period of 950 nm, showing positions of the plasmonic resonances.

Fig. 5.4 (a) shows that the resonance wavelength for gap thicknesses below 60 nm is blue-shifted while dielectric gap thicker than this tend to shift the gap mode to longer wavelengths. This is expected for a mode tightly localized inside the dielectric, indicating the concentration of energy in a sub-wavelength space. However, as the thickness gets wider, the evanescent interaction which leads to the excitation of gap mode suffers from radiation by coupling into higher diffraction order in the dielectric medium forming a hybrid photonic-plasmonic mode. This means that for a given period of the array, there is a cut-off gap thickness beyond which the gap mode cannot be supported. For the SLR and SPP resonances in fig. 5.3 c and b respectively, there is a linear dependence on the gap thickness. We observe that for the SPP resonance, there is a stronger dependence of the gap ($\Delta\lambda = 220$ nm) than the SLR which strictly is a function of array period ($\Delta\lambda = 140$ nm).
To investigate the coupling between the localized gap Plasmon and SLR, we tune the resonance wavelengths of the SLR mode by changing the array periodicity and fixing the gap thickness at 25 nm. In Fig. 5, the calculated resonance wavelengths of the three resonant modes are plotted as a function of the period. The solid lines drawn on both SLR and GSP (red and blue respectively) represent the free space wavelengths, considering that there is

no coupling between the two modes. However, a clear anticrossing feature occurs for a period of about 1090 nm. The anticrossing implies strong coupling between PSPs and SLRs with a splitting wavelength of $\sim$ 10 nm.

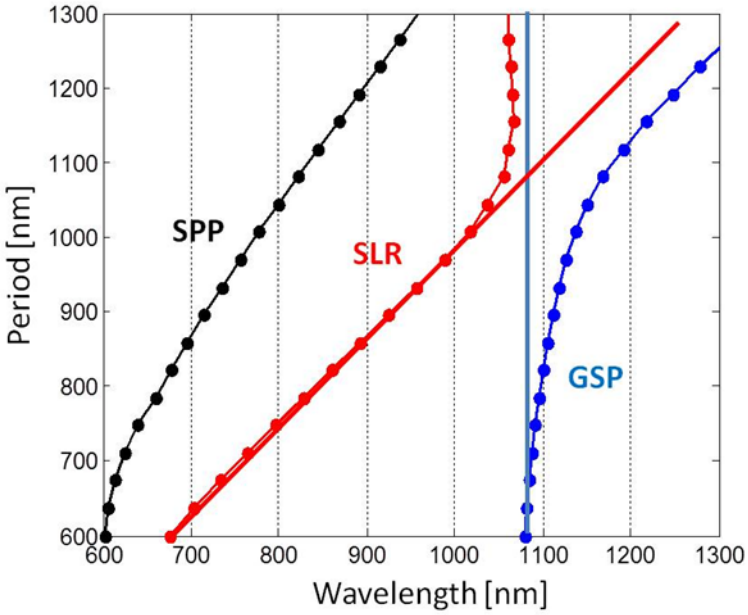

FIGURE 5.5 Resonance positions of different plasmonic modes as a function of array periods, showing the anticrossing effect between the localized gap plasmon and the lattice surface plasmon modes.

5.4 CONCLUSION

In summary, the chapter describes the reflection spectra of a metal-insulator-metal (MIM) structure containing Au square NP under normal incidence with x-polarized plane waves for different periods. The thickness of the metal film is infinitely thick, and the particle height and length are fixed at 50 nm and 200 nm, respectively, while the dielectric gap thickness is fixed at 25 nm. The reflection spectra show distinct resonances in three wavelength regions. The broad resonance centered at about 1150 nm is common across all the periods and associated with the excitation of a plasmonic mode localized inside the dielectric gap. The narrow deep resonance found at almost the grating period is the surface lattice resonance (SLR), which occurs due to the excitation of SPPs by diffraction orders of the incident beam and is governed by the Bragg formula.

The authors note that the SLR has components for two immediate particle sites that destructively interfere due to symmetry and incident beam polarization, and the only non-cancelling excitations are the (1,0) and (-1,0) which both occur in opposing directions but at the same wavelength. The dip at the left end of the SLR is the SPP associated with the diffracted incident beam.

Chapter 6

Band-pass integrated optical filters with hyperbolic metamaterials

6.1 Introduction

Optical bandpass filters are optical devices that selectively transmit a portion of the electromagnetic spectrum while rejecting all other wavelengths. One of the main applications of these devices stands for optical communications, where optical fiber technology requires the transmission of specific bandwidths at given wavelengths. For many years, different photonic waveguides compatible with optical fibers have been designed to properly filter light signals (Kogelnik, 1975; Suhara and Nishihara, 1986; Okamoto, 1999; Ma, Jen, and Dalton, 2002; Broquin, 2007; Sohler et al., 2008; Tong, 2013). Even with this development, several factors still hinder the practical use of these devices with nowadays technologies, which require of miniaturized functional photonic systems with more advanced and configurable filters with novel characteristics.

With the development of nanotechnology, new opportunities have opened up for the integration of artificially engineered subwavelength materials with enhanced properties not otherwise found in nature, so-called metamaterials (Zheludev and Kivshar, 2012; Urbas et al., 2016), with photonic waveguides. Among the different structures integrated to waveguides for signal filtering can be mentioned dielectric and plasmonic ring resonators (Rabus and Sada, 2020; Holmgaard et al., 2009), gratings (Pérez-Galacho et al., 2017; Quaranta et al., 2018), nanodisk (Matsko and Ilchenko, 2006; Lu et al., 2010; Khani, Danaie, and Rezaei, 2018) and asymmetric resonators (Tao et al., 2009; López-Rayón et al., 2022), nanostructured plasmonic waveguides (Lin and Huang, 2008; Neutens et al., 2012), waveguide cladding modulators (Tan, Ikeda, and Fainman, 2009; Yun et al., 2019; Yen et al., 2018; Yen et al., 2017) and photonic crystals (Jin et al., 2016; Mendez-Astudillo, Okayama, and Nakajima, 2018). In a previous work, we experimentally demonstrated that a gold nanoslab placed on top of an ion-exchanged glass waveguide serves as stop-band filter of light for a broad bandwidth at near infrared wavelengths (Tellez-Limon et al., 2020).

In recent years, a new kind of metamaterials had attracted the interest of research community due to their unusual anisotropic nature, the so-called hyperbolic metamaterials (HMM) (Poddubny et al., 2013; Shekhar, Atkinson, and Jacob, 2014; Ferrari et al., 2015). This growing interest is because isotropic materials have a closed isofrequency surface that limits the wavenumber of electromagnetic field propagating through these media. For HMM,

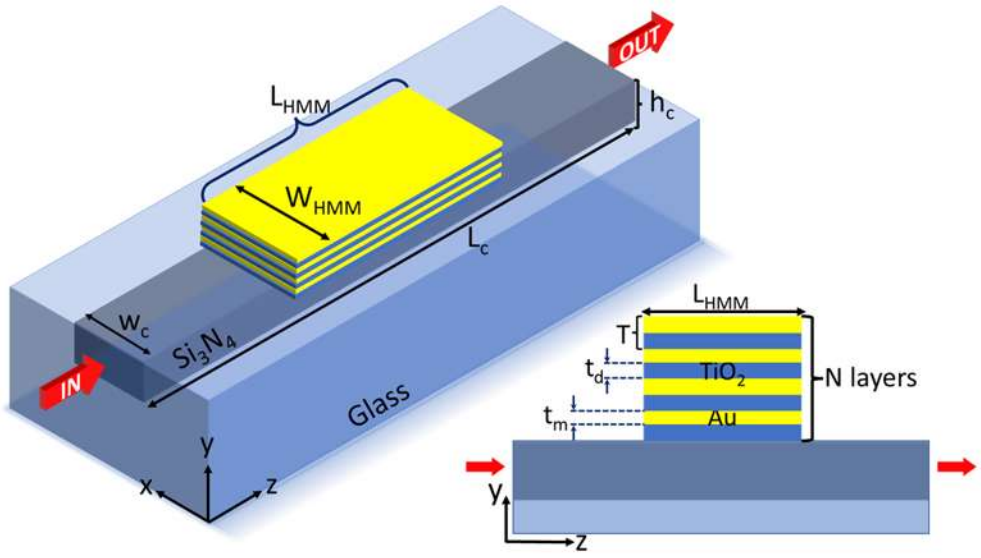

FIGURE 6.1 Schematic of the integrated device. Hyperbolic metamaterial consisting of a periodic array of $Au - TiO_2$ thin layers of thickness t_m and t_d, respectively, are placed on top of a Si_3N_4 waveguide ($w_c = 750$ nm, $h_c = 250$ nm) buried in a glass substrate. Photonic modes propagates through the waveguide along z direction from the input (IN) and transmission spectrum is measured at the output (OUT) face of the waveguide.

an extreme anisotropy is induced, leading to higher wavenumbers values in a non-closed hyperbolic isofrequency surface (Rytov, 1956; Drachev, Podolskiy, and Kildishev, 2013). One way to introduce this extreme anisotropy is by alternating dielectric and metallic thin layers (Kidwai, Zhukovsky, and Sipe, 2012; Ferrari et al., 2015; Tumkur et al., 2015). For this one-dimensional periodic structures, intrinsic resonant modes arise from coupling of photonic modes and SPP at the metal-dielectric interfaces, leading to hybrid photonic-plasmonic modes. If the wavelength and spectral bandwidth of these modes is too close, broad band resonances can take place (Kidwai, Zhukovsky, and Sipe, 2012; Zhukovsky et al., 2014). These broad resonances have been used for the design of bulk bandpass filters operating at telecommunications (Kalusniak, Orphal, and Sadofev, 2015), terahertz (THz) (Rizza et al., 2012) and near infrared (Naik et al., 2012) wavelengths. Integrated band-pass filters have also been proposed at THz frequencies by using a composite of two different-sized tapered HMM waveguide arrays, with each waveguide operating at wide but different absorption and transmission bands (Zhou et al., 2015).

However, the use of HMM for the development of band-pass filters integrated to optical waveguides operating at visible and near-infrared wavelengths has been barely explored. In this contribution, we numerically explore the design of an integrated band-pass filter by making use of metallic-dielectric multilayered HMM. The structure, as depicted in fig. 6.1, consist of a Si_3N_4 multimode waveguide on top of which is placed a finite periodic array of gold (Au) and titanium dioxide (TiO_2) thin layers. It is demonstrated that the transmission for the TM_0 mode is filtered at a central wavelength $\lambda = 760$ nm of bandwidth $\Delta\lambda_{FWHM} = 100$ nm with a transmittance above 40% of incident light, when the material

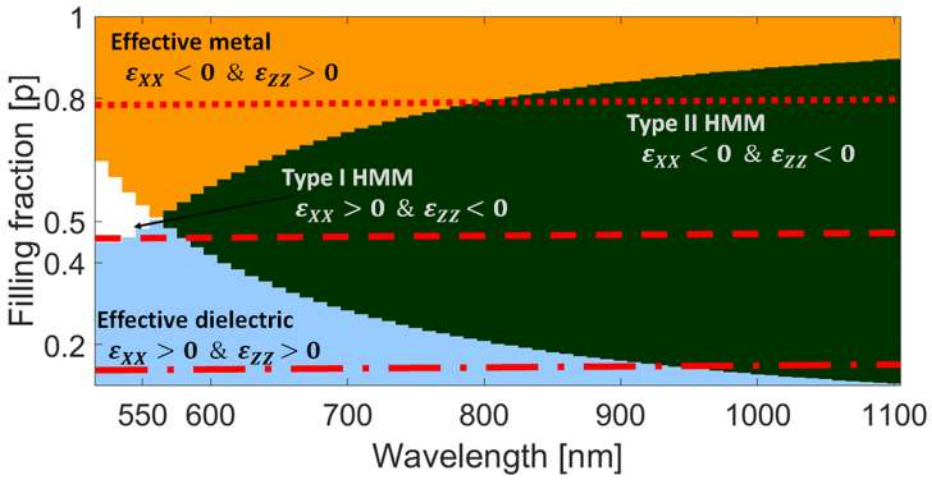

FIGURE 6.2 Phase diagram of the metamaterial composed by layers of Au/TiO_2 as function of the filling fraction and wavelength.

behaves as an effective metal or hyperbolic metamaterial type II (Ferrari et al., 2015), while for an effective dielectric metamaterial, the band-pass filtering can be tuned as a function of the period and number of layers. Due to the simplicity of the structure, the proposed devices open new perspectives for the development of size reduced integrated optical filters.

6.2 System Model and Design

6.2.1 Description of the integrated system

The device under analysis consist of a finite size HMM placed on top of a dielectric photonic waveguide, as depicted in fig. 6.1.

The waveguide consist of a rectangular silicon nitride (Si_3N_4) core of width $w_c = 750$ nm, height $h_c = 250$ nm and length $L_c = 2.0$ μm. This core of refractive index $n_c = 2.016$ was buried in a glass substrate of refractive index $n_{sub} = 1.5$. The superstrate was considered as air ($n_{sup} = 1.0$). This photonic waveguide supports the propagation of six modes ($TE_0, TM_0, TE_1, TM_1, TE_2$ and TM_2) along the z direction in the spectral range from 500 nm to 1523 nm. The cut-off wavelengths of these modes are $\lambda_{TE_0} = 1523nm$, $\lambda_{TM_0} = 1089nm$, $\lambda_{TE_1} = 901nm$, $\lambda_{TM_1} = 787nm$, $\lambda_{TE_2} = 654nm$, and $\lambda_{TM_2} = 611nm$, respectively.

The HMM has a width of $w_{HMM} = 1.0$ μm and length $L_{HMM} = 2.0$ μm, and it is constituted by a periodic array of N alternated thin layers of metal consisted dielectric (TiO_2) materials, of thickness t_m ad t_d, respectively. The period of the structure is $T = t_d + t_m$, as shown in inset of fig. 6.1. The HMM on top of the waveguide was centered with respect to the center of the core. The dielectric function of the gold was calculated from the Drude-Lorentz model as described in (Vial et al., 2005), while the refractive index of TiO_2 was taken from the refractive index database using Devore, 1951.

6.2.2 Effective medium theory

The effective medium theory describes a system considering the properties of its constituents. For a metamaterial composed by multilayers, if the layers are thinner with respect to the wavelength, it is possible to consider the electric field as spatially constant on that region and the effective electrical response of the whole system can be characterized by an effective permittivity. We propose an HMM made by a periodic dielectric-metallic multilayer system, which consists of alternating stacked thin films of titanium dioxide (TiO_2) and gold (Au). Each period T is constituted by a pair of dielectric-metallic thin films (measured in the z direction) (fig. 6.1). Considering the constituent materials, filling factor and using the effective medium theory for a multilayer system as calculated in (Rytov, 1956), obtained the effective permittivity phase diagram (fig. 6.2).
The effective permittivity phase diagram (fig. 6.2) classifies the effective medium according to the effective dielectric permittivity equation, as a function of the metal filling fraction and the wavelength, the behavior of the metamaterial depends on these two. The phase diagram was obtained using effective medium theory, in accordance with this, the effective dielectric function for transverse magnetic polarization is given by:

$$\epsilon_{xx} = \epsilon_{yy} = p\epsilon_m + (1-p)\epsilon_d, \tag{6.1}$$

$$\epsilon_{zz} = \left(\frac{p}{\epsilon_m} + \frac{1-p}{\epsilon_d}\right)^{-1}, \tag{6.2}$$

where p is the metal filling fraction (a portion of metal at each period). The metallic and dielectric layers have permittivities ϵ_m and ϵ_d, respectively. To calculate the phase diagram we used (6.1) and (6.2), varying the Au filling fraction from $p = 0.1$ to $p = 1$ and the wavelength from $\lambda = 500nm$ to $\lambda = 1100nm$. We show different regions depending on the signs ϵ_{xx} and ϵ_{zz}. TiO_2 permittivity was obtained from refractive index database Devore, 1951 and Au permittivity was calculated using Drude-Lorentz model and the parameters proposed by Barchiesi and Grosges (Barchiesi and Grosges, 2014).

6.2.3 Transfer matrix method

To compute the dispersion curves of the multilayered media, we used the transfer matrix method (Téllez-Limón and Salas-Montiel, 2021). These curves quantify the number of modes supported by the periodic structure as a function of the propagation constant at a given spectral range. The obtained results for a system of $N = 12$ layers (6 Au and 6 TiO_2 layers) with a filling fraction $p = 0.5$ and period $T = 80$ nm ($t_m = t_d = 40$ nm) are shown in fig. 6.3a. The green curves represent the modes, dotted curve represent the air light-line, and dashed curve correspond to glass substrate light-line. The map was plotted using logarithmic scale in order to facilitate its visualization.

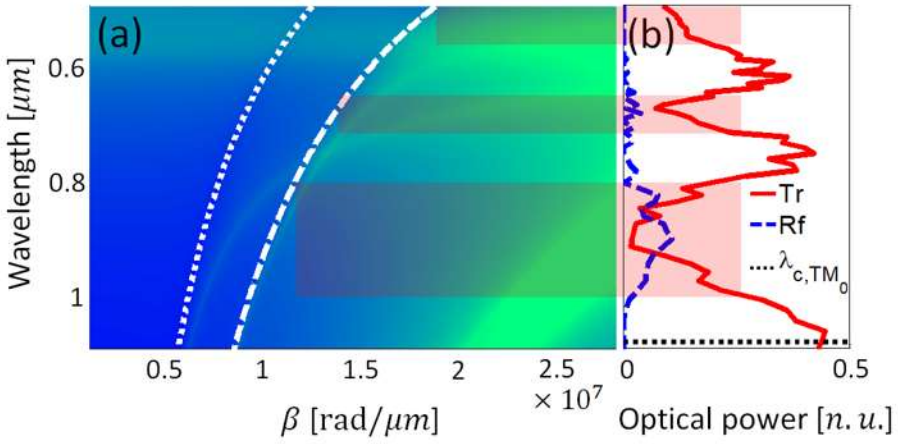

FIGURE 6.3 (a) Dispersion curves for a HMM of 6 Au and 6 TiO_2 layers with a filling fraction $p = 0.5$ and period $T = 80$ nm. Dotted and dashed curves represent air and glass light-lines, respectively. (b) Transmission (red) and reflection (blue dashed) spectra for an integrated system with a finite HMM ($N = 12$, $p = 0.5$, and $T = 80$ nm) integrated on top of a dielectric waveguide. Several modes in the dispersion curves are associated in main bands corresponding to broad-band minima in transmission spectrum (shaded regions).

6.2.4 Light propagation in 3D integrated device

To compute the transmission and reflection spectra of light at the output and input of the waveguide, we perfomed 3D simulations by means of the finite integration technique (Wittig, Schuhmann, and Weiland, 2006), using the commercial software CST Studio Suite 2020 (Dassault Systems, Vélizy-Villacoublay, France). To this purpose, first we computed the photonic modes supported by the dielectric waveguide and used the spatial distribution of their electromagnetic field and propagated them trough the waveguide. For the simulations, we used a computational window of width $w_x = 3.0$ μm, height $h_y = 2.4$ μm and length $L_z = 2.0$ μm, surrounded by perfectly matched layers. The transmission and reflection signals were measured defining port monitors at the input and end of the waveguide.
Fig. 6.3b shows the transmission (red line) and reflection (blue line) curves when the integrated device was excited with the fundamental TM_0 photonic mode. Two main broad minima bands are observed in the transmission spectrum, located at the spectral position of the broad modes supported by the HMM plotted in the dispersion curves.

6.3 Results

We firstly analyzed the dependence of the operation of the device as a function of light polarization. To this purpose, we propagated the fundamental TM_0 and TM_0 photonic modes through the waveguide. For TM_0 mode, the electric field is mainly oriented along

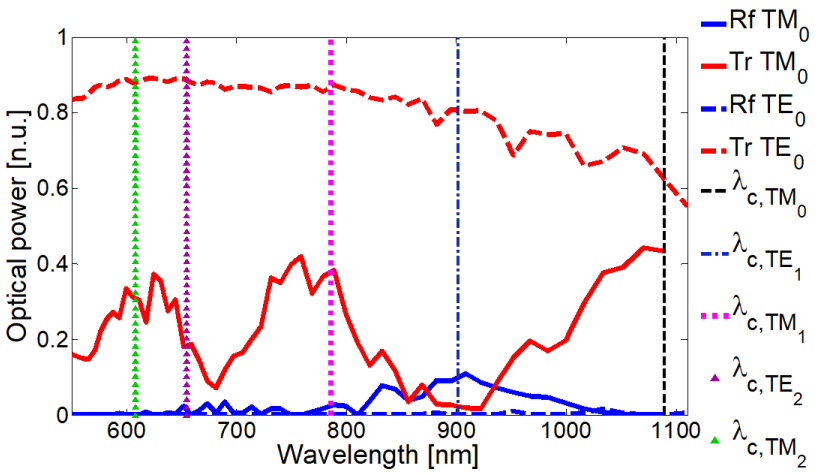

FIGURE 6.4 Polarization dependence of transmitted signal. For TM_0 mode (vertical polarization), the transmission spectrum exhibits two broad deeps due to the excitation of modes in the hyperbolic metamaterial. For TE_0 mode (horizontal polarization), no deeps are observed as no SPP are excited in the metamaterial.

the horizontal x direction, while for TE_0 the electric field is oriented along the vertical y direction (López-Rayón et al., 2022). For these simulations, we considered a system of $N = 8$ layers (4 Au layers and 4 TiO_2 layers) with a filling fraction $p = 0.5$ ($t_m = 40$ nm, $t_d = 40$ nm, period $T = 80$ nm), on top of the Si_3N_4 dielectric waveguide.
The results are plotted in fig. 6.4, where transmission and reflection curves for TM_0 mode (red and blue continuous, respectively) and for the TE_0 mode (red and blue dashed, respectively) are shown. Vertical lines correspond to the cut-off wavelengths for each mode supported by the waveguide in the spectral region from $550 - 1150$ nm: TM_0 mode has a cut-off wavelength $\lambda_{c,TM_0} = 1089$ nm (black dashed), TE_1 mode at $\lambda_{c,TE_1} = 901$ nm (blue dot-dashed), TM_1 mode at $\lambda_{c,TM_1} = 786$ nm (magenta dotted), TE_2 at $\lambda_{c,TE_2} = 655$ nm (purple triangles) and TM_2 at $\lambda_{c,TM_2} = 608$ nm (green triangles). We must remark that no mode conversion was observed, and scattering losses are around 10% of incident light: the signal reduction for TM_0 mode is mainly because of optical losses by absorption.
As observed in fig. 6.4, the transmission of TM_0 mode presents two main broad-band deeps centered around 680 nm ($\Delta\lambda_{FWHM} = 60$ nm) and at 900 nm ($\Delta\lambda_{FWHM} = 150$ nm). For TE_0 mode these broad deeps disappear.
As the transmission signal was modified only for TM_0 mode (vertical polarization), we studied the behavior of the transmission and reflection spectra in terms of the filling fraction, number of layers and period of the structure. We first considered a fixed period $T = 80$ nm for three filling fractions $p = [0.2, 0.5, 0.8]$ and three values for the number of layers $N = [8, 12, 16]$ (4, 6 and 8 pairs of $Au - TiO_2$ interfaces). The results are shown in fig. 6.5.
The principal observations from transmission (red curves) and reflection (blue curves) spectra of fig. 6.5 are as follows. For $N = 8$ (fig. 6.5a, b and c), the transmission spectrum for $p = 0.2$ exhibits minima at $\lambda = 638$ nm (guided light transmittance of 2%), $\lambda = 880$

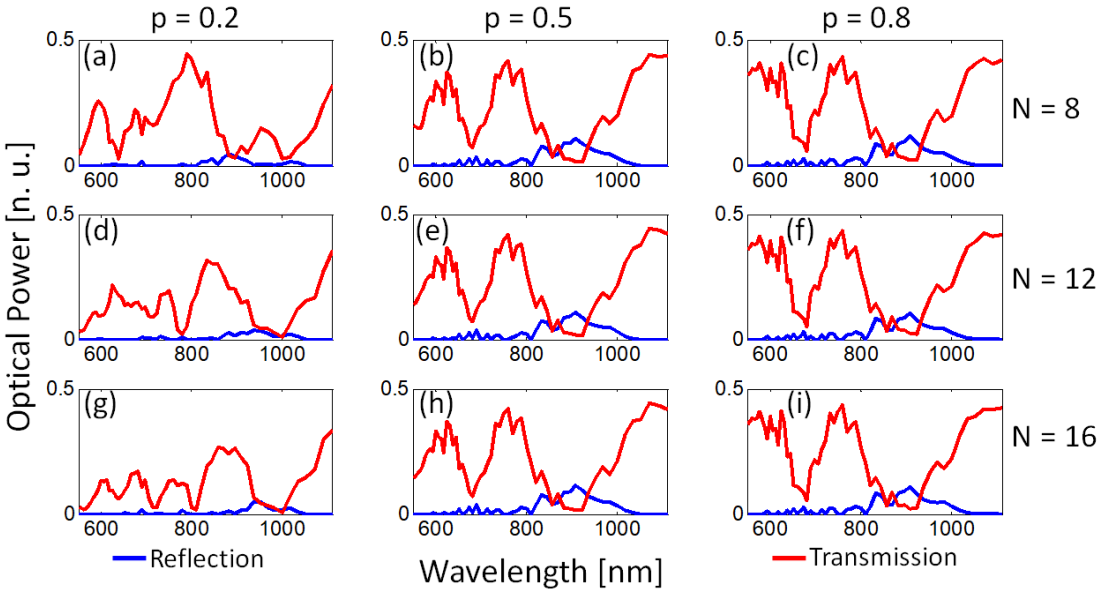

FIGURE 6.5 Dependence of the broad deeps as a function of the number of layers (N) and filling fraction (p). For $p = 0.2$, the number of deeps and their spectral position depends on the number of layers. For $p = 0.5, 0.8$, the broad deeps remain almost the same.

nm (transmittance of 4%) and $\lambda = 999$ nm (transmittance of 2%). For $p = 0.5$, two main broad-band deeps occur at 680 nm (transmittance of 7%, $\Delta\lambda_{FWHM} = 80$ nm) and at $\lambda = 908$ nm (transmittance of 1%, $\Delta\lambda_{FWHM} = 200$ nm). For $p = 0.8$, two main broad-band deeps also appear, centered at $\lambda = 680$ nm (transmittance of 5%, $\Delta\lambda_{FWHM} = 78$ nm) and at $\lambda = 908$ nm (transmittance of 2%, $\Delta\lambda_{FWHM} = 190$ nm). These two deeps generate a band-pass filter with a central wavelength around $\lambda = 760$ nm, $\Delta\lambda_{FWHM} = 100$ nm, and signal transmittance of 41%.

For $N = 12$ (fig. 6.5d, e and f), when $p = 0.2$ two local minima occur at $\lambda = 778$ nm (transmission of 2%, $\Delta\lambda_{FWHM} = 35$ nm) and at $\lambda = 999$ nm (0.9% transmittance, $\Delta\lambda_{FWHM} = 130$ nm) and a transparency band is observed centered at $\lambda = 845$ nm (30% transmittance, $\Delta\lambda_{FWHM} = 110$ nm). For $p = 0.5$ and $p = 0.8$, the transmission spectra are almost the same than for $N = 8$.

For $N = 16$ (fig. 6.5g, h and i), if $p = 0.2$, four minima are observed centered at $\lambda = 638$ nm (6% transmittance, $\Delta\lambda_{FWHM} = 20$ nm), $\lambda = 713$ nm (2% transmittance, $\Delta\lambda_{FWHM} = 40$ nm), $\lambda = 810$ nm (2% transmittance, $\Delta\lambda_{FWHM} = 30$ nm), and $\lambda = 999$ nm (0.6% transmittance, $\Delta\lambda_{FWHM} = 100$ nm). For $p = 0.5$ and $p = 0.8$, transmission spectra remain, once again, almost the same than for $N = 8$ and $N = 12$.

We then computed propagation of TM_0 mode considering a fixed number of layers $N = 8$ (4 pairs of $Au - TiO_2$ interfaces) for filling fractions $p = [0.2, 0.5, 0.8]$ and two periods of the layers $T = [50, 80]$ nm. The obtained transmission (red curves) and reflection (blue curves) spectra are shown in fig. 6.6.

For $T = 50$ nm (fig. 6.6a, b and c), when $p = 0.2$ two principal minima occur at $\lambda = 778$ nm (0.5% transmittance, $\Delta\lambda_{FWHM} = 57$ nm) and at $\lambda = 936$ nm (1% transmittance,

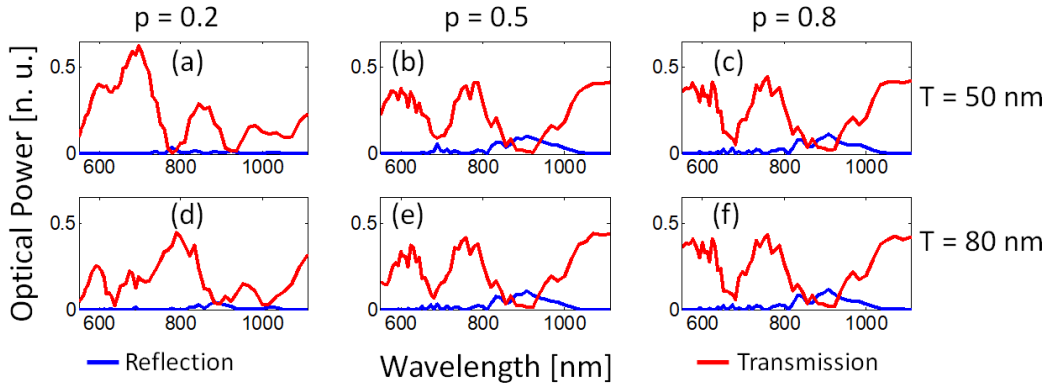

FIGURE 6.6 Dependence of broad-band deeps as a function of the period (T) and filling factor (p) for a fixed number of layers ($N = 8$ layers). For $p = 0.2$ (a and d), transmission (red) and reflection (blue) spectra are modified, while for $p = 0.5$ and $p = 0.8$, they remain almost unchanged.

$\Delta\lambda_{FWHM} = 47$ nm). For $p = 0.5$, two broad-band deeps appear centered at $\lambda = 689$ nm (9% transmittance, $\Delta\lambda_{FWHM} = 75$ nm) and at $\lambda = 920$ nm (0.9% transmittance, $\Delta\lambda_{FWHM} = 170$ nm). For $p = 0.8$, two deeps appear centered at $\lambda = 680$ nm (5% transmittance, $\Delta\lambda_{FWHM} = 65$ nm) and at 908 nm (2% transmittance, $\Delta\lambda_{FWHM} = 150$ nm). For $T = 80$ nm, the spectra and values are the same than in fig. 6.5a, b and c.

6.4 Discussion

The obtained results show that the transmission spectrum of a dielectric waveguide can be filtered by placing a hyperbolic metamaterial consisting of periodically structured metallic (Au)-dielectric (TiO_2) thin layers integrated on top of a dielectric (Si_3N_4) waveguide.
This optical integrated bandpass filter only operates if light is mainly polarized along the vertical y direction, situation that can be achieved by propagating the TM_0 mode of the photonic waveguide, as demonstrated in fig. 6.4. For this polarization, the electric field is symmetrically compatible for the excitation of SPP at the dielectric-metallic interfaces (Tellez-Limon et al., 2020).
As established by the effective medium theory (eqs. 6.1 and 6.2), the filling fraction of the multilayered system determines the behavior of the hyperbolic metamaterial (effective dielectric, effective metal of hyperbolic metamaterial type I or II), as shown in fig. 6.2. Hence, it is expected that the bands of modes supported by the hyperbolic metamaterial (see fig. 6.3, for instance) also depend on the number of layers (N). However, as demonstrated in fig. 6.5, the number of layers only modifies the spectral response (broad band shifting) of the integrated device when the metamaterial behaves as an effective dielectric material ($p = 0.2$). When the multilayered system behaves as hyperbolic media type II or as effective metal, the number of layers does not significantly modify the central wavelength of two principal broad-band resonances centered around $\lambda = 680$ nm and $\lambda = 908$ nm, with transmittance of 5% and 2%, respectively.

When the period of the multilayered structure was modified from $T = 80$ nm to $T = 50$ nm, it was also observed that for $p = 0.2$ different broad-band transmission minima arise and are spectrally shifted, while for $p = 0.5$ and $p = 0.8$ the two main broad-band deeps remain almost unchanged.
It is worth to mention that several small and narrow deeps also appear in transmission spectra. Most of them are due to plasmonic and hybrid photonic-plasmonic modes, which are hard to identify because the modes of the infinite multilayered system are too close to each other (see fig. 6.3a for instance). Also, it is possible that some of these small deeps arise from photonic modes, because the hyperbolic metamaterial placed on top of the dielectric waveguide is finite and standing waves can also take place. However, for $p = 0.5$ and $p = 0.8$, these perturbations are mounted in two main broad-band deeps.
These results open new perspectives for the design of simplistic integrated systems that can be easily fabricated to generate integrated optical band-pass filters by making use of 1D hyperbolic metamaterials. Without loose of generality, the combination of dielectric and metallic thin layers can be modified to tune the central wavelengths of the proposed integrated band-pass filters.

6.5 Conclusion

The chapter focuses on the development of optical bandpass filters and their applications in optical communications, specifically in the transmission of specific bandwidths at given wavelengths. This investigation focuses on the use of hyperbolic metamaterials (HMM) for the development of bandpass filters integrated into optical waveguides operating at visible and near-infrared wavelengths. We numerically explore the design of an integrated band-pass filter using a metallic-dielectric multilayered HMM, consisting of a Si3N4 multimode waveguide with a periodic array of gold and titanium dioxide thin layers. We filtered the transmission for the TM_0 mode at a central wavelength of 760 nm and bandwidth of 100 nm. We observed that the transmittance rises above 40% when the material behaves as an effective metal or hyperbolic metamaterial type II while for an effective dielectric metamaterial, the band-pass filtering can be tuned as a function of the period and number of layers. Due to the simplicity of the structure, the proposed devices open new perspectives for the development of size-reduced integrated optical filters. The study shows that a hyperbolic metamaterial consisting of periodically structured metallic and dielectric thin layers integrated on top of a dielectric waveguide can be used as an optical integrated bandpass filter. The filter operates for light that is mainly polarized along the vertical y direction, which can be achieved by propagating the TM_0 mode of the photonic waveguide. The filling fraction of the multilayered system determines the behavior of the hyperbolic metamaterial, and the number of layers only modifies the spectral response of the integrated device when the metamaterial behaves as an effective dielectric material. When the multilayered system behaves as hyperbolic media type II or as effective metal, the number of layers does not significantly modify the central wavelength of two principal broad-band resonances. Changing the period of the multilayered structure can also lead to different broad-band transmission minima and spectral shifting. The study also mentions that small

and narrow deeps appear in the transmission spectra, which are mainly due to plasmonic and hybrid photonic-plasmonic modes. These results provide new opportunities for the design of simplistic integrated systems that can be easily fabricated to generate integrated optical band-pass filters using 1D hyperbolic metamaterials.

Chapter 7

Two-photon imaging and field enhancement from random gold NP

7.1 Introduction

Localized surface plasmons have been generated in random metallic NP, and have demonstrated potential applications in different facets of technology. This has been the reason for the wide interest in the plasmonic properties of different random configurations in recent decades. Some interesting applications have been reported in recent years. For example, in the detection of small-sized molecules through Surface Enhanced Raman scattering (SERS), (Yang et al., 2017; Li; 2013; Yamazoe, 2014), refractive index sensing (Barrios, 2023), solar energy harvesting at different wavelengths, optical trapping (Tharwat, 2021), have become vibrant areas of research. This localization effect is due to in-plane multiple scattering by random surface nanostructure and interference in a random media. The effect is physically described by the theoretical Anderson electron localization. This implies that the localization spots are not automatic but on certain conditions. It has been proposed that light localization usually occurs when the free mean path is less or of the order of $\lambda/2\pi$, where λ is the wavelength of the incident light. There have been reports on the localization of SPP in random media from the literature. V. Coello et. al. have demonstrated strong localization in random gold nanostructures, using near-field optical images obtained from second harmonic (SH) far-field microscopy. Also reported, is a strongly enhanced SHG characterized by a broad angular (far-field) distribution observed with gold on glass film near the percolation threshold (P. Segovia, 2012). After this, a two-photon microscopy technique was used to perform high spatial resolution S-SHG imaging on granular gold structures. More recently, strong localization of SPP with engineered disordered nanograting was experimentally demonstrated. However, a detailed experimental study, showing the non-linearity nature SPP localization with wavelength, and polarization dependence is still not very well understood. In this section, we demonstrated using a two-photon luminescence technique, strong and well-localized SPP enhancement with gold random NP fabricated on a smooth gold thin film. It is shown that the enhancement depends principally on the wavelength and polarization of the incident light.

7.2 The Sample

The sample used in this work is prepared by depositing a layer of resist on a 55-nm-thick gold film, which has been evaporated onto a glass substrate. Another gold layer is spun on the resist and completed by employing a standard fabrication procedure process based on standard electron beam lithography and the lift-off technique. The resulting structure contains randomly placed 70-nm-high gold bumps in highly dense rectangular arrays. For these samples, the percolation threshold was near 70 Å with larger islands formed of their clusters. This means that the gold bumps are not yet considered a conducting layer. Fig. 7.2 shows the optical image obtained for the resulting structures under a 20X (a), and 100X (b) showing the highly dense gold bumps area.

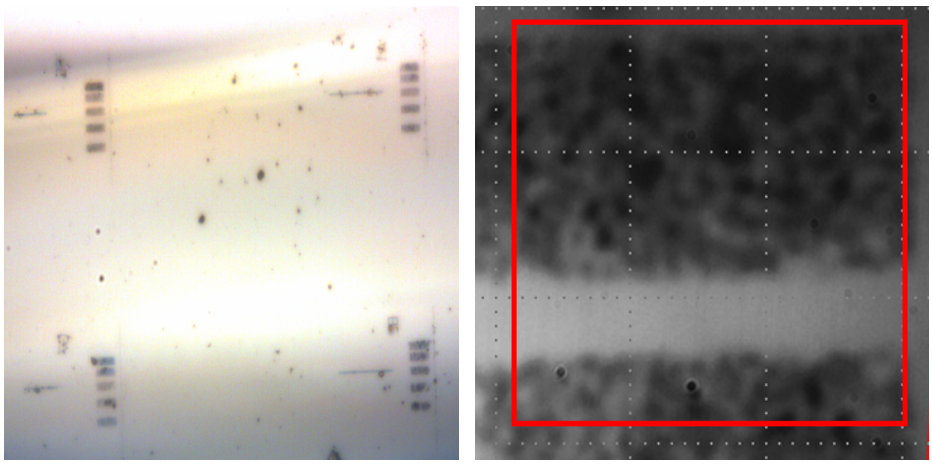

FIGURE 7.1 SEM images of random gold NP in rectangular arrays and magnification with an objective lens of 100X in a highly dense area.

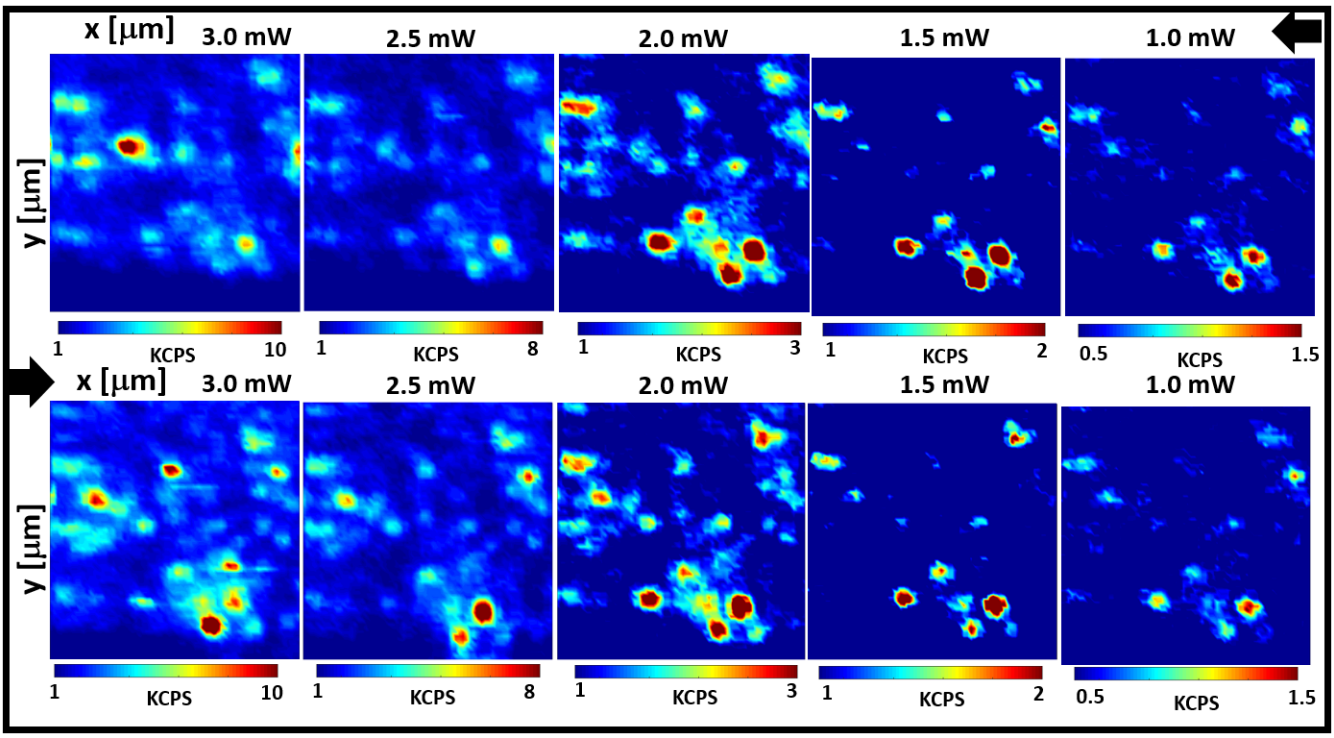

FIGURE 7.2 The quadratic power dependence of TPL signal on incident power and power hysteresis curve for incident power of 1 mW - 3 mW.

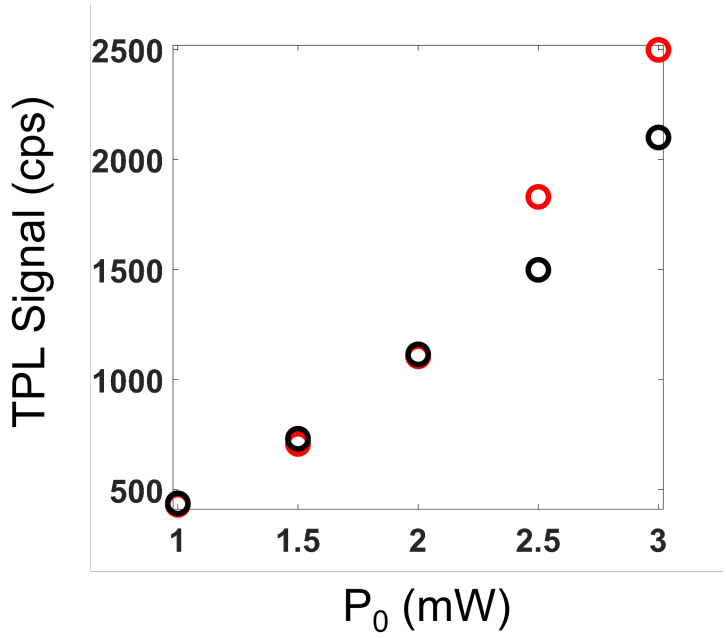

FIGURE 7.3 The quadratic power dependence of TPL signal on incident power and power hysteresis curve for incident power of 1 mW - 3 mW.

7.3 Results

7.3.1 Power Test

The random gold NP sample was investigated using the TPL experiments with a sample area of $20\mu mX20\mu m$ and a resolution of 130 nm in steps of 0.5 mW with varying input power and incident wavelength λ_0. As a first approach, we perform the power hysteresis experiment by changing input power from 1 mW to 3 mW and then returning from 3 mW to 1 mW. The choice of the power range is to avoid saturation in obtained results. This experiment tests the resistance of the sample to deformations by laser heating, and at what input power the nonlinear response is consistent. Fig. 7.2 shows the intensity map obtained from an area of $20 \times 20\ m\mu^2$ with gold bumps using an incident wavelength of $\lambda_0 = 790$ nm, polarization horizontal to the sample plane. The positions of the bright spots remain consistent for all incident power, which demonstrates the reproducibility of results within the chosen parameters. To estimate the signal count, we find the average over a specified area with consistent bright spots positions and present the graphical representation in fig. 7.3. However, we observe that for input power above 2 mW, the sample is already modified by the heating effect of the laser. For this reason, the average intensity over the chosen is different for both legs of the experiment.
The nonlinear property of the luminescence was studied by measuring the intensity of the luminescence as a function of the excitation power. The avalanche photodiode measures the luminescence while increasing the incident power from $1mW$ to $3mW$ and record it as a function of the particles' coordinates. It has been established that a quadratic dependence of the nonlinear intensity on the input power confirms the luminescence originated from a two-photon excitation process. Fig. 7.4 shows the dependence of the response on input power, obtained by illuminating the sample with incident power varying from 1 mW -3 mW. During post-processing, the average of the signal is calculated over a specified area within the NP, and after subtracting the dark counts from the average, the difference is called the TPL signal in this report. The power of 2.1 confirms the detected signal is from a two-photon absorption process while the intercept indicates the noise level (dark counts) indicates the nonlinear nature of the response, considering experimental and other sources of error.

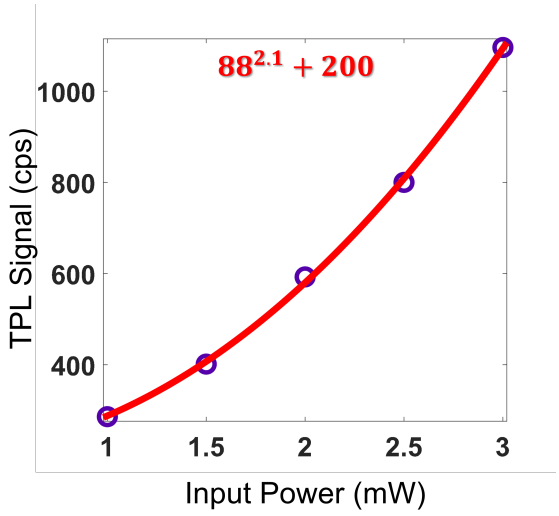

FIGURE 7.4 The quadratic power dependence of TPL signal on incident power and power hysteresis curve for incident power of 1 mW-3 mW.

7.3.2 Wavelength and Polarization Dependence

The wavelength dependence of the signal is demonstrated by an experiment with an input power of 2 mW and a wavelength range of 775-835 nm in steps of 15 nm, scanning over a sample area of 5.7 μ m $\times$ 5.7 μ m. The incident power, polarization, scanning resolution, and scanned area are all kept constant for this experiment. The images shown in fig. 7.5 show bright spots vanishing to zero while other bright spots emerge at longer wavelengths. This dependence can be attributed to the density of gold NP and the wavelength of the excited SPP. The interference pattern is expected to change at different incident wavelengths, and this is evident in the exchange of positions of the bright points (Coello, 2008b). Based on the theory of random walk, it has been determined that for enhancement to occur in random gold bump structures, the propagation length of SPP mediating the bright spots must be much longer than the scattering mean free path (Bozhevolnyi, 2002). The dark counts (background noise) is $\sim$ 11 since the experiment is realized in a well-controlled environment where other sources of illumination are reduced to a minimum. Among other bright spots, note that spots A, B, and C in fig. 7.5(a) are observed to gradually vanish for longer wavelengths while other bright spots emerge. The contrast of the images is adjusted individually to avoid oversaturation of the responses and be able to observe background details. Point D shows a diffuse-like hotspot, which can be attributed to weak multiple SPP scattering and interference in the surface plane. Another factor that may account for this feature is that the localization may also have occurred in islands of random gold bumps where the scattering mean free path is larger. In contrast to the diffuse hotspot in E, point D at $\lambda_0 = 820$ nm (d) demonstrates a hotspot reaching up to 30000 cps. This is equivalent to enhancement reaching up to $\sim$ 17 using the expression 7.1 (Hohenau et al., 2007).

$$\alpha = \sqrt{\frac{S_{NP}\langle P_{film}\rangle^2 A_{film}}{S_{film}\langle P_{NP}\rangle^2 A_{NP}}}, \tag{7.1}$$

where S_{NP} and S_{film} are TPL signals obtained from a sample area with NP and gold smooth surface respectively. $\langle P\rangle$ is the average incident power, and A is the area over which the signals are measured.

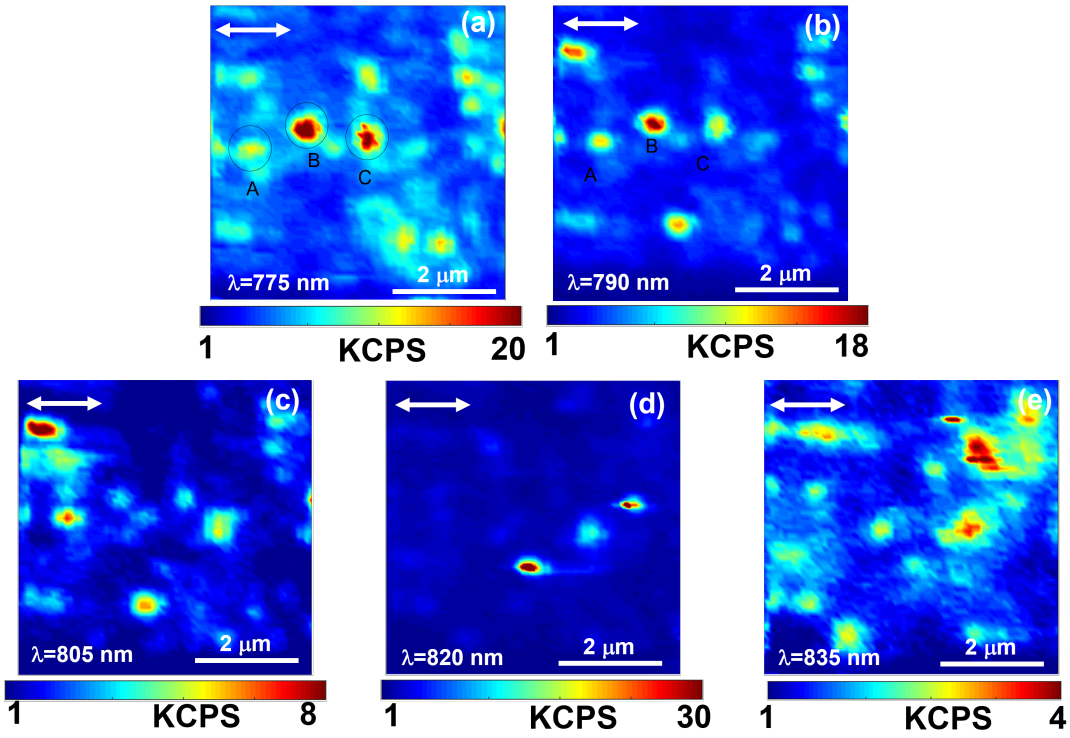

FIGURE 7.5 TPL images of the same area (5.7 $m\mu$x5.7 $m\mu$) with the same high density of gold NP in random array structure for five different wavelengths, varying from 775 nm to 835 nm. The direction of incident polarization is indicated by the arrows.

Fig. 7.6 shows polarization dependence of nonlinear response obtained from a (20 $m\mu$x20$m\mu$) densely-packed gold bumps area. The positions of bright spots are obviously different for both polarizations. We observe that there are more bright spots for vertical polarization, with a maximum signal count of 14000. This can be attributed to the geometrical orientations of the gold bumps in the x-y plane. The vertical polarization supports more efficient excitation of SPP, using the gold bumps as a diffraction coupler. It is worth mentioning that after different complete series of wavelength and polarization measurements, identical responses with the same hotspot positions and average intensity values were observed. This confirms that the pronounced differences in the exchange of bright spot positions and intensity distributions are truly because of the change in wavelength and polarization.

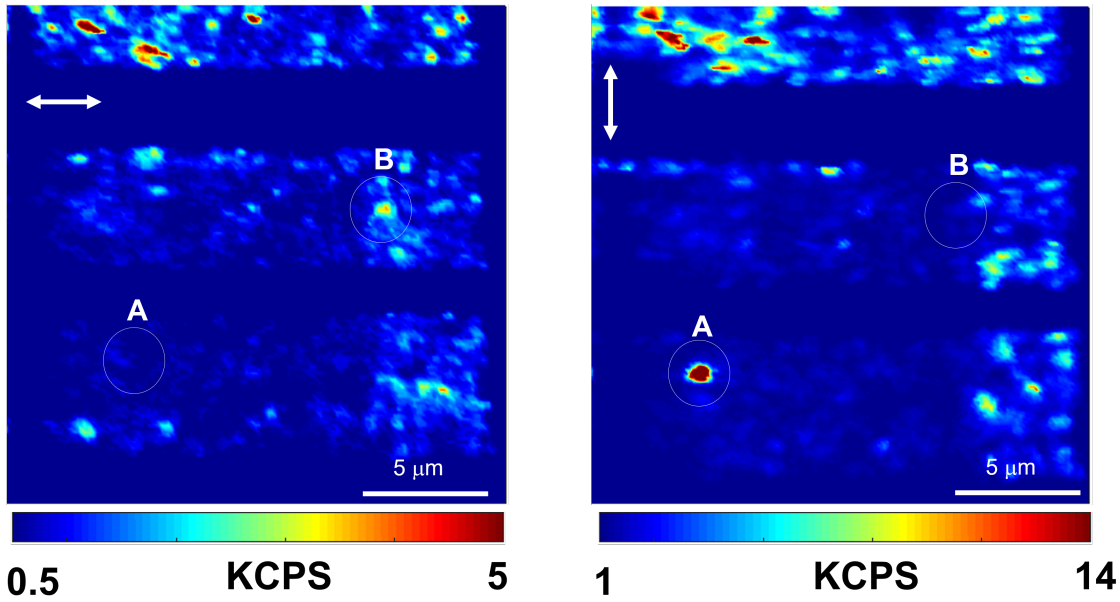

FIGURE 7.6 TPL images of the same area (5.7 $m\mu$ X 5.7 $m\mu$) with the same high density of gold NP in random array structure for five different wavelengths, varying from 775 nm to 835 nm. The direction of incident polarization is indicated by the arrows.

7.4 Conclusion

The results of the TPL experiments on a random sample of gold NP are presented in this chapter. The intensity map obtained from an area of 20 × 20 μm^2 with gold bumps using an incident wavelength of λ_0 = 790 nm, with polarization horizontal to the sample plane, shows that the positions of the bright spots remain consistent for all incident powers, indicating the reproducibility of results within the chosen parameters. The nonlinear property of the luminescence was studied by measuring the intensity of the luminescence as a function of the excitation power. A quadratic dependence of the nonlinear intensity on the input power confirms that the luminescence originates from a two-photon excitation process. The experiment shows that hotspot positions and intensity distributions change with wavelength and polarization, with more bright spots observed for vertical polarization, indicating more efficient excitation of SPP using the gold bumps as a diffraction coupler.

Chapter 8

Two-photon imaging of field enhancement from square array of gold NPs

8.1 Introduction

The quest for light control below diffraction limit is vastly dominating the study of microscopy in recent decades because they have potential applications in different fields. The two-photon luminescence (TPL) microscopy is a nonlinear microscopy that uses two-photon excitation and absorption in molecules that has recently been used to investigate the optical properties of molecules and surfaces. In this process, a molecule absorbs two simultaneous quanta of light of either different or the same energies to emit a photon at a shorter wavelength. To induce TPL in natural materials, a highly energetic electric field is required; high enough to break the linear correlation between the incident electric field and the polarizability response in the material medium (Boyd, 2007). This provokes the emission intensity to quadratically depend on the incident power which implies a high signal-to-noise ratio that makes TPL-based sensors more efficient than their conventional counterparts (G. E. Johnstone, 2019). This emission, in a collection of gold nanorods (GNR) can form strong localization of light in a nanometer-volume of space and has been applied in optical biosensors, used in detecting pathogenic microorganism (A. A. Bergwerff, 2006; J. Homola, 2009; Y. Wang, 2012; K. Whang, 2018), and biomarker detectors used in non-invasive early cancer detection (N. Bellassai, 2019; J. Duffy, 2018). We demonstrated in an earlier work that the enhancement can assist waveguiding property in a random assembly of NPs (Pisano et al., 2016), as well as surface enhanced Raman Scattering (Novikov et al., 2016).

Due to the Abbe diffraction limit imposed by optical devices, laboratory samples in nanometer sizes appear unclear under traditional microscopes. By employing plasmon-assisted TPL, where images are formed at plasmon resonance wavelengths, overcoming this limitation as has been proposed and demonstrated in the imaging of lipid drops (J. Yin, 2019), preneoplastic oral mucosa (S. Motamedi, 2011), and groups of nanostrip antenna (Novikov et al., 2009). Aside from quantifying enhancement based on the rectangular structure of gold nano bars, a detail on how the enhancement is affected by periodicity is yet to be presented experimentally.

Most studies on two-photon enhanced luminescence focus on the spectral position of plasmon resonances, purposely for sensor-based applications while for the enhancement and directionality of such emissions, only little is known. Aside from using asymmetric structures and incident angle to control the direction of SPP, the direction of excitation can also be exploited by incident light polarization (J. Lin, 2013; L. Huang, 2013; T. Qing, 2020). The numerical calculations by (S.J. Erik, 1999) for gold tips show an enhancement factor of up to 1000, while theoretical studies by Shalaev et al. predicted even stronger enhancement of optical fields near semi-continuous metal film with random clusters of metallic particles (Shalaev, 1996; J. Beermann, 2006b; Beermann et al., 2008). As far as controlling the directionality of TPL excitation, Zenin et. al. have used 2-D periodic lattice of metal particles since they posses translational symmetry, hence, can support plasmon waves travelling in the direction ortogonal to the incident light polarization (V.A. Zenin, 2015; Novikov et al., 2009; Beermann and Bozhevolnyi, 2006). However, because of reproducibility, exploring TPL to image surfaces with regular sub-wavelength structures is more practical in contrast to random clusters of NPs, and needs to be emphasized.
In this contribution, we use a two-photon excitation laser-scanning microscope to study the local field enhancement and TPL-mediated imaging of 2D periodic lattice of gold square NPs. It is well established that the surface plasmon modes in an array of periodic metal particles can be modified by varying the periodicity of the array as well as the particle sizes. Hence, we measured the two-photon luminescence of gold NPs by fixing the interparticle distance while varying the NP size. TPL imaging is characterized as a function of excitation wavelengths and polarization. We observe that the enhancement in these periodic structures is strongly dependent on the incident wavelength and array period, while the excitation direction is principally controlled by the incident light polarization. For each of the designed structures, the enhancement factor is evaluated.

8.2 Materials and Methods

The sample used in this study consists of three 100 μ mx100 μ m arrays with gold NPs of different sizes and particle-particle distances. The sample is fabricated by using standard electron-beam lithography (EBL) and lift-off patterning. A 100-nm-thick gold film is deposited on a silicon wafer, then a layer of polymethyl methacrylate (PMMA) is spin-coated on the gold deposit, which acts as a positive resist. After patterning the PMMA using the EBL module, the gold is deposited onto the composite structure. Finally, a solvent is used to dissolve the resist and complete the lift-off. The arrays are kept at the same area size while the particle sizes are varied to produce structures with a constant period of 730 nm. The performance of the fabricated components is characterized by TPL microscopy with a tunable (760 nm - 840 nm) Ti:Saphire mode-locked pulsed laser as a source. At a repetition rate of 80 Mhz and average power of 300 mW, the laser produces photons with a pulse of $\approx$ 200 fs. The TPL experimental setup as shown in fig. 4.3 operates in reflection geometry. At the exit of the beam from the laser cavity, the polarization and the input power are controlled by the combination of a polarizer (P) and a half-wave plate (HWP). After passing through a beam expander (used to control the beam spot size and shape), the laser beam is

focused on the sample at normal incidence with a Nikon Plan X100 objective. The reflected signals with both first harmonic (linear response) and TPL (nonlinear signals) are collected with the same objective and separated by a long-pass dichroic mirror that reflects TPL signals ($\lambda < 638$ nm), and transmitting linear signal ($\lambda > 638$ nm). The TPL response is collected by an Avalanche Photo-detector (APD) connected to a photon counter, leading to a higher signal-to-noise ratio. The average dark counts with this setup is 30 cps. Both TPL and FH signals are simultaneously recorded as a function of the X-Y scanning coordinates of a high-precision controlled piezo-electric stage upon which the sample is mounted. The setup is connected to a workstation which is used to reconstruct the FH and TPL images, using the commercial computer program LabView.

8.3 Results

Square gold NPs with a height of 100 nm positioned periodically in a square array have been studied experimentally using the setup described in chapter 4. Three different NP sizes are studied. The dimensions are 330, 350, and 370 nm, leading to interparticle distances of 400, 380, and 360 nm respectively. The choice of this particle size stems from deformations due to laser heating as reported by Beermann (Beermann and Bozhevolnyi, 2006; Beermann and Bozhevolnyi, 2004). Hence, with a 100x100x330 nm^3 volume size, the sample will be more resistant to modifications by laser heating. To functionalize the NP arrays, two-photon-induced luminescence from the sample was verified using an incident wavelength of 790 nm and measuring the dependence of the TPL signal intensity on excitation power. The input power is varied from 0.5 mW to 4 mW and the dependence is confirmed by the logarithmic graph with a slope value of 2 (fig. 8.1 inset), indicating that the excitation emanates from a two-photon process fig. 8.1. For the rest of this paper, the incident power will be 2 mW since for this power, TPL signal is stable for repeated scans over the same sample area.

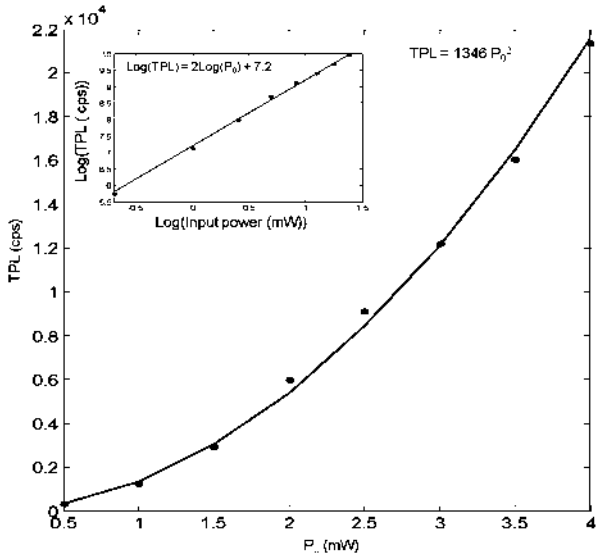

FIGURE 8.1 Power dependence measurement on a square array of gold NPs with a period of 730 nm. The input power is varied from 0.5 mW – 4 mW in steps of 0.5 mW. The solid line is a linear fit with a slope value of 2. For the rest of this paper, the incident power will be 2 mW since for this power, TPL signal is stable for repeated scans over the same area.

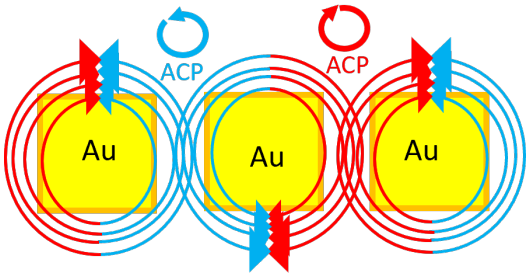

FIGURE 8.2 A schematic representation of polarization decomposition into clockwise and anti-clockwise circular polarization.

Fig. 8.3 and 8.4 show images of TPL and FH measurements obtained from scanning $6.7\mu mX6.7\mu m$ area of an array with a particle-particle distance of 400 nm and a square dimension of 330 nm. Both horizontal and circular polarizations are presented and are indicated by the corresponding images. For both polarizations, the NP sites appear in the FH images as dark spots since light is scattered by the gold patches, while reflection from smooth gold substrate is shown as bright areas because of its high reflectivity. In contrast to the FH images, TPL signals from gold substrate is practically zero the for the input power of 2 mW, and the particle sites appear as bright spots. However, the TPL from the substrate increases as the incident wavelength increases, hence, the contrast of the images is adjusted for clarity. For the horizontal polarization (fig. 8.3), the particles act as diffraction coupler

for the incident light, coupling light with gold plasmons to excite surface plasmon propagating in two symmetric directions perpendicular to the FH k-vector. With this in mind, we can identify the bright stripes as [0,1] and [0,-1] resonant SPP modes. Images obtained for vertical polarization follow the same pattern but for [1,0] and [-1,0] resonant SPP, and are so not included here. The images show variations in hotspot position and intensity with respect to change of FH incident wavelengths. The most pronounced image (λ = 820 nm) has the most number of hotspots with TPL localized signal count reaching as high as 40000 cps and well-defined stripes.

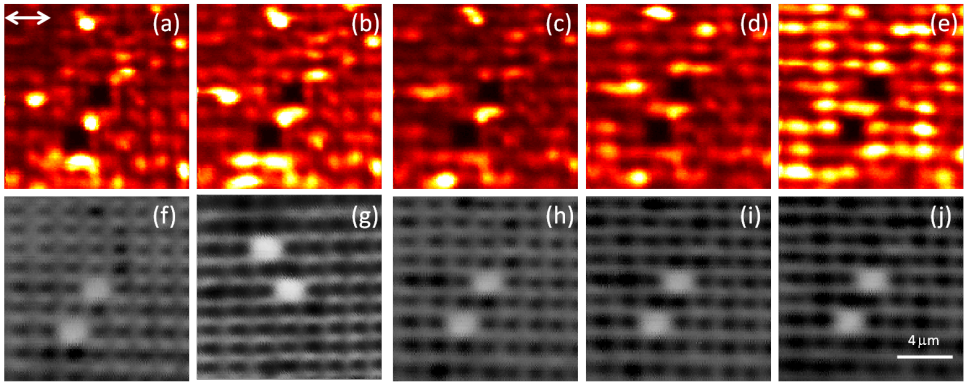

FIGURE 8.3 TPL images of 6.7x6.7 μm^2 gold square NP in a square array with a particle-particle distance of 400 nm with incident wavelength 770-810 nm in a step of 10 nm (a-e). FH images corresponding to the same area with the same incident wavelength as in (a). The incident power is 2 mW and polarization is indicated by the arrow. The maximum TPL (a-e) signal is 25000 cps, and the maximum for FH images (f-j) is 0.96.

Theoretically, circularly polarized light that impinges on an array of particles can be decomposed into clockwise circularly polarized (CCP) and anticlockwise circularly polarized (ACP) beams (T. Qing, 2020). When the interparticle distance is $d \neq \lambda_{SPP}/4$, there is a destructive interference between the ACP emerging from one NP and that of its nearest left-hand side scatterer. If we consider the same process as applied to the right-hand side NP for CCP as demonstrated in fig. 8.4, it is only expected to have destructive interference on both sides of the gold patch. For an x-polarized light, no SPP excitation occur in the direction orthogonal to the incident k-vector, the bright spots then take a more circle-like shape around the NPs.

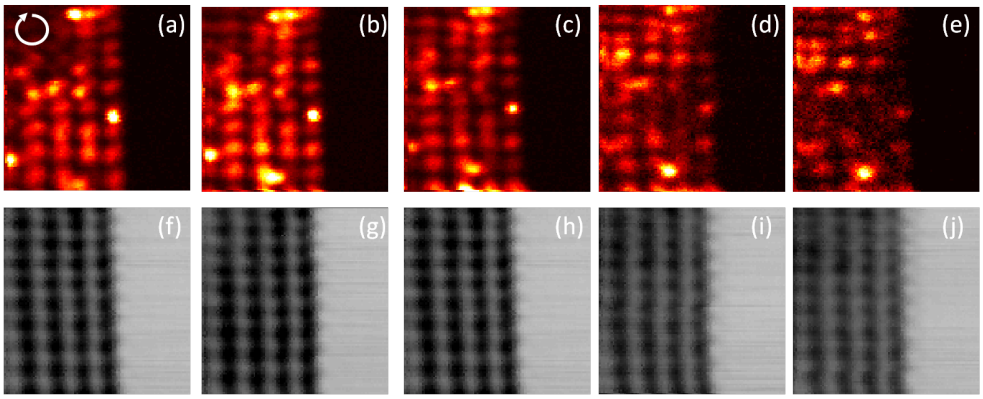

FIGURE 8.4 6.7 X 6.7 μm^2 TPL images of gold square NP in a square array of period 790 nm with incident wavelength 770-810 nm in a step of 10 nm (a-e) . FH images corresponding to the same area with incident wavelengths of 770-810 in step of 10 nm. The incident power is 2 mW and polarization is indicated by the arrow.

As the next step, we experimentally estimate the intensity enhancement in the array of gold particles. This can be objectively achieved by taking into consideration the area and the incident power that produces the TPL signal. The enhancement factor for the TPL from gold NPs compared to the signal obtained from smooth gold substrate has been previously calculated using expression in equ. 7.1.

To test whether the observed phenomenon is spatially homogeneous and if so, to estimate the magnitude of the peak enhancement factor, we perform a scan over an area of $4X4\mu m^2$ with NP and the same area size without gold nanopatches, using the same input power for horizontally polarized light while changing the incident wavelength from 760-840 nm in steps of 10 nm. Three different NP lengths are selected (370, 350, and 330 nm), with a fixed interparticle distance of 400 nm. The average enhancement factor in fig. 8.5 shows two distinct peaks around $\lambda = 780$ nm and $\lambda = 810$ nm for a structure with particle length of 370 nm. The average intensity enhancement peaks increase with an increasing gap between the patches as the wavelength shifts to red. This increase in enhancement can probably be related to two major phenomena; (i) Larger filling of the Gaussian focus spot as the gap increases, and (ii) increased coupling efficiency as back-scattering reduces for smaller particles.The maximum enhancement occurs at 760 nm for all particle length, but unfortunately, this is the minimum wavelength achievable to operate the laser in pulsed mode. We obtain enhancement factor reaching 12000 for gap of 400 nm.

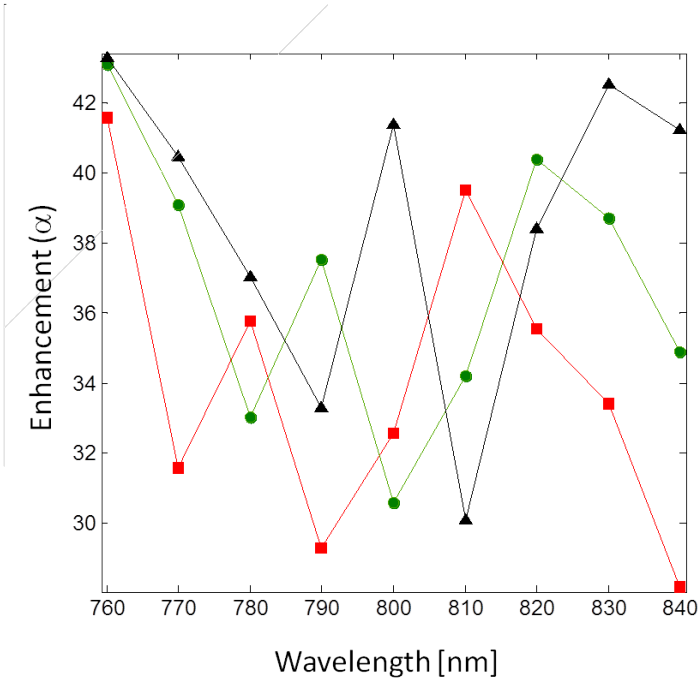

FIGURE 8.5 6.7 X 6.7 μm^2 TPL images of gold square NP in a square array of period 790 nm with incident wavelength 770-810 nm in a step of 10 nm (a-e) . FH images corresponding to the same area with incident wavelengths of 770- nm in step of 10 nm. The incident power is 2 mW and polarization is indicated by the arrow.

8.4 Conclusions

In this experiment, square gold NPs with a height of 100 nm positioned periodically in a square array were studied. The NPs had three different sizes of 330, 350, and 370 nm, which resulted in interparticle distances of 400, 380, and 360 nm respectively. The sample was functionalized using two-photon-induced luminescence, and the dependence of TPL signal intensity on excitation power was measured. The incident power was set to 2 mW since at this power, TPL signal was stable for repeated scans over the same sample area.

The TPL and FH images were obtained from scanning a 6.7μmX6.7μm area of an array with a particle-particle distance of 400 nm and a square dimension of 330 nm. The horizontal and circular polarizations were presented and identified by the corresponding images. The NP sites appeared in the FH images as dark spots, while reflection from smooth gold substrate was shown as bright areas because of its high reflectivity. In contrast to the FH images, TPL signals from the gold substrate were practically zero for the input power of 2 mW, and the particle sites appeared as bright spots. The TPL images showed variations in hotspot position and intensity with respect to the change of FH incident wavelengths.

Circularly polarized light impinging on an array of particles can be decomposed into clockwise circularly polarized (CCP) and anticlockwise circularly polarized (ACP) beams.

When the interparticle distance is not equal to $\frac{\lambda_{SPP}}{4}$, there is destructive interference between the ACP emerging from one NP and that of its nearest left-hand side scatterer. For an x-polarized light, no SPP excitation occurs in the direction orthogonal to the incident k-vector, and the bright spots take a more circle-like shape around the NPs.

The intensity enhancement in the array of gold particles can be estimated by taking into consideration the area and the incident power that produces the TPL signal.

Chapter 9

CONCLUSION and OUTLOOK

9.1 Conclusion

This Ph.D. research project aimed to elucidate into the design, analysis, and optimization of plasmonic structures to enhance their characteristics. To achieve this, various aspects of these structures were thoroughly investigated using advanced numerical methods such as Finite-Difference Time-Domain (FDTD) and Finite Element Method (FEM). The research progressed by focusing on the design of arrays of gold nanoparticles, carefully considering their precise periodicity and particle dimensions. Additionally, a dielectric layer was introduced between arrays of gold bumps and a gold thin film, forming a metal-insulator-metal (MIM) structure. This configuration facilitated the exploration of reflection spectra, periodicity dependence, and gap thickness dependence of plasmonic resonances. An in-depth analysis was conducted to understand the simultaneous occurrence and interaction of plasmonic resonances originating from different channels, thus providing valuable insights into their interplay and potential applications. Through simulations, multiple plasmonic resonances within the near-infrared domain were discovered, showcasing their tunability by varying the array period. A significant finding was the coupling between localized surface plasmon (LSP) resonances and surface plasmon polariton (SPP) resonances, resulting in the generation of the gap-surface plasmon (GSP) effect, which exhibited a blue shift with increasing gap thickness. Furthermore, the reflectance spectra exhibited distinctive dips with nearly zero reflectivity values, indicating the presence of resonant modes within the system. Remarkably, the dips with the narrowest bandwidth displayed a linear dispersion with the lattice period, aligning precisely with the period of the grid.

The analysis of the reflection spectra, combined with the examination of the near-field optical distribution around the nanoblocks, provided crucial insights into the optical response and the intricate hybridization effects of the metal-insulator-metal (MIM) structure. Moreover, the calculated near-field images confirmed the redistribution of the electromagnetic field with varying gap sizes, illustrating the coupling of scattered light to surface plasmon polaritons (SPPs) between neighboring nanoblocks. These findings significantly contributed to the fundamental understanding of plasmonic resonances in periodic nanoparticle arrays and offered valuable insights for the design and optimization of nanophotonic devices, allowing for the tailoring of their optical properties.

Furthermore, the research project delved into exploring an intricate structure that involved cascaded metal-insulator-metal (MIM) layers, resulting in the formation of a hyperbolic metamaterial. The device consisted of a finite-sized HMM (Hyperbolic Metamaterial) placed on top of a dielectric photonic waveguide. The waveguide was made of a rectangular silicon nitride (Si3N4) core buried in a glass substrate, with an air superstrate. The dispersion curves and spatial distribution of the electric field for different modes supported by the waveguide were determined. The HMM was composed of an infinite periodic array of alternating thin layers of gold (Au) and titanium dioxide (TiO2). The effective medium theory was employed to characterize the electrical response of the HMM, and a phase diagram was obtained, showing the regions with positive and negative effective permittivity components. The HMM exhibited extreme anisotropy and hyperbolic dispersion curves when the effective permittivity components had opposite signs. The dispersion curves of the multilayered HMM were calculated using the transfer matrix method. The number of modes supported by the structure was quantified as a function of the propagation constant in a given spectral range. The obtained results showed the presence of broad minima in the transmission spectrum, corresponding to the excitation of modes in the HMM. By performing 3D simulations using the finite integration technique, the transmission and reflection spectra of the integrated system were computed. The results demonstrated that the broad minima in the transmission spectrum were primarily observed for the TM0 mode (vertical polarization), while the TE0 mode (horizontal polarization) did not exhibit deeps due to the excitation of surface plasmon polaritons (SPPs) in the HMM. The dependence of the transmission spectrum on the filling fraction, the number of layers, and the period of the HMM structure was also investigated. It was found that the broad deeps remained almost the same for filling fractions of 0.5 and 0.8, and for different numbers of layers (8, 12, and 16). Additionally, the transmission spectra exhibited local minima and transparency bands at specific wavelengths for different combinations of filling fraction and number of layers. Overall, the analysis of the device's performance revealed the ability to control and manipulate light propagation through the integration of the HMM with the dielectric waveguide. The findings provided insights into the design and optimization of integrated photonic devices based on metamaterials, offering potential applications in areas such as sensing, imaging, and optical communication.

In addition to the numerical investigations, the research project aimed to validate the findings and assess the practical feasibility of the designed plasmonic structures through experimental characterization. It is worth to remark the impact of the challenging circumstances imposed by the COVID-19 pandemic, which significantly limited access to laboratories and resources. Nevertheless, despite these circumstances, significant efforts were made to adapt and continue with the experimental investigations. The experimental characterization involved the thorough study of the linear and nonlinear responses of the fabricated plasmonic structures. Special attention was given to the evaluation of arrays of gold nanoparticles, and two-photon luminescence measurements were conducted to precisely assess the enhancement factor in comparison to a gold thin film. The obtained experimental images of surfaces featuring subwavelength structures not only provided valuable validation but also offered further insights into the optical properties of the plasmonic structures.

Overall, periodic arrays of plasmonic nanoparticles held immense significance in the fields of nanoscience and nanotechnology, particularly for the development of advanced nanophotonic circuitry. The capacity to achieve precise control over plasmonic dispersion, high-Q resonances, and subwavelength control of nano-optical fields through meticulously designed nanostructures continues to be a subject of ongoing research and exploration.

I. LIST OF PUBLICATIONS BASED ON THE THESIS

1. Mas-ud A. Abdulkareem, Fernando López-Rayón, Citlalli T. Sosa-Sánchez, Ramsés E. Bautista González, Maximino L. Arroyo Carrasco, Mary Carmen Peña-Gomar, Victor Coello, and Ricardo Téllez-Limón "Band-pass integrated optical filters with hyperbolic metamaterials" *Nanomaterials*, Volume (759) 13. 2023.
2. Mas-ud A. Abdulkareem, C. E. Garcia-Ortiz, V. Coello, Mary Carmen Peña-Gomar Surface Lattice resonance *Journal*, Volume, Page, (2023).

II. PRESENTATIONS IN CONFERENCES

1. Mas-ud A. Abdulkareem Title... *Metanano School 2020*, Department of Physics and Engineering of ITMO University (2020).

1. NAME : Mas/ud Ayodeji Abdulkareem

2. DATE OF BIRTH : 15 Oct 1985

3. EDUCATIONAL QUALIFICATIONS

2013 Bachelor of Science

Institution : Adekunle Ajasin University Akungba Akoko
Specialization : Physics and Electronics

2015 Master of Science (M. Sc.)

Institution : African University of Science and Technology Abuja
Specialization : Theoretical Physics

Doctor of Philosphy

Institution : Universidad Michoacana de San Nicolas de Hidalgo
Specialization : Engineering Physics
Registration Date : 1 March 2017

CHAIRPERSON	:	Dr. Mary Carmen Peña-Gomar Professor Faculty of Mathematical Physics and Sciences, UMSNH
GUIDE	:	Dr. Victor Coello Cardenas Manuel Professor Unidad Foránea Monterrey, CICESE
MEMBERS	:	Dr. Ricardo Tellez-Limón Researcher Unidad Monterrey, CICESE
		Dr. Hector Perez Aguilar Professor Faculty of Mathematical Physics and Sciences, UMSNH
		Dr. Gonzalo Viramontes Gamboa Professor Faculty of Mathematical Physics and Sciences, UMSNH

Bibliography

A. A. Bergwerff, F. van Knapen (2006). "Surface Plasmon Resonance Biosensors for Detection of Pathogenic Microorganisms: Strategies to Secure Food and Environmental Safety." In: *Journal of AOAC International* 89 (3), pp. 826–831.

A. Ferraro J. M. Djouda, G. E. Lio G. Leveque P.-M. Adam C. P. Umeton T. Maurer and R. Caputo (2022). "Investigation of Lattice Plasmon Modes in 2D Arrays of Au Nanoantennas". In: *Crystals* 12 (3), pp. 336–345. DOI: 10.1021/acs.jpcc.6b11321. URL: https://doi.org/10.1021/acs.jpcc.6b11321.

A. Pors, S.I. Bozhevolnyi (2008). "Plasmonic metasurfaces for efficient phase control in reflection". In: *New J. Phys.* 21.22, p. 27438. URL: https://doi.org/10.1364/OE.21.027438.

Arianfard, H., J. Wu, and D.J. Moss (2020). "Ultra-sharp Fano resonances in integrated photonic resonators based on coupled Sagnac loop reflectors". In: *2020 Conference on Lasers and Electro-Optics Pacific Rim (CLEO-PR)*.

A.Taflove and M. E. Brodwin (1975a). "Numerical-solution of steady-state electromagnetic scattering problems using time-dependent Maxwell's equations". In: *IEEE Transactions on Microwave Theory and Techniques* 23.3, 623–630. DOI: 10.1109/TMTT.1975.1128640. URL: https://doi.org/10.1109/TMTT.1975.1128708.

A.Taflove and M.E. Brodwin (1975b). "Computation of electromagnetic-fields and induced temperatures within a model of a microwave-irradiated human eye". In: *IEEE Transactions on Microwave Theory and Techniques* 23.11, 888–896. DOI: 10.1109/TMTT.1975.1128640. URL: https://doi.org/10.1109/TMTT.1975.1128640.

B, Rothenhäuslar and Knoll W (1988). "Surface-plasmon microscopy". In: *Nature* 332.615.

B. B. Rajeeva, L. Lin and Y. B. Zheng (2018). "Design and applications of lattice plasmon resonances". In: *Nano Research* 11, 4423–4440. URL: https://doi.org/10.1007/s12274-017-1909-4.

B. Lamprecht G. Schider, R. Lechner H. Ditlbacher J. Krenn A. Leitner and F. Aussenegg (2000). "Metal Nanoparticle Gratings: Influence of Dipolar Particle Interaction on the plasmon resonance". In: *Phy. Rev. Lett.* 84 (20), p. 4721. DOI: 10.1103/PhysRevLett.84.4721. URL: https://doi.org/10.1103/PhysRevLett.84.4721.

Barchiesi, Dominique and Thomas Grosges (2014). "Resonance in metallic nanoparticles: A rigorous formulation of the dipolar approximation". In: *European Journal of Physics* 35.3. ISSN: 13616404. DOI: 10.1088/0143-0807/35/3/035012.

Barrios Carlos Angulo; Mirea, Teona; Represa Miguel Huerga; (2023). "A Self-Referenced Refractive Index Sensor Based on Gold Nanoislands." In: *Sensors* 23 (1), pp. 66–77. URL: https://doi.org/10.3390/s23010066.

Beermann, J. and S. I. Bozhevolnyi (2004). "Second-harmonic near-field optical microscopy of periodic nanoholes in metal films". In: *Laser Physics Letters* 1 (12), p. 592.

Beermann, J. and S.I. Bozhevolnyi (2006). "Two-photon luminescence microscopy of field enhancement at gold nanoparticles." In: *Physical Review B - Condensed Matter and Materials Physics vol: 73, issue 11, 2006* 73 (11).

Beermann, J. et al. (2008). "Nonlinear microscopy of localized field enhancements in fractal shaped periodic metal nanostructures". In: *Journal of the Optical Society of America B: Optical Physics vol: 25, issue 10, 2008, pp. 1585-* 25 (10).

Bekele, D.A. et al. (2019). "Towards High-Speed Fano Photonic Switches". In: *2019 21st International Conference on Transparent Optical Networks (ICTON)* 142. URL: http://dx.doi.org/10.1109/ICTON.2019.8840374.

Berenger, J. P. (2007). *Perfect Matched Layer (PML) for Computational Electromagnetics*. Morgan and Claypool.

Berenger, J.P. (1994). "A perfectly matched layer for the absorption of electromagnetic waves". In: *Journal of Computational Physics* 114.2, pp. 185–200. DOI: doi.org/10.1006/jcph.1994.1159. URL: https://doi.org/10.1006/jcph.1994.1159.

Betz, V. and R. Mittra (1992). "Comparison and evaluation of boundary conditions for the absorption of guided waves in an FDTD simulation". In: *IEEE Microwave and GuidedWave Letters* 2.12, 499–501. DOI: 10.1109/75.173408. URL: https://doi.org/10.1109/75.173408.

Bonatti, L. et al. (2020). "Plasmonic Resonances of Metal Nanoparticles: Atomistic vs. Continuum". In: *Frontiers in Chemistry* 8. URL: https://doi.org/10.3389/fchem.2020.00340.

Boyd, Robert Wood (2007). *Nonlinear Optics, Third Edition*. Academic Press.

Bozhevolnyi, S. (2006). "Effective-index modeling of channel Plasmon polaritons". In: *Opt. Exp.* 14 (20), p. 9467. DOI: 10.1364/oe.14.009467.. URL: https://doi.org/10.1364/OE.14.009467.

Bozhevolnyi S.I.; Volkov, V.S.; Leosson K.; (2002). "Localization and Waveguiding of Surface Plasmon Polaritons in Random Nanostructures". In: *Phy. Rev. Lett.* 89 (18).

Broquin, Jean-Emmanuel (2007). "Glass integrated optics: state of the art and position toward other technologies". In: *Integrated Optics: Devices, Materials, and Technologies XI*. Ed. by Yakov Sidorin and Christoph A. Waechter. Vol. 6475. International Society for Optics and Photonics. SPIE, p. 647507. DOI: 10.1117/12.706785. URL: https://doi.org/10.1117/12.706785.

Bushati, R., S. Guddala, and V.M. Menon (2019). "Strong Coupling of Excitons in WS2 with Fano Resonances in Photonic Crystals". In: *2019 Conference on Lasers and Electro-Optics (CLEO), Lasers and Electro-Optics (CLEO)*. URL: http://dx.doi.org/10.1364/CLEO_SI.2019.STh4H.7.

C. Cherqui M.R. Bourgeois, G.C. Schatz D. Wang (2019). "Plasmonic Surface Lattice Resonances: Theory and Computation". In: *Am. Chem. Soc.* 52.9, 2548–2558. URL: https://doi.org/10.1021/acs.accounts.9b00312.

C. Garcia-Ortiz V. Coello, E. Pisano Y. Chen and S. Bozhevolnyi (2019). "Plasmonic directional couplers using channel waveguides in random arrays of metal nanoparticles". In: *Opt. Exp.* 27 (16), p. 22753. DOI: 10.1364/OE.27.022753. URL: https://doi.org/10.1364/OE.27.022753.

C. Garcia-Ortiz R. Cortes, J. Gómez-Correa E. Pisano V. Coello J. Fiutowski H.-G. Rubahn and D. Garcia-Ortiz (2019). "Plasmonic metasurface Luneburg lens". In: *Nat. Mat.* 7 (10), p. 1112. DOI: 10.1364/PRJ.7.001112. URL: https://doi.org/10.1364/PRJ.7.001112.

C. Molinaro Y. El Harfouch, E. Palleau-F. Eloi L. Douillard F. Charra C. Fiorini-Debuisschert S. Marguet (2016). "Two-photon luminescence of single colloidal gold nanorods: revealing the origin of plasmon relaxation in small nanocrystals". In: *Phys. Chem. C* 120.40, pp. 23136–23143. URL: https://doi.org/10.1021/acs.jpcc.6b07498.

C.E. Garcia-Ortiz V. Coello, E. Pisano-Y. Chen S.I. Bozhevolnyi (2019). "Plasmonic directional couplers using channel waveguides in random arrays of metal nanoparticles". In: *Opt. Exp.* 27.16. URL: https://doi.org/10.1364/OE.27.022753.

Coello, V. (2008a). "Surface Plasmon Polariton Localization". In: *Surf. Rev. and Lett.* 15.6. URL: https://doi.org/10.1142/S0218625X08011974.

Coello, V.; (2008b). "Surface plasmon polariton localization". In: *Surf. Rev. and Lett.* 15 (6), p. 867.

Colburn S.; Majumdar, A.; Zhan A.; (2018). "Metasurface optics for full-color computational imaging". In: *Science Advances.* 4 (2), pp. 1–6.

Ditlbacher, H. et al. (2005). "Silver nanowires as surface plasmon resonators". In: *Phys. Rev. Lett.* 95.25. URL: https://doi.org/10.1103/PhysRevLett.95.257403.

Drachev, Vladimir P., Viktor A. Podolskiy, and Alexander V. Kildishev (2013). "Hyperbolic metamaterials: new physics behind a classical problem". In: *Opt. Express* 21.12, pp. 15048–15064. DOI: 10.1364/OE.21.015048. URL: https://opg.optica.org/oe/abstract.cfm?URI=oe-21-12-15048.

D.Wang et al. (2020). "Surface enhanced, infrared absorption of ligands on colloidal gold nanowires through resonant coupling". In: *Am.Chem. Soc.* 92.5, 3494–3498. URL: https://doi.org/10.1021/acs.analchem.9b04885.

F. Ding Y. Yang, R. Deshpande and S. Bozhevolnyi (2018). "A Review of Gap Surface Plasmon Metasurfaces: Fundamentals and Applications". In: *Nanophotonics* 7 (6), p. 1129. DOI: 10.1515/nanoph-2017-0125. URL: https://doi.org/10.1515/nanoph-2017-0125.

Fantoni, A. et al. (2017). "Local Surface Plasmon Resonance of metallic Nanoparticles Embedded in Amorphous Silicon". In: *App. Phys. Lett.* 29.1. URL: http://dx.doi.org/10.1016/j.ctmat.2016.06.011.

Feng, R. et al. (2014). "Dual-band infrared perfect absorber based on asymmetric T-shaped plasmonic array". In: *Opt. Exp.* 22.2, A335–A343. URL: https://doi.org/10.1364/OE.22.00A335.

Ferrari, Lorenzo et al. (2015). "Hyperbolic metamaterials and their applications". In: *Progress in Quantum Electronics* 40, pp. 1–40. ISSN: 0079-6727. DOI: https://doi.org/10.1016/j.pquantelec.2014.10.001. URL: https://www.sciencedirect.com/science/article/pii/S0079672714000408.

G. E. Johnstone G. S. Cairns, B. R. Patton (2019). "Nanodiamonds enable adaptive-optics enhanced, super-resolution, two-photon excitation microscopy". In: *Royal Society Open Science* 6 (7).

G. E. Lio J. B. Madrigal, C. Couteau S. Blaize and R. Caputo (2015). "Polarization interferometry for real-time spectroscopic plasmonic sensing". In: *Nanoscale.* 7 (9), p. 4226.

— (2020). "Conceptual Implementation of a Photonic–Plasmonic Transistor onto a Structured Nano-Guided Hybrid System". In: *Physica Status Solidi (A) Applications and Materials Science* 217 (11), p. 1900911. DOI: 10.1002/pssa.201900911. URL: https://doi.org/10.1002/pssa.201900911.

G. Lio A. Ferraro, M. Giocondo R. Caputo and A. De Luca (2020). "Color Gamut Behavior in Epsilon Near-Zero Nanocavities during Propagation of Gap Surface Plasmons." In: *Adv. Opt. Mater* 8 (17), p. 2020. DOI: 10.1002/adom.202000487. URL: https://doi.org/10.1002/adom.202000487.

Garcia, C. et al. (2012). "Partial loss compensation in dielectric-loaded plasmonic waveguides at near infra-red wavelengths". In: *Opt. Exp.* 20.7, pp. 7771–7776. URL: https://doi.org/10.1364/OE.20.007771.

Ghindani D.; Rashed, A.R.; Habib M.; Caglayan H.; (2021). "Gate Tunable Coupling of Epsilon-Near-Zero and Plasmonic Modes". In: *Adv. Opt. Mat.* 9 (22).

Giovannini, T. et al. (2019). "A classical picture of subnanometer junctions: an atomistic Drude approach to nanoplasmonics". In: *Nanoscale*. URL: https://doi.org/10.1039/C8NR09134J.

G.Mur (1981). "Absorbing boundary-conditions for the finite-difference approximation of the timedomain electromagnetic-field equations". In: *IEEE Transactions on Electromagnetic Compatibility* EMC-23.4, 377–382. DOI: 10.1109/TEMC.1981.303970. URL: https://doi.org/10.1109/TEMC.1981.303970.

Gutha, R.R., S.M. Sadeghi, and W.J. Wing (2017). "Ultrahigh refractive index sensitivity and tunable polarization switching via infrared plasmonic lattice modes". In: *Appl. Phys. Lett.* 110.153103. URL: https://doi.org/10.1063/1.4980060.

H. Saito D. Yoshimoto, H. Loureno-Martins N. Yamamoto T. Sannomiya (2019). "Hybridization of gap modes and lattice modes in a plasmonic resonator array with a metal-Insulator-Metal Structure". In: *ACS Photonics* 6.11, pp. 2618–2625. URL: https://doi.org/10.1021/acsphotonics.9b00977.

Han, Z. et al. (2009). "Detuned-resonator induced transparency in dielectric-loaded plasmonic waveguides". In: *Opt. Lett.* 38.14. URL: https://doi.org/10.1364/OL.38.000875.

Higdon, R. L. (1986). "Absorbing boundary-conditions for difference approximations to the multidimensional wave-equation". In: *Mathematics of Computation* 47.176, pp. 437–459. DOI: doi.org/10.2307/2008166. URL: https://doi.org/10.2307/2008166.

Hohenau, A. et al. (2007). "Spectroscopy and nonlinear microscopy of gold nanoparticle arrays on gold films." In: *Physical Review B - Condensed Matter and Materials Physics* 75 (8).

Holmgaard, Tobias et al. (2009). "Dielectric-loaded plasmonic waveguide-ring resonators". In: *Opt. Express* 17.4, pp. 2968–2975. DOI: 10.1364/OE.17.002968. URL: https://opg.optica.org/oe/abstract.cfm?URI=oe-17-4-2968.

Horton Matthew J.; Ojambati, Oluwafemi S.; Chikkaraddy Rohit; Deacon William M.; Kongsuwan Nuttawut; Demetriadou Angela; Hess Ortwin; Baumberg Jeremy J.; (2020). "Nanoscopy through a plasmonic nanolens". In: *PNAS* 117 (5), p. 2275. DOI: 10.1073/pnas.1914713117. URL: https://doi.org/10.1073/pnas.1914713117.

Humphrey, A. and W. Barnes (2018). "Plasmonic surface lattice resonances on arrays of different lattice symmetry". In: *Chemical reviews* 90 (075404), 5912–5951. DOI: 10.1021/acs.chemrev.8b00243. URL: https://doi.org/10.1021/acs.chemrev.8b00243.

J. Beermann S.I. Bozhevolnyi, V. Coello (2006a). "Modeling of nonlinear microscopy of localized field enhancements in random metal nanostructures". In: *Phy. Rev.- Condensed Matter and Materials Phys.* 73.11. URL: https://doi.org/10.1103/PhysRevB.73.115408.

— (2006b). "Modeling of nonlinear microscopy of localized field enhancements in random metal nanostructures". In: *Physical Review B - Condensed Matter and Materials Physics vol: 73, issue 11, 2006* 73 (11).

J. Duffy F. Padovani, G. Brunetti P. Noy U. Certa M. Hegner (2018). "Towards personalised rapid label free miRNA detection for cancer and liver injury diagnostics in cell lysates and blood based samples." In: *Nanoscale* 10 (26), p. 12797.

J. Gömez-Correa N. Puente, V. Coello S. Balderas-Mata J. Rogel-Salazar and S. Chávez-Cerda (2017). "On the physics of propagating bessel modes in cylindrical waveguides, vol. 85, no. 5, p. 341, 2017." In: *Am. J. of Phy.* 85 (5), p. 341. DOI: 10.48550/arXiv.1612.01959. URL: https://doi.org/10.48550/arXiv.1612.01959.

J. Homola K. Hegnerová, M. Vala (2009). "Surface plasmon resonance biosensors for detection of foodborne pathogens and toxins." In: *Progress in Biomedical Optics and Imaging - Proceedings of SPIE vol: 7167, 2009* 7167, p. 8343.

J. Jung T. Søndergaard, S.I. Bozhevolnyi (2009). "Gap plasmon-polariton nanoresonators: scattering enhancement and launching of surface plasmon polaritons". In: *Phys Rev B* 79.3, p. 35401. URL: https://doi.org/10.1103/PhysRevB.79.035401.

J. Lin J.P. Mueller, Q. Wang G. Yuan N. Antoniou X. Yuan-F. Capasso. (2013). "Polarization-Controlled Tunable Directional Coupling of Surface Plasmon Polaritons". In: *Science* 340 (6130), p. 331.

J. Luo, Y.S. Lin (2019). "High-efficiency of infrared absorption by using composited metamaterial nanotubes". In: *App. Phys. Lett.* 114.5. URL: https://doi.org/10.1063/1.5063736.

J. Yin M. Peng, W. Lin (2019). "Two-photon fluorescence imaging of lipid drops polarity toward cancer diagnosis in living cells and tissue". In: *Sensors and Actuators, B: Chemical* 288, p. 251.

Jackson, J.D. (1998). *Classical Electrodynamics*. Wiley.

Jin, Yabin et al. (2016). "Tunable waveguide and cavity in a phononic crystal plate by controlling whispering-gallery modes in hollow pillars". In: *Phys. Rev. B* 93 (5), p. 054109. DOI: 10.1103/PhysRevB.93.054109. URL: https://link.aps.org/doi/10.1103/PhysRevB.93.054109.

K. Whang Y. Shin, T. Kang J.H. Lee L.P. Lee W. Lee-Y.W. Kim D. Kim (2018). "Plasmonic bacteria on a nanoporous mirror via hydrodynamic trapping for rapid identification of waterborne pathogens". In: *Light: Science and Applications* 7 (1).

Kalusniak, Sascha, Laura Orphal, and Sergey Sadofev (2015). "Demonstration of hyperbolic metamaterials at telecommunication wavelength using Ga-doped ZnO". In: *Opt. Express* 23.25, pp. 32555–32560. DOI: 10.1364/OE.23.032555. URL: https://opg.optica.org/oe/abstract.cfm?URI=oe-23-25-32555.

Khani, Shiva, Mohammad Danaie, and Pejman Rezaei (2018). "Realization of single-mode plasmonic bandpass filters using improved nanodisk resonators". In: *Optics Communications* 420, pp. 147–156. ISSN: 0030-4018. DOI: https://doi.org/10.1016/j.optcom.2018.03.047. URL: https://www.sciencedirect.com/science/article/pii/S0030401818302268.

Kidwai, Omar, Sergei V. Zhukovsky, and J. E. Sipe (2012). "Effective-medium approach to planar multilayer hyperbolic metamaterials: Strengths and limitations". In: *Phys. Rev. A* 85 (5), p. 053842. DOI: 10.1103/PhysRevA.85.053842. URL: https://link.aps.org/doi/10.1103/PhysRevA.85.053842.

Kogelnik, H. (1975). "An Introduction to Integrated Optics". In: *IEEE Transactions on Microwave Theory and Techniques* 23.1, pp. 2–16. DOI: 10.1109/TMTT.1975.1128500.

L. Huang X. Chen, S. Zhang B. Bai Q. Tan G. Jin-T. Zentgraf. (2013). "Helicity dependent directional surface plasmon polariton excitation using a metasurface with interfacial phase discontinuity". In: *Light: Science and Applications vol: 2, issue MARCH, 2013* 2 (March).

Leveque, G. and O.J.F. Martin (2006). "Optical Interactions in a Plasmonic Particle Coupled to a Metallic Film". In: *Opt. Exp.* 14.21, p. 9971. URL: https://doi.org/10.1364/OE.14.009971.

Li; Seongmin Hong; Xiao (2013). "Optimal Size of Gold Nanoparticles for Surface-Enhanced Raman Spectroscopy under Different Conditions." In: *Nanomaterials* 2013.1 (49). URL: https://doi.org/10.1155/2013/790323.

Liang, Y. et al. (2018). "Comparative investigation of sensing behaviors between gap and lattice plasmon modes in a metallic nanoring array". In: *Nanoscale* 10, pp. 548–555. URL: https://doi.org/10.1039/C7NR07124H.

Lin, Xian-Shi and Xu-Guang Huang (2008). "Tooth-shaped plasmonic waveguide filters with nanometeric sizes". In: *Opt. Lett.* 33.23, pp. 2874–2876. DOI: 10.1364/OL.33.002874. URL: https://opg.optica.org/ol/abstract.cfm?URI=ol-33-23-2874.

Lio G.E.; Ferraro, A.; Ritacco T.; De Luca A.; Giocondo M.; Caputo-R.; Aceti D.M.; (2021). "Leveraging on ENZ Metamaterials to Achieve 2D and 3D Hyper-Resolution in Two-Photon Direct Laser Writing". In: *Adv. Mat.* 33 (18).

Lio G.E.; De Luca, A.; Umeton C.P.; Caputo R.; (2020). "Opto-mechanically induced thermoplasmonic response of unclonable flexible tags with hotspot fingerprint". In: *App. Phys.* 128 (9).

Lu, Hua et al. (2010). "Tunable band-pass plasmonic waveguide filters with nanodisk resonators". In: *Opt. Express* 18.17, pp. 17922–17927. DOI: 10.1364/OE.18.017922. URL: https://opg.optica.org/oe/abstract.cfm?URI=oe-18-17-17922.

Luk'yanchuk, B.S. et al. (2007). "Peculiarities of light scattering by nanoparticles and nanowires near plasmon resonance frequencies in weakly dissipating materials". In: *Optics A: Pure and Applied Optics* 9.9, pp. 294 –304. URL: DOI:10.1038/nmat2810.

Luk'yanchuk1, Boris et al. (2010). "the Fano resonance in plasmonic nanostructures and metamaterials". In: *Nat. Mat.* 9.9, pp. 707 –715. URL: DOI:10.1038/nmat2810.

López-Rayón, Fernando et al. (2022). "Plasmonic-Induced Transparencies in an Integrated Metaphotonic System". In: *Nanomaterials* 12.10. ISSN: 2079-4991. DOI: 10.3390/nano12101701. URL: https://www.mdpi.com/2079-4991/12/10/1701.

Ma, H., A.K.-Y. Jen, and L.R. Dalton (2002). "Polymer-Based Optical Waveguides: Materials, Processing, and Devices". In: *Advanced Materials* 14.19, pp. 1339–1365. DOI: https://doi.org/10.1002/1521-4095(20021002)14:19<1339::AID-ADMA1339>3.0.CO;2-O.

Matsko, A.B. and V.S. Ilchenko (2006). "Optical resonators with whispering-gallery modes-part I: basics". In: *IEEE Journal of Selected Topics in Quantum Electronics* 12.1, pp. 3–14. DOI: 10.1109/JSTQE.2005.862952.

Mendez-Astudillo, Manuel, Hideaki Okayama, and Hirochika Nakajima (2018). "Silicon optical filter with transmission peaks in wide stopband obtained by anti-symmetric photonic crystal with defect in multimode waveguides". In: *Opt. Express* 26.2, pp. 1841–1850. DOI: 10.1364/OE.26.001841. URL: https://opg.optica.org/oe/abstract.cfm?URI=oe-26-2-1841.

M.G. Nielsen O. Albrektsen, S.I. Bozhevolnyi A. Pors R.B. Nielsen A. Boltasseva (2010). "Investigations of scattering and field enhancement effects in retardation-based plasmonic nanoantennas". In: *Proc. of SPIE* 7757. URL: https://doi.org/10.1117/12.868363.

Moreno, F., F. Gonzalez, and J.M. Saiz (2006). "Plasmon Spectroscopy of Metallic Nanoparticles Above Flat Dielectric Substrates". In: *Opt. Lett.* 31.12, p. 1902. URL: https://doi.org/10.1364/OL.31.001902.

N. Bellassai R. D'Agata, V. Jungbluth G. Spoto (2019). "Surface Plasmon Resonance for Biomarker Detection: Advances in Non-invasive Cancer Diagnosis". In: *Frontiers in Chemistry* 7.

N. Felidj G. Laurent, J. Aubard G. Lévi A. Hohenau J.R. Krenn-F.R. Aussenegg (2005). "Grating-induced plasmon mode in gold nanoparticle arrays". In: *Chm. Phy.* 123.221103. URL: https://doi.org/10.1063/1.2140699.

N. Mahi G. Léveque, O. Saison A. Akjouj B. Bouhafs J. Marae-Djouda R. Caputo and A. Gontier (2017). "In Depth Investigation of Lattice Plasmon Modes in Substrate-Supported Gratings of Metal Monomers and Dimers". In: *Phys. Chem.* 121 (4), p. 2388.

DOI: 10.1021/acs.jpcc.6b11321. URL: https://doi.org/10.1021/acs.jpcc.6b11321.

Naik, Gururaj V. et al. (2012). "Demonstration of Al:ZnO as a plasmonic component for near-infrared metamaterials". In: *Proceedings of the National Academy of Sciences* 109.23, pp. 8834–8838. DOI: 10.1073/pnas.1121517109. eprint: https://www.pnas.org/doi/pdf/10.1073/pnas.1121517109. URL: https://www.pnas.org/doi/abs/10.1073/pnas.1121517109.

Neutens, P. et al. (2012). "Plasmon filters and resonators in metal-insulator-metal waveguides". In: *Opt. Express* 20.4, pp. 3408–3423. DOI: 10.1364/OE.20.003408. URL: https://opg.optica.org/oe/abstract.cfm?URI=oe-20-4-3408.

Novikov, S. M. et al. (2009). "Two-photon imaging of field enhancement by groups of gold nanostrip antennas". In: *Journal of the Optical Society of America B: Optical Physics* 26 (11), p. 2199.

Novikov, S.M. et al. (2016). "Enhancement of two-photon photoluminescence and SERS for low-coverage gold films." In: *Opt. Exp.* 24 (15), p. 12797.

Okamoto, Katsunari (1999). "Recent progress of integrated optics planar lightwave circuits". In: *Optical and Quantum Electronics* 31.2, pp. 107–129. DOI: 10.1023/A:1006975415469. URL: https://doi.org/10.1023/A:1006975415469.

P. Segovia, V. Coello (2012). "Elastic surface plasmon polariton scattering: Near- and far-field interactions". In: *Nano* 7.1. URL: https://doi.org/10.1142/S1793292011500032.

Papanikolaou, N. (2007). "Optical Properties of Metallic Nanoparticles Arrays on a Thin Metallic Film". In: *Phys. Rev.* ***B*** 75.23. URL: https://doi.org/10.1103/PhysRevB.75.235426.

Pérez-Galacho, Diego et al. (2017). "Optical pump-rejection filter based on silicon subwavelength engineered photonic structures". In: *Opt. Lett.* 42.8, pp. 1468–1471. DOI: 10.1364/OL.42.001468. URL: https://opg.optica.org/ol/abstract.cfm?URI=ol-42-8-1468.

Pisano, E. et al. (2016). "Plasmonic channel waveguides in random arrays of metallic nanoparticles." In: *Opt. Exp.* 24 (15), p. 12797.

"Plasmons in Strongly Coupled Metallic Nanostructures" (2011). In: *ACS* 114.2, 3913–3961. DOI: https://doi.org/10.1021/cr200061k.

Poddubny, Alexander et al. (2013). "Hyperbolic metamaterials". In: *Nature Photonics* 7.12, pp. 948–957. DOI: 10.1038/nphoton.2013.243. URL: https://doi.org/10.1038/nphoton.2013.243.

Pors, A. and S. Bozhevolnyi (2013a). "Efficient and broadband quarter-wave plates by gap-plasmon resonators, vol. 21, no. 3, p. 2942, 2013." In: *Opt. Exp.* 21 (3), p. 2942. DOI: 10.1364/OE.21.002942. URL: https://doi.org/10.1364/OE.21.002942.

Pors, A. and S.I Bozhevolnyi (2013b). "Efficient and broadband quarter-wave plates by gap-plasmon resonators". In: *Opt. Express* 21.3, pp. 2942–2952. URL: https://doi.org/10.1364/OE.21.002942.

Quaranta, Giorgio et al. (2018). "Recent Advances in Resonant Waveguide Gratings". In: *Laser & Photonics Reviews* 12.9, p. 1800017. DOI: https://doi.org/10.1002/lpor.201800017. eprint: https://onlinelibrary.wiley.com/

doi/pdf/10.1002/lpor.201800017. URL: https://onlinelibrary.wiley.com/doi/abs/10.1002/lpor.201800017.

R., Linic S.; Chavez S.; Elias (2021). "Flow and extraction of energy and charge carriers in hybrid plasmonic nanostructures". In: *Nat. Mat.* 20 (7), p. 916. DOI: 10.1038/s41563-020-00858-4. URL: https://doi.org/10.1038/s41563-020-00858-4.

R. Bukasov, J.S. Shumaker-Parry (2009). "Silver nanocrescents with infrared plasmonic properties as tunable substrates for surface enhanced infrared absorption spectroscopy". In: *Anal. Chem.* 81.11. URL: https://doi.org/10.1021/ac900477p.

R. Tellez-Limon M. Février, A. Apuzzo R. Salas-Montiel and S. Blaize (2017). "Numerical analysis of tip-localized surface plasmon resonances in periodic arrays of gold nanowires with triangular cross-section." In: *Opt. Journal of the Opt. Soc. of Am. B* 34 (10), p. 341. DOI: 10.1364/JOSAB.34.002147. URL: https://doi.org/10.1364/JOSAB.34.002147.

R. Tellez-Limon F. Gardillou, V. Coello and R. Salas-Montiel (2021). "Coupled localized surface plasmon resonances in periodic arrays of gold nanowires on ion-exchange waveguide technology". In: *Journal of Optics* 23.2. URL: https://ui.adsabs.harvard.edu/link_gateway/2021JOpt...23b5801T/doi:10.1088/2040-8986/abcfd5.

R. Xu, Y.S Lin (2018). "Characterizations of reconfigurable infrared metamaterial absorbers". In: *Opt. Lett.* 43.19, pp. 4783–4786. URL: https://doi.org/10.1364/OL.43.004783.

Rabus, Dominik G. and Cinzia Sada (2020). *Integrated ring resonators. A compendium*. 2nd ed. Springer Cham, p. 360. ISBN: 978-3-030-60130-0. URL: https://doi.org/10.1007/978-3-030-60131-7.

Ritchie, R.H (1957). "Plasma Losses by Fast Electrons in Thin Films". In: *Phy. Rev.* 106.5.

Rivera, V.A.G., F.A. Ferri, and E. Marega Jr. (2012). "Localized Surface Plasmon Resonances:Noble Metal Nanoparticle Interaction with Rare-Earth Ions". In: *Plasmonics: Principles and applications*, pp. 283–312. URL: http://dx.doi.org/10.5772/50753.

Rizza, Carlo et al. (2012). "Terahertz active spatial filtering through optically tunable hyperbolic metamaterials". In: *Opt. Lett.* 37.16, pp. 3345–3347. DOI: 10.1364/OL.37.003345. URL: https://opg.optica.org/ol/abstract.cfm?URI=ol-37-16-3345.

R.L.Higdon (1987). "Numerical absorbing boundary-conditions for the wave-equation". In: *Mathematics of Computation* 49.179, pp. 65–90. DOI: doi.org/10.2307/2008250. URL: https://doi.org/10.2307/2008250.

Rytov, S. (1956). "Electromagnetic properties of a finely stratified medium". In: *Soviet Physics JEPT* 2.3, pp. 466–475.

S. Motamedi T. Shilagard, K. Edward L. Koong G. Vargas S. Qui (2011). "Gold nanorods for intravital vascular imaging of preneoplastic oral mucosa". In: *Biomedical Optics Express* 2 (5), p. 1194.

Saudan, Q. et al. (2019). " Low-Power Thermo-Optic Switching Using Photonic Crystal Fano Structure with p-i-n Junction". In: *2019 21st International Conference on Transparent Optical Networks (ICTON)*. URL: https://doi.org/10.1109/ICTON.2019.8840273.

Shalaev, Vladimir M. (1996). "Electromagnetic properties of small-particle composites". In: *Physics Report* 272, p. 61.

Shekhar, Prashant, Jonathan Atkinson, and Zubin Jacob (2014). "Hyperbolic metamaterials: fundamentals and applications". In: *Nano Convergence* 1.1, pp. 1–14. DOI: 10.1186/s40580-014-0014-6. URL: https://doi.org/10.1186/s40580-014-0014-6.

Singh, M. and S.K. Raghuwanshi (2018). "Metal-insulator-metal waveguide based passive structures analyzed by transmission line model". In: *Superlattices and Microstructures* 114.233, pp. 233–241. URL: https://doi.org/10.1016/j.spmi.2017.12.041.

S.J. Erik L. Novotny, X.S. Xie (1999). "Near-field fluorescence microscopy based on two-photon excitation with metal tips". In: *Physical Review Letters* 82 (20), p. 4014.

S.M. Novikov J. Beermann, S.I. Bozhevolnyi Søndergaard A.E. Boltasseva (2009). "Two-photon imaging of field enhancement by groups of gold nanostrip antennas". In: *Opt. Soc. of Am.**B*** 26.11. URL: https://doi.org/10.1364/JOSAB.26.002199.

Sohler, Wolfgang et al. (2008). "Integrated Optical Devices in Lithium Niobate". In: *Opt. Photon. News* 19.1, pp. 24–31. DOI: 10.1364/OPN.19.1.000024. URL: https://www.optica-opn.org/abstract.cfm?URI=opn-19-1-24.

Stephen, D.G. (2011). *Introduction to the Finite Difference Time-Domain (FDTD) Method for Electromagnetics*. Morgan and Claypool Publishers.

Su, W. et al. (2021). "Multi-Fano Resonances in Graphene Coated All-Dielectric Metasurface for Refractive Index Sensing With High Figure of Merits". In: *IEEE Journal of Selected Topics in Quantum Electronics* 27.1. URL: https://doi.org/10.1109/JSTQE.2020.2991884.

Suhara, T. and H. Nishihara (1986). "Integrated optics components and devices using periodic structures". In: *IEEE Journal of Quantum Electronics* 22.6, pp. 845–867. DOI: 10.1109/JQE.1986.1073051.

Swartz, M. et al. (2016). "Aluminum Nanocrescent Plasmonic Antennas Fabricated by Copper Mask Nanosphere Template Lithography". In: *Phys. Chem. **C*** 120.37. URL: https://doi.org/10.1021/acs.jpcc.6b00396.

T. Qing J. Liu, S. Ke B. Wang P. Lu. (2020). "Directional Excitation of Surface Plasmon Polaritons by Circularly Polarized Vortex Beams." In: *Plasmonics* 15 (3), pp. 727–734.

T. Søndergaard J. Jung, Bozhevolnyi SI Valle GD (2005). "Towards Advanced Chemical and Biological Nanosensors- An Overview". In: *Talanta* 67.3, pp. 438–448. URL: https://doi.org/10.1016/j.talanta.2005.06.039.

T. Søndergaard, S. Bozhevolnyi (2007). "Slow-plasmon resonant nanostructures: scattering and field enhancements". In: *Phys. Rev. B* 75.7. URL: https://doi.org/10.1103/PhysRevB.75.073402.

Taflove, A. (1984). *Advances in Computational Electrodynamics- The Finite Difference Time-Domain Method*. Phys. Rev. Lett.

Tan, D. T. H., K. Ikeda, and Y. Fainman (2009). "Cladding-modulated Bragg gratings in silicon waveguides". In: *Opt. Lett.* 34.9, pp. 1357–1359. DOI: 10.1364/OL.34.001357. URL: https://opg.optica.org/ol/abstract.cfm?URI=ol-34-9-1357.

Tao, Jin et al. (2009). "A narrow-band subwavelength plasmonic waveguide filter with asymmetrical multiple-teeth-shaped structure". In: *Opt. Express* 17.16, pp. 13989–13994. DOI: 10.1364/OE.17.013989. URL: https://opg.optica.org/oe/abstract.cfm?URI=oe-17-16-13989.

Tellez-Limon, Ricardo et al. (2020). "Excitation of surface plasmon polaritons in a gold nanoslab on ion-exchanged waveguide technology". In: *Appl. Opt.* 59.2, pp. 572–578. DOI: 10.1364/AO.381915. URL: https://opg.optica.org/ao/abstract.cfm?URI=ao-59-2-572.

T.H. Xiao Z. Cheng, K. Goda Z. Zhao M. Takenaka W. Zhou-H.K. Tsang (2018). "High-Q germanium optical nanocavity". In: *Photonics Research* 6.9, pp. 925–928. URL: https://doi.org/10.1364/PRJ.6.000925.

Tharwat M.M.; Almalki, A.; Mahros A.M.; (2021). "Plasmon-enhanced sunlight harvesting in thin-film solar cell by randomly distributed nanoparticle array". In: *Materials* 14 (6), p. 1. URL: https://doi.org/10.3390/ma14061380.

Tong, Xingcun Colin (2013). *Advanced materials for integrated optical waveguides*. Springer Cham, p. 552. ISBN: 978-3-319-01549-1. URL: https://doi.org/10.1007/978-3-319-01550-7.

Tumkur, T. et al. (2015). "Permittivity evaluation of multilayered hyperbolic metamaterials: Ellipsometry vs. reflectometry". In: *Journal of Applied Physics* 117.10, p. 103104. DOI: 10.1063/1.4914524. eprint: https://doi.org/10.1063/1.4914524. URL: https://doi.org/10.1063/1.4914524.

Téllez-Limón, Ricardo and Rafael Salas-Montiel (2021). "Nanowires Integrated to Optical Waveguides". In: *Nanowires*. Ed. by Xihong Peng. Rijeka: IntechOpen. Chap. 8. DOI: 10.5772/intechopen.95689. URL: https://doi.org/10.5772/intechopen.95689.

Urbas, Augustine M et al. (2016). "Roadmap on optical metamaterials". In: *Journal of Optics* 18.9, p. 093005. DOI: 10.1088/2040-8978/18/9/093005. URL: https://dx.doi.org/10.1088/2040-8978/18/9/093005.

V. Coello, S.I. Bozhevolnyi (2009). "Surface plasmon polariton excitation and manipulation by nanoparticle arrays". In: *Opt. Comm.* 282.14, pp. 3032–3036. URL: https://doi.org/10.1016/j.optcom.2009.04.012.

V.A. Zenin I.P. Radko, V.S. Volkov S.I. Bozhevolnyi A. Andryieuski R. Malureanu-A.V. Lavrinenko D.K. Gramotnev (2015). "Boosting Local Field Enhancement by on-Chip Nanofocusing and Impedance-Matched Plasmonic Antennas". In: *Nano Letters* 15 (12), p. 8148.

V.G. Kravets A.V. Kabashin, W.L. Barnes A.N. Grigorenko (2018). "Plasmonic Surface Lattice Resonances: A Review of Properties and Applications". In: *Chem. Rev.* 118.12, 5912–5951. URL: https://doi.org/10.1021/acs.chemrev.8b00243.

Vial, Alexandre et al. (2005). "Improved analytical fit of gold dispersion: Application to the modeling of extinction spectra with a finite-difference time-domain method". In:

Phys. Rev. B 71 (8), p. 085416. DOI: 10.1103/PhysRevB.71.085416. URL: https://link.aps.org/doi/10.1103/PhysRevB.71.085416.

Wittig, Tilmann, Rolf Schuhmann, and Thomas Weiland (2006). "Model order reduction for large systems in computational electromagnetics". In: *Linear Algebra and its Applications* 415.2. Special Issue on Order Reduction of Large-Scale Systems, pp. 499–530. ISSN: 0024-3795. DOI: https://doi.org/10.1016/j.laa.2004.06.023. URL: https://www.sciencedirect.com/science/article/pii/S0024379504002915.

Woods, R.W. (1902). "On a remarkable case of uneven distribution of light in a diffraction grating spectrum". In: *Phil. Mag. 4* 393.

X. Wang H. Shi, N. Wang L. Cheng Y. Gao L. Huang-Y. Jiang (2014). "Two-Photon Luminescence and Second Harmonic Generation from Gold Micro-Plates". In: *Sensors* 14.10, 18328–18336. URL: https://dx.doi.org/10.33902\%Fs141018328.

X. Yang G. Xiao, Y. Lu and G. Li (2019). "Narrow plasmonic surface lattice resonances with preference to asymmetric dielectric environment". In: *Opt. Exp.* 27 (18), p. 341. DOI: 10.1364/OE.27.025384. URL: https://doi.org/10.1364/OE.27.025384.

X. Yang L. Xiong, Y. Lu and G. Li (2020). "Exceptionally narrow plasmonic surface lattice resonances in gold nanohemisphere array". In: *Journal of Physics D* 53 (46), p. 341. DOI: 10.48550/arXiv.1612.01959. URL: https://doi.org/10.48550/arXiv.1612.01959.

Y. Wang W. Knoll, J. Dostalek (2012). "Bacterial pathogen surface plasmon resonance biosensor advanced by long range surface plasmons and magnetic nanoparticle assays." In: *Analytical Chemistry* 84 (19), p. 8343.

Y. Xu C. Gu, B. Hou Y. Lai H. Chen and J. Li (2013). "Broadband asymmetric waveguiding of light without polarization limitations". In: *Nature Communications* 4. DOI: 10.1038/ncomms3561.. URL: https://www.nature.com/articles/ncomms3561.

Y. Zhang D.J.S. Birch, Y. Chen J. Yu (2010). "Gold nanorods for fluorescence lifetime imaging in biology". In: 15.2. URL: https://doi.org/10.1117/1.3366646.

Yamazoe S.; Naya, M.; Shiota M.; Tani T.; Morikawa T.; Kubo A.; Hishiki T.; Horiuchi T.; (2014). "Large-area surface-enhanced raman spectroscopy imaging of brain ischemia by gold nanoparticles grown on random nanoarrays of transparent boehmite". In: *ACS Nano vol: 8, issue 6, 2014, pp. 5622* 8 (6), p. 5622. URL: https://doi.org/10.1021/nn4065692.

Yang, G. et al. (2017). "Self-Assembly of Large Gold Nanoparticles for Surface-Enhanced Raman Spectroscopy". In: *Nano* 9.1 (15). URL: https://doi.org/10.1021/acsami.7b01121.

Yee, K. S. (1966). "Numerical solution of initial boundary value problems involving Maxwell's equations in isotropic media". In: *IEEE Transactions on Antennas and Propagation* 14.3, 302—307. DOI: 10.1109/TAP.1966.1138693. URL: https://doi.org/10.1109/TAP.1966.1138693.

Yen, Tzu-Hsiang et al. (2017). "Silicon photonics multi-channel Bragg reflectors based on narrowband cladding-modulated gratings". In: *2017 Conference on Lasers and Electro-Optics (CLEO)*, pp. 1–2.

Yen, Tzu-Hsiang et al. (2018). "Linewidth-adjustable bandpass filter based on silicon cladding-modulated waveguide moiré Bragg gratings". In: *Conference on Lasers and Electro-Optics*. Optica Publishing Group, JW2A.38. DOI: 10.1364/CLEO_AT.2018.JW2A.38. URL: https://opg.optica.org/abstract.cfm?URI=CLEO_AT-2018-JW2A.38.

Yun, Han et al. (2019). "Optical Add-drop Filters using Cladding-modulated Sub-wavelength Grating Contra-directional Couplers for Silicon-on-Insulator Platforms". In: *2019 IEEE 10th Annual Information Technology, Electronics and Mobile Communication Conference (IEMCON)*, pp. 0926–0931. DOI: 10.1109/IEMCON.2019.8936256.

Zhao, X. et al. (2020). "Sandwiched PbS/Au/PbS phototransistor for surface plasmon enhanced near-infrared photodetection". In: *J.Alloy. compd.* 815.152331. URL: https://doi.org/10.1016/j.jallcom.2019.152331.

Zheludev, Nikolay I. and Yuri S. Kivshar (2012). "From metamaterials to metadevices". In: *Nature Materials* 19.11, pp. 917–924. DOI: 10.1038/nmat3431. URL: https://doi.org/10.1038/nmat3431.

Zhou, Xuetong et al. (2015). "Ultrabroad terahertz bandpass filter by hyperbolic metamaterial waveguide". In: *Opt. Express* 23.9, pp. 11657–11664. DOI: 10.1364/OE.23.011657. URL: https://opg.optica.org/oe/abstract.cfm?URI=oe-23-9-11657.

Zhukovsky, Sergei V. et al. (2014). "Photonic-band-gap engineering for volume plasmon polaritons in multiscale multilayer hyperbolic metamaterials". In: *Phys. Rev. A* 90 (1), p. 013801. DOI: 10.1103/PhysRevA.90.013801. URL: https://link.aps.org/doi/10.1103/PhysRevA.90.013801.